Surface Energy Balance Modeling in Urban Environments

A numerical study on the influence of thermal radiation on the urban heat island effect using a one-way coupled RANS $k - \epsilon$ approach

Alje Visser

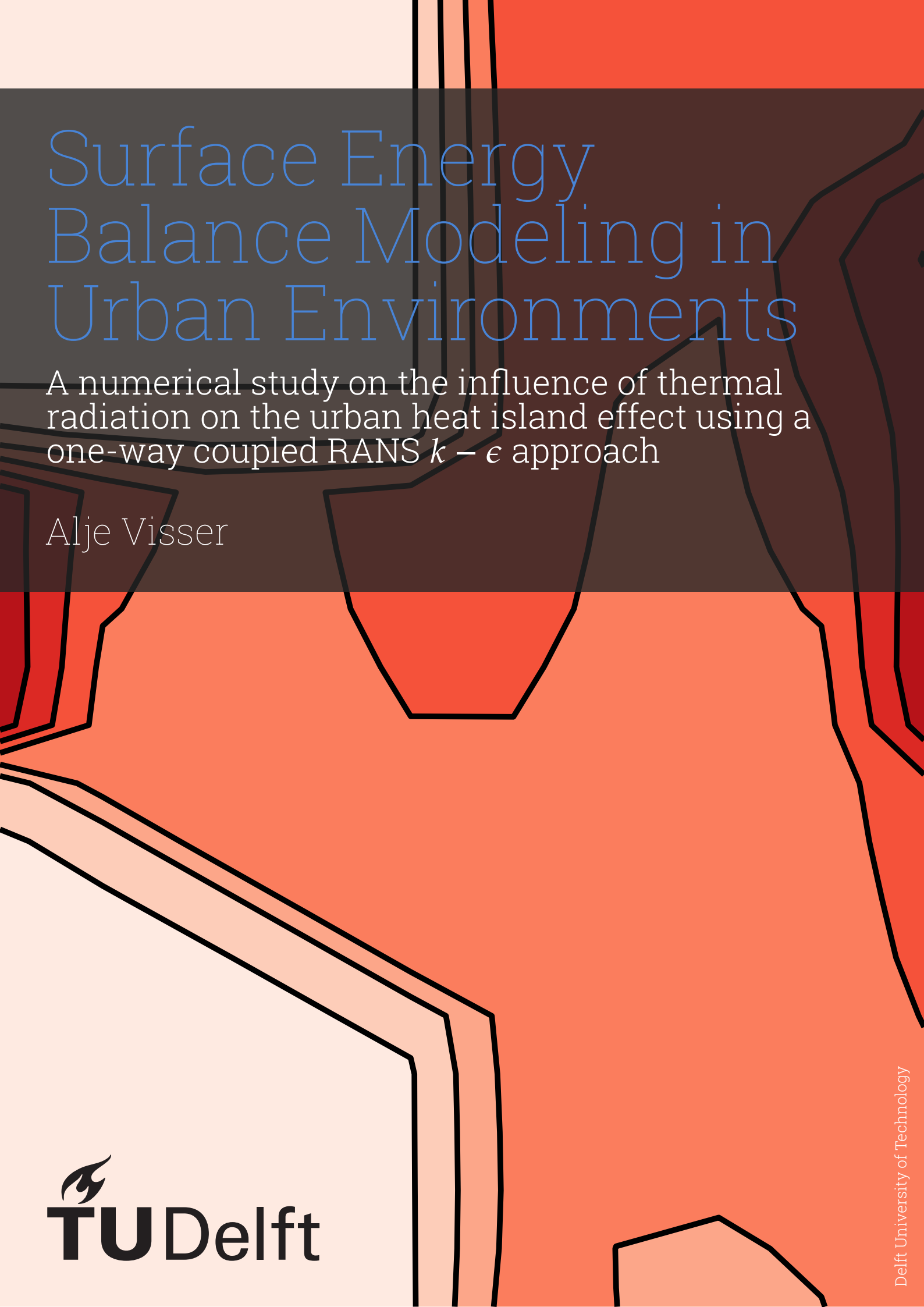

Delft University of Technology

Surface Energy Balance Modeling in Urban Environments

A numerical study on the influence of thermal radiation on the urban heat island effect using a one-way coupled RANS $k-\epsilon$ approach

by

Alje Visser

in order to fulfill the requirements for the degree of

Master of Science
in Applied Physics

at the Delft University of Technology,
to be defended publicly on August 28, 2023 at 14:00.

Student number:	4586972	
Project duration:	Dec. 12, 2022 - Aug. 28, 2023	
Thesis committee:	Prof. dr. S. Kenjereš,	TU Delft, supervisor
	Dr. B. Bera,	TU Delft
	Dr. S.R. de Roode,	TU Delft

TU Delft

Abstract

A phenomenon that compromises the health of city inhabitants is the urban heat island (UHI) effect. This effect is mainly driven by thermal radiation and designates the typically higher air temperature in cities compared to the surrounding rural areas. Over 55% of the world's population lives in cities, and with this percentage set to rise to more than 65% by 2050, it is vital to model the urban climate to be able to mitigate the UHI-effect. In this study, the surface energy balance (SEB) is modeled in urban environments using a one-way coupled RANS $k-\epsilon$ approach in order to gain fundamental insights into the influence of thermal radiation on the UHI-effect. The SEB model is built mechanism-by-mechanism, adding in different physical mechanisms one at a time and validating the model at each step with literature- or theoretical values.

The SEB model showed a good agreement with experimentally found values for the effect of surface irregularity of an urban structure on the absorption and reflection of incident solar radiation. A good agreement was also found with theoretical values for the longwave radiation and conductive heat flux part of the SEB model. Subsequently, a study was done on a 2D street canyon to compare the model with literature results. This study showed a good agreement for the radiative fluxes, but a lesser agreement for the conductive- and sensible heat fluxes. A more complex scenario of an intersection between buildings was studied. It was shown that the longwave trapping effect is highly correlated with building height. Finally, the effect of wall heating on flow characteristics in a 2D street canyon was examined. For homogeneously heated walls, the SEB model showed a relatively good agreement with literature results. A study was also done with non-homogeneously heated walls. This study showed less realistic results and should be further investigated in further research.

Contents

Nomenclature

Abbreviations

Abbreviation	Definition
CDS	Central differencing scheme
CFD	Computational fluid dynamics
DNS	Direct numerical simulation
FVM	Finite volume method
GDDH	Generalized gradient diffusion hypothesis
LES	Large eddy simulation
NMAE	Normalized mean absolute error
RANS	Reynolds-averaged Navier-Stokes
SEB	Surface energy balance
SGDH	Simple gradient diffusion hypothesis
SIMPLE	Semi-implicit method for pressure-linked equations
SIP	Strongly implicit procedure
UDS	Upwind differencing scheme
UHI	Urban heat island
UTCI	Universal Thermal Climate Index

Symbols

Symbol	Definition	Units
A_i	Surface of facet i	m^2
c_p	Specific heat	$Jkg^{-1}K^{-1}$
C_i	Facet contour	m
$C_{\epsilon 1}$	k-ϵ model coefficient	-
$C_{\epsilon 2}$	k-ϵ model coefficient	-
$C_{\epsilon 3}$	k-ϵ model coefficient	-
C_μ	k-ϵ model coefficient	-
d	Wall thickness	m
D	Diffusive shortwave radiation	Wm^{-2}
D_{sky}	Total diffusive sky radiation	Wm^{-2}
e	Roughness length	m
E	Latent heat flux	Wm^{-2}
E_r	Roughness constant	-
f_e	Sun-lit factor	-
f_{sc}	Scaling factor	m^{-1}
g_i	Acceleration of gravity	ms^{-2}
G	Conduction heat flux	Wm^{-2}
H	Sensible heat flux	Wm^{-2}
k	Turbulent kinetic energy	m^2s^{-2}
K	Shortwave radiation	Wm^{-2}
l_e	Integral turbulent length scale	m
L	Longwave radiation	Wm^{-2}
$L^{\downarrow}_{\text{env},i}$	Incoming longwave radiation from other facets	Wm^{-2}

Symbol	Definition	Units
$L^{\downarrow}_{\text{sky}}$	Total incoming longwave radiation from the sky	Wm^{-2}
$L^{\downarrow}_{\text{R}}$	Incoming reflected longwave radiation	Wm^{-2}
L_s	Length of a shared vertex	m
P	Pressure	$kgm^{-1}s^{-2}$
P_k	Production of turbulence kinetic energy	m^2s^{-3}
Pr_t	Turbulent Prandtl number	-
O	Other heat fluxes	Wm^{-2}
Q	Stored heat	Wm^{-2}
R	Reflected shortwave radiation flux	Wm^{-2}
S	Shortwave radiation flux	Wm^{-2}
S_d	Distance between two facets	m
S_{ij}	Symmetric strain rate tensor	s^{-1}
S_k	Turbulence kinetic energy sink/source term	m^2s^{-3}
t	Time	s
T_s	Surface temperature	K
T_∞	Interior temperature	K
u'_i	Fluctuating velocity	ms^{-1}
$\hat{U}_i$	Instantaneous velocity	ms^{-1}
U_i	Mean velocity	ms^{-1}
U_τ	Friction velocity	ms^{-1}
x_i	Position	m
Q	Stored heat	Wm^{-2}
α	Shortwave albedo factor	-
β	Thermal expansion coefficient	K^{-1}
δ_{ij}	Kronecker delta function	-
ϵ	Turbulent dissipation rate	m^2s^{-3}
ϵ_c	Reflection convergence criterion	-
ε	Longwave emissivity	-
η	Angle to normal of an area	rad
η_e	Kolmogorov length scale	m
λ	Thermal conductivity	$Wm^{-1}K^{-1}$
μ	Dynamic viscosity	$kgm^{-1}s^{-1}$
ν	Kinematic viscosity	m^2s^{-1}
ν_t	Turbulent viscosity	m^2s^{-1}
ϕ_i	Facet i's azimuthal angle	rad
ϕ_s	Sun's azimuthal angle	rad
ψ_{ij}	View factor of facet i on facet j	-
$\psi_{i,\text{sky}}$	Sky view factor	-
ρ	Density	kgm^{-3}
ρ_c	Correlation coefficient	-
σ	Stefan-Boltzmann constant	$Wm^{-2}K^{-4}$
σ_ϵ	Eddy diffusivity turbulent dissipation rate	-
σ_k	Eddy diffusivity turbulent kinetic energy	-
θ_i	Facet i's zenith angle	rad
θ_s	Sun's zenith angle	rad
τ	Turbulence timescale	s
τ_w	Wall shear stress	Pa
ζ	Longwave absorptivity	-

1

Introduction

1.1. Motivation

Inhabitants of cities are exposed to a variety of health risks due air-, water- and soil pollution, overcrowding, noise and poor housing (Vardoulakis et al., 2016). In addition to those risks, there is a mechanism that compromises the health of city inhabitants more indirectly, namely the urban heat island (UHI) effect. The UHI-effect designates the typically higher air temperature in cities compared to the surrounding rural areas, see figure 1.1. This comparatively high air temperature is mainly caused by a lack of water surfaces, limited vegetation and a large amount of heat absorption by buildings. Tan et al. (2010) showed that the UHI-effect intensifies heat waves, which, in turn, has a measurable increase in hospitalizations and mortality rate (Pyrgou and Santamouris, 2018). Over 55% of the world's population lives in cities, and with this percentage set to rise to 68% by 2050 (WHO, 2022), it is vital to model the urban climate to be able to mitigate these health risks.

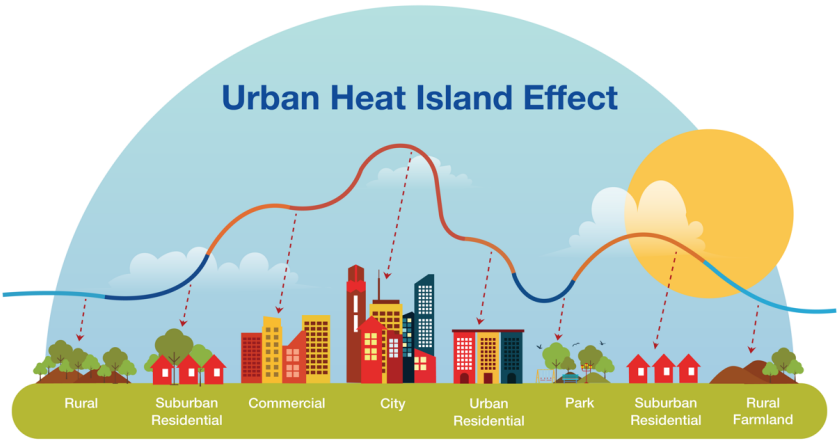

Figure 1.1: A schematic image of the urban heat island effect. The curved line indicates high- (red) and low (blue) temperatures. It can be seen that in urban environments the temperature is higher compared to rural areas (GOSmartBricks, 2022).

The key driver behind the UHI-effect is thermal radiation, which can be divided into two sorts: shortwave- and longwave radiation. Shortwave radiation mainly comes from the sun and is absorbed and reflected by buildings, pavements and other surfaces. Surfaces in cities, compared to that of rural areas, generally have a low level of reflectivity (Wang et al., 2007). Albedo is the measure of surface reflectivity, it designates the fraction of the amount of reflected radiation and the total incoming radiation on a surface. A lower albedo in cities therefore means that less radiation is reflected and more is absorbed compared to rural areas. The surfaces subsequently heat up and emit longwave radiation, which is then absorbed and reflected by other surfaces. This phenomenon is also referred to as longwave trapping. Besides

radiation, other physical mechanisms are at play in the dispersion of heat in cities. These include the conductive heat flux, which resembles heat transfer through building walls, streets and soil, the sensible heat flux, which designates heat transfer due to convection, and the latent heat flux, which concerns heat transfer due to the evaporation of water.

It is important to model the complex interaction of thermal radiation and other heat fluxes between surfaces to understand the UHI-effect, and to subsequently be able to (re-)design future urban environments. Field experiments can also be done to gain a better understanding of the UHI-effect, however, they are tedious to perform and entail high costs. Therefore, it is more efficient to use simulation methods, as they are generally lower in cost and more straightforward in execution.

In this study, the effect of thermal radiation and different heat fluxes on the surface temperature will be studied to get fundamental insights into the UHI-effect. This will be done by modeling the surface energy balance and, subsequently, comparing the current model with literature studies and values. Finally, the model will be used to study the effect of different parameters, such as the wind speed or building height, on the surface temperature in urban environments.

1.2. Literature background

Several observational studies have been done to study the UHI-effect. Núñez and Oke (1977) studied the energy exchanges occurring in an urban street canyon. They used field measurements conducted in a specially instrumented street canyon. Kolokotroni et al. (2006) used air temperature measurements carried out in London in 1999-2000 to quantify the London UHI-intensity. They studied the effect of increased air temperature in London on the effectiveness of stack night ventilation strategies for office buildings. Although the use of field measurements to study the UHI-effect is praised for its simplicity, it also has its downsides, as they are generally expensive. On top of that, in order to filter out noise like pedestrians and cars, the field measurements must be particularly extensive, which makes them very time-consuming.

For those reasons are the conduction of small-scale model experiments, in some cases, more favorable. Aida (1982) carried out a small-scale model experiment to examine the effect of surface irregularity of an urban structure on the anomalous absorption of incident solar radiation. On top of that, Aida observed the albedo change as a function of the solar zenith angle throughout the year in different urban geometries. Kanda et al. (2005) performed an outdoor small-scale model experiment to evaluate their numerical model. They performed a similar model experiment as Aida, but covered a wider range of surface geometries and seasons. Small-scale model experiments can provide detailed information about certain model parameters that the researchers are interested in. For example, Aida's experiment isolated the effect of surface properties on the effective albedo of certain urban geometries. The main drawback of using small-scale model experiments is that it's sometimes difficult to translate the experiment to a real world problem. Besides that, similar to field experiments, this is a time-consuming business.

Numerical studies on the UHI-effect have become increasingly popular with the rise of computational power. One of the simpler and computationally cheaper studies in this field is the energy balance budget for a building canyon, as suggested by Oke (1982). Oke uses a conservation of energy approach for a specific control volume to model the UHI-effect. In this model, the velocity field and turbulence are parameterized such that it is incorporated as heat fluxes in the energy balance. The energy balance budget method is computationally cheap and relatively simple. The decoupling of the velocity field and temperature field, however, makes the model weak in modeling the sensible/latent heat fluxes.

Approaches that do couple the temperature- and velocity fields are methods based on computational fluid dynamics (CFD). The CFD-based approaches that study the urban climate can be differentiated into meso-scale models and micro-scale models. An example of a meso-scale model is HARMONIE, a weather model of KNMI (2012). Meso-scale models, such as HARMONIE, typically have a range from 1 to several hundreds of kilometers and maintain a resolution of roughly 2-3 km. These meso-scale approaches model the urban boundary layer by assigning surface roughness numbers based on the urban geometry. Therefore, detailed information about what happens inside the urban boundary layer is not available.

Contrary to meso-scale models, micro-scale models give more insight into what happens inside the urban boundary layer. Micro-scale models solve the temperature equation and transport equations directly. Besides that, urban geometries, such as buildings and trees, can be modeled in more detail. In simulation methods based on Reynolds Average Navier-Stokes (RANS), the full range of turbulence scales is modeled. RANS models are inherently steady-state and come with low computational costs. Examples of simulation methods based on RANS that are capable of modeling the urban climate are MIMO (Ehrhard et al., 2000) and MITRAS (Schlünzen et al., 2003). Although both MIMO and MITRAS solve the velocity- and temperature field, the models do not solve the surface energy balance explicitly. Both models are focused on the dispersion of air pollutants and solving the velocity fields around urban geometries.

Simulation methods that resolve a large amount of the turbulence scales are methods based on large eddy simulation (LES). uDALES (Grylls et al., 2021) is one of those methods. uDALES is a very high-resolution (1-2 m), building-resolving, large eddy simulation code for the urban micro-climate. uDALES solves the surface energy balance per urban facet and models the multi-reflective behavior of radiation. The precision of LES-based methods comes at a cost, since the computational expenses of a LES code are often high compared to other methods.

1.3. Objective and scope of the study

The goal of this study is to model the surface energy balance (SEB) at micro-scale to obtain fundamental insights into the UHI-effect. This will be done by building a SEB model mechanism-by-mechanism, adding in different physical mechanisms one at a time. After every step, the model is validated quantitatively and qualitatively. After validation, the model will be used to simulate the diurnal pattern of the surface temperature in different geometries and under different conditions.

In chapter 2, the theory behind this study will be explained. In chapter 3, the numerical methods will be explained, which includes all discretization methods. After that, in chapter 4, a brief overview will be given of the numerical implementation. In chapter 5, the results and discussions will be presented. Lastly, in chapter 6, the final conclusions and recommendations will be given.

2

Theory

In this chapter, the physical and mathematical background will be given that is needed for the understanding of all physical mechanisms at play in this study. First, the governing equations will be discussed. Secondly, the surface energy balance modeling will be discussed. And lastly, turbulence modeling will be discussed.

2.1. Governing equations

The governing equations in this study consist of the conservation of mass equation, the conservation of momentum equation, the conservation of energy equation, and the surface energy balance. The equations in this section are given in the Cartesian coordinate system designated by the triplet $x_i = (x, y, z)$. Besides that, Einstein notation is used to describe the equations in a succinct fashion.

2.1.1. Conservation of mass

The conservation of mass is given by the continuity equation, which states that the mass flow rate of a fluid entering a specified volume must be equal to the mass flow rate exiting the same specified volume plus the accumulation of mass within the specified volume. The continuity equation is given as follows:

$$\frac{\partial \hat{\rho}}{\partial t} + \frac{\partial}{\partial x_i}\left(\hat{\rho}\hat{U}_i\right) = 0, \tag{2.1}$$

where $\hat{\rho}$ is the density of the fluid, t represents time and $\hat{U}_i$ stands for the instantaneous velocity. In the case of an incompressible fluid, i.e., where the density is constant over time and space, the continuity equation can be written as:

$$\frac{\partial \hat{U}_i}{\partial x_i} = 0. \tag{2.2}$$

2.1.2. Conservation of momentum

The conservation of momentum is given by the Navier-Stokes equation, which states that the total momentum of a system remains constant unless acted upon by an external force. This equation can be mathematically expressed as:

$$\underbrace{\hat{\rho}\frac{\partial \hat{U}_i}{\partial t}}_{\text{time rate of change}} + \underbrace{\hat{\rho}\hat{U}_j\frac{\partial \hat{U}_i}{\partial x_j}}_{\text{convection}} = \underbrace{-\frac{\partial \hat{P}}{\partial x_i}}_{\text{pressure gradient}} + \underbrace{\frac{\partial}{\partial x_j}\left[\mu\left(\frac{\partial \hat{U}_i}{\partial x_j} + \frac{\partial \hat{U}_j}{\partial x_i}\right)\right]}_{\text{diffusion}} \underbrace{- \hat{\rho} g_i \beta\left(\hat{T} - T_{ref}\right)}_{\text{buoyancy term}}, \tag{2.3}$$

where P represents the pressure and μ is the dynamic viscosity. Besides that, g_i represents the acceleration of gravity, β is the thermal expansion coefficient of air and T_{ref} is the reference temperature.

2.1.3. Conservation of energy

The conservation of energy is one of the most fundamental equations in nature. Since energy must be conserved, a balance over a control volume can be derived. This is given by the following equation:

$$\hat{\rho} c_p \left(\frac{\partial \hat{T}}{\partial t} + \hat{U}_j \frac{\partial \hat{T}}{\partial x_j} \right) = \frac{\partial}{\partial x_j} \left(\lambda \frac{\partial \hat{T}}{\partial x_j} \right) - \hat{\rho} \frac{\partial \overline{\theta u_j'}}{\partial x_j}, \tag{2.4}$$

where $\hat{T}$ represents the instantaneous temperature, λ the thermal conductivity, c_p the heat capacity and $\overline{\theta u_j'}$ represents the turbulent heat flux.

2.1.4. Surface energy balance

The surface energy balance (SEB) is an equation consisting of a balance between several forms of incoming- and outgoing energy fluxes striking or exiting a surface. The SEB describes the flow of energy from and to a surface and, therefore, also determines the temperature of the surface in question. Following the notation of Grylls et al. (2021), the SEB can be expressed as follows:

$$\frac{dQ}{dt} = (L^{\downarrow} - L^{\uparrow}) + (K^{\downarrow} - K^{\uparrow}) - (H + E + G) + O, \tag{2.5}$$

where Q stands for the stored heat, $(K^{\downarrow}, K^{\uparrow})$ for the incoming and outgoing shortwave radiation, respectively, $(L^{\downarrow}, L^{\uparrow})$ for the incoming and outgoing longwave radiation, respectively. Besides that, H represents the turbulent sensible heat flux, E for the turbulent latent heat flux, G for the ground heat flux, and O for other fluxes such as, for example, the anthropogenic heat flux. All terms have the units of Watts per square meter (W m^{-2}). The latent heat flux, E, and the other heat flux, O, are outside the scope of this study. Besides that, this study is modeling in steady-state. Due to the omission of these fluxes and the modeling in steady-state, this leads to the following governing equation for the SEB in this study:

$$(L^{\downarrow} - L^{\uparrow}) + (K^{\downarrow} - K^{\uparrow}) - (H + G) = 0. \tag{2.6}$$

2.2. Surface energy balance modeling

The surface energy balance (SEB) consists of several forms of incoming- and outgoing energy fluxes, as was explained in section 2.1.4. In this section, the modeling of the SEB will be discussed.

A key component of the SEB is thermal radiation. In radiative heat transfer studies, surface areas are commonly referred to as facets, each with different (thermal) properties. It must be noted that in modeling the SEB, a set of assumptions has been made. These assumptions include that (1) no wavelength dependency is acknowledged to the radiation except the distinction between longwave- and shortwave radiation, (2) the radiosity across a facet is uniform, (3) that each facet is isothermal, (4) facets are 'grey' in the longwave regime ($\alpha = \varepsilon$) and (5) that reflections and emitted radiation are diffusive (no specular reflections).

In the upcoming sections, the modeling of the different energy fluxes included in the SEB will be discussed. First, the view factor modeling will be discussed. This is a geometric relation between different facets used to model the radiative exchanges between facets.

2.2.1. View factor

In radiative heat transfer, the view factor ψ_{ij} is defined as the fraction of radiation leaving facet i with surface area A_i and striking facet j with surface area A_j and lies, therefore, per definition between 0 and 1. A frequently used formula for the view factor of a facet with area A_i on a facet with area A_j is stated as follows:

$$\psi_{ij} = \frac{1}{A_i} \int_{A_i} \int_{A_j} \frac{\cos \eta_i \cos \eta_j}{\pi S_d^2} dA_j dA_i. \tag{2.7}$$

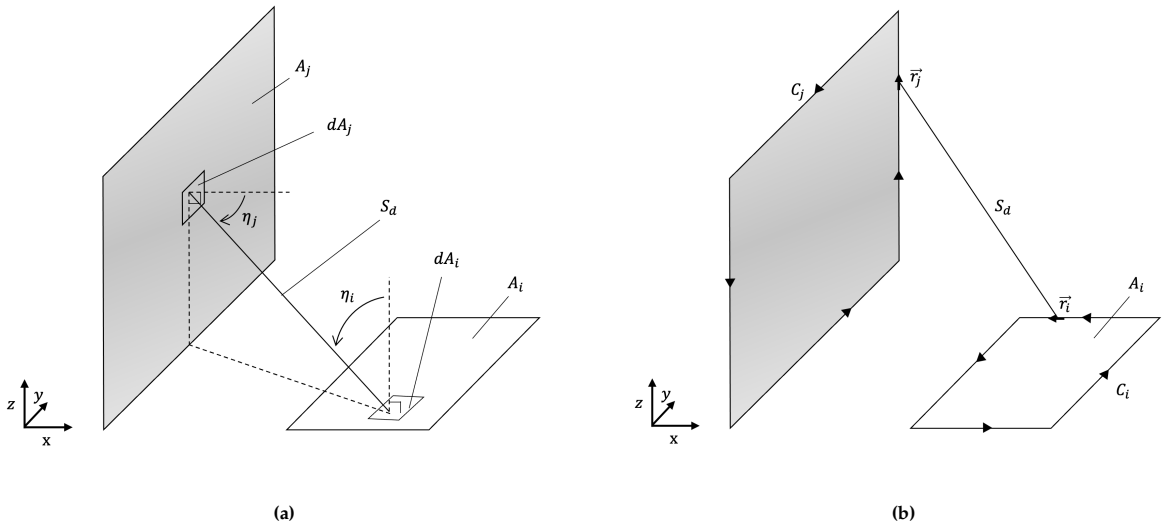

Figure 2.1: Schematics showing the relevant geometric quantities for the view factor in (a) area integral form and (b) contour integral form.

In equation 2.7, η is the angle to the normal of the two respective facets and S_d is the distance between the two facets. The geometric quantities from equation 2.7 are schematically presented in figure 2.1a. Sparrow and Cess (1963) showed that the view factor between two surface areas can also be expressed in a double contour integral form. This form is commonly referred to as the contour integration formula and is described in the following equation:

$$\psi_{ij} = \frac{1}{2\pi A_i} \oint_{C_i} \oint_{C_j} \ln S_d \, d\vec{r}_i \cdot d\vec{r}_j. \tag{2.8}$$

The geometric quantities of this equation are schematically shown in figure 2.1b. A significant amount of computational time can be saved by using equation 2.8 in view factor calculations instead of equation 2.7, since the integration is over two lines instead of over two areas. Therefore, the contour integration formula is used to calculate the view factor in this study.

It must be noted that evaluating equation 2.8 cannot be done when two areas share a common edge, since $\ln S_d$ diverges. Ambirajan and Venkateshan (1993) have provided an analytical contribution to the overall view factor in the case of a shared edge. This analytical contribution is defined as follows:

$$\Delta\psi_{ij} = \frac{L_s^2}{2\pi}\left(\frac{3}{2} - \ln L_s\right), \tag{2.9}$$

where L_s stands for the length of the shared edge. Besides the case of two shared edges, Grylls et al. (2021) distinguished three important exceptions to be taken into account when evaluating the view factor of a geometry using equation 2.8.

(i) The first exception is that of two planes that cannot see each other given their orientation and location. For example, a west-facing facet cannot see another west-facing facet, and a west-facing facet cannot see a facet that is located east of it.

(ii) The second exception occurs when two facets intersect. This problem can be dealt with adequately by cropping the intersected facet such that no intersection occurs. In this study, however, intersecting facets are not considered for the sake of simplicity.

(iii) The third exception occurs when the view of one facet on another facet is blocked, for example, by other facets or objects such as trees. This exception is the most tenacious to deal with and no straightforward solution exists. Therefore, Grylls et al. (2021) provide a more pragmatic approach to this problem by determining a percentage that designates how much a facet sees the other. This is, subsequently, multiplied by the unobstructed view factor.

At last, after all the view factors have been calculated, the view factor of facet i on the sky, $\psi_{i,\text{sky}}$, can be determined. This value can easily be calculated by considering that radiation leaving a surface is conserved and that the sum of the view factor of surface area A_i on all other surfaces is unity: $\sum_{j=1}^{n} \psi_{ij} = 1$. This means that $\psi_{i,\text{sky}}$ can be determined as follows:

$$\psi_{i,\text{sky}} = 1 - \sum_{j=1}^{n} \psi_{ij}, \tag{2.10}$$

with n the total number of facets in the computational domain.

2.2.2. Shortwave radiation

Shortwave radiation is ultimately the driving force behind the surface energy balance. This class of radiation represents the incoming ultraviolet and visible energy fluxes from the sun. Under the assumption that there is no transmission of radiation through the surface, the net shortwave radiation K (W m^{-2}) for a facet i is given as:

$$K_i = K_i^{\downarrow} - K_i^{\uparrow}, \tag{2.11}$$

where $K^{\downarrow}$ designates the incoming shortwave radiation and $K^{\uparrow}$ the outgoing shortwave radiation. Since there is no transmission, the outgoing radiation can be expressed in terms of the incoming radiation with the help of the albedo factor α. This results in the following:

$$K_i = (1 - \alpha_i) K_i^{\downarrow}, \tag{2.12}$$

where α_i is the albedo factor of facet i. According to Oke et al. (2017), the incoming shortwave radiation can be divided into three sorts: the diffusive shortwave radiation from the sky, D, the direct shortwave radiation coming from the sun, S, and the reflected shortwave radiation, R, coming from other surfaces. This gives the following equation:

$$K_i^{\downarrow} = D_i + S_i + R_i. \tag{2.13}$$

The diffusive radiation striking each facet is determined by multiplying the sky view factor, $\psi_{i,\text{sky}}$, with D_{sky}, the total diffusive sky radiation:

$$D_i = \psi_{i,\text{sky}} D_{\text{sky}}. \tag{2.14}$$

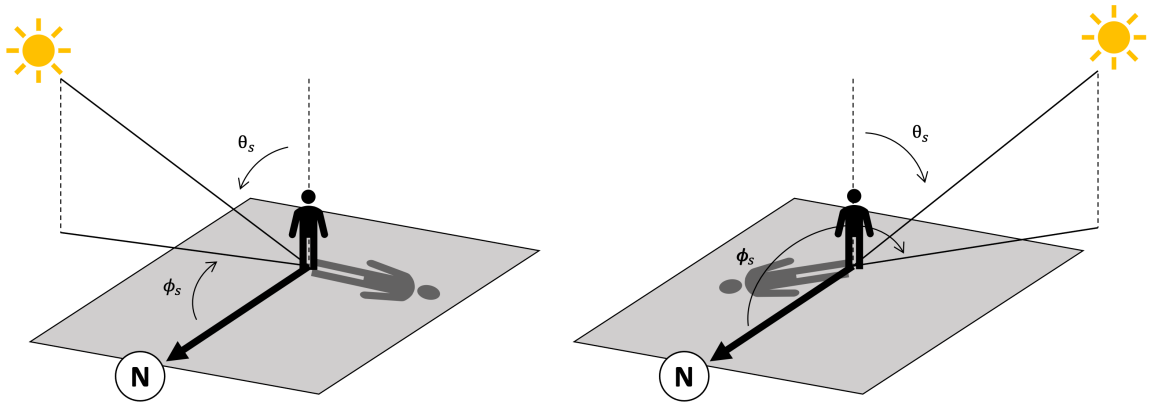

Figure 2.2: A schematic representation of the two solar angles: the solar zenith angle, θ_s, and the solar azimuthal angle, ϕ_s. Here, N designates true north.

In order to compute the direct shortwave radiation, S, different parameters need to be taken into account. These parameters include the solar azimuthal angle, ϕ_s, and the solar zenith angle, θ_s, which give the position of the sun with respect to the earth surface. These angles are schematically depicted in figure 2.2. Besides that, the facet's azimuthal angle, ϕ_i, the facet's zenith angle, θ_i, and the sun-lit factor, $f_{e,i}$, must be taken into account. The solar angles are taken from the site of National Oceanic and

Atmospheric Administration (NOAA, 2023). The direct shortwave radiation on a facet i is given as (Wu, 1995):

$$S_i = I \cos(\theta_s - \theta_i) \cos(|\phi_s - \phi_i|) f_{e,i}, \tag{2.15}$$

where I represents the solar irradiance on a given time and geographic location on Earth. Both I and D_{sky} are model inputs based on ASHRAE (2001). The sun-lit factor, $f_{e,i}$, is determined with a similar approach to the blocking percentage calculation in the view factor. For each facet, it is determined whether the path between the facet and the sun is blocked by another facet. This is determined for the four vertices and the central node of each facet. Each vertex contributes 12.5 % to $f_{e,i}$ and the central node contributes 50 % to $f_{e,i}$ (Grylls et al., 2021). This way, if none of the paths are blocked, the sun-lit factor is equal to 1.

Reflected radiation from the environment must be taken into consideration when determining the in- and outgoing shortwave radiation. These reflections are considered Lambertian and are modeled through an iterative approach, with each iteration resembling a reflection. This iterative approach is schematically given in figure 2.3 and can be summarized as follows. The first step is making an initial guess of the outgoing radiation of each facet, $K^{\uparrow}_{i,0}$. Subsequently, in step two, the reflected radiation striking each facet after one reflection, $R_{i,0}$, is computed. This is added to the total incoming radiation on each facet in step three. In step four, the n-th reflection of each facet is determined and in step five the reflected radiation striking each facet is determined and added to the total incoming radiation of each facet. This results in a looping procedure that stops when the convergence criterion ϵ_c is met, which is set at 0.1 %.

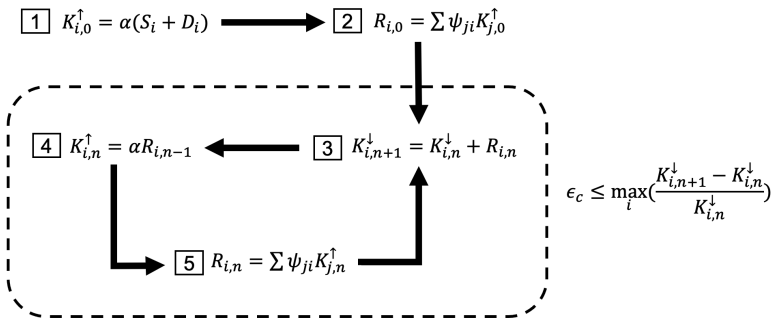

Figure 2.3: A schematic representation of the iterative procedure to compute the total reflected shortwave radiation. Here, K represents the total shortwave radiation, R represents the reflected radiation, ψ signifies the view factor and ϵ_c is the convergence criterion.

2.2.3. Longwave radiation

Longwave radiation represents the infrared part of thermal radiation. The net longwave radiation striking facet i is expressed as follows:

$$L_i = \zeta_i \left(\psi_{\text{sky},i} L^{\downarrow}_{\text{sky}} + L^{\downarrow}_{\text{env},i} + L^{\downarrow}_{\text{R},i} \right) - L^{\uparrow}_i, \tag{2.16}$$

where ζ_i is the longwave absorptivity, $L^{\downarrow}_{\text{sky}}$ represents the incoming longwave radiation coming from the sky, $L^{\downarrow}_{\text{env},i}$ is the incoming longwave radiation from other facets, $L^{\downarrow}_{\text{R},i}$ represents the incoming reflected longwave radiation and $L^{\uparrow}_i$ presents the outgoing longwave radiation. Following Grylls et al. (2021), $L^{\downarrow}_{\text{R},i}$ is neglected and set to zero in this study, since, for many building materials, the absorptivity is generally close to unity. The outgoing longwave radiation, $L^{\uparrow}_i$, depends on the surface temperature $T_{s,i}$ according to the Stefan-Boltzmann law:

$$L^{\uparrow}_i = \sigma \varepsilon_i T^4_{s,i}, \tag{2.17}$$

with the Stefan-Boltzmann constant σ and the facet's longwave emmisivity ε_i. The incoming longwave radiation from other facets can also be expressed according to the Stefan-Boltzmann law:

$$L^{\downarrow}_{\text{env},i} = \sum_{j=1}^{p} \psi_{ji} \varepsilon_j T^4_{s,j}, \tag{2.18}$$

where p represents the total number of facets. $L^{\downarrow}_{\text{sky}}$ is given as a model input.

2.2.4. Conductive heat flux

The conductive heat flux at each facet, G_i, is given by:

$$G_i = \lambda_i \frac{\partial T_{s,i}}{\partial \xi} \Big(\xi = 0 \Big), \tag{2.19}$$

where λ_i is the thermal conductivity of facet i, T_i the temperature of the facet and ξ the position vector point into the surface. In the present study, it is assumed that each facet consists of one single layer of building material with thickness d and internal temperature, $T_{\infty,i}$, which is the temperature at depth d and is given as model input. This results in the following discretized equation:

$$G_i = \lambda \frac{T_{s,i} - T_{\infty,i}}{d_i}. \tag{2.20}$$

2.2.5. Sensible heat flux

The sensible heat flux represents the heat exchange between the surface and the surrounding medium and is modeled with the use of the Simple Gradient Diffusion Hypothesis (SGDH):

$$\overline{\theta u_i'} = -\frac{\nu_t}{Pr_t} \frac{\partial T}{\partial x_i}, \tag{2.21}$$

where $\overline{\theta u_i'}$ is the turbulent heat flux, ν_t is the turbulent viscosity and Pr_t is the turbulent Prandtl number. The turbulent Prandtl number is set to 0.86 in accordance with Schrijvers (2020) to acquire stable solutions. The turbulent viscosity, ν_t, is calculated with the use of turbulence modeling. This will be explained in the next section. The sensible heat flux can be expressed in terms of the turbulent heat flux:

$$H_i = -\rho c_p \overline{\theta u_i'}, \tag{2.22}$$

where ρ is the density of the surrounding medium and c_p is the specific heat of the surrounding medium. The air temperature is kept constant in the current model's one-way coupling approach. Therefore, when the previous two equations are synthesized and the temperature gradient is linearized, the following is acquired:

$$H_i = \rho c_p \frac{\nu_t}{Pr_t} \frac{T_{s,i} - T_{\text{air}}}{\Delta x}. \tag{2.23}$$

In the equation above, T_{air} represents the ambient air temperature and Δx represents the distance between the facet and point in the surrounding medium.

2.3. Turbulence modeling

Turbulence is a chaotic phenomenon that occurs in fluid flows. Turbulence modeling is the study of mathematically representing turbulence in CFD simulations. There are three main approaches to turbulence modeling: Reynolds-Averaged Navier-Stokes (RANS), Large Eddy Simulation (LES), and Direct Numerical Simulation (DNS).

DNS is a simulation method that completely solves the Navier-Stokes equations without using turbulence modeling. DNS is, therefore, computationally expensive as it requires resolving all of the turbulent scales in the flow. DNS is particularly useful in fundamental studies of turbulence as it provides detailed information on the flow field. The computational expenses, however, are generally too high and DNS is

therefore mostly used in academic studies.

LES is a computational method that solves large-scale turbulent structures while modeling small-scale structures. The small-scale turbulent structures are modeled using so-called sub-grid scale models. LES is less computationally expensive compared to DNS while still achieving high accuracy in simulating large-scale turbulent structures. Therefore, LES is particularly useful in situations where large-scale structures are of primary interest, such as in acoustics or weather simulations.

RANS is a computational method that models all turbulence by time-averaging the Navier-Stokes equations. RANS models are based on the assumption that instantaneous quantities, such as the velocity, can be decomposed into a mean- and a fluctuating component. The mean component is computed using the Reynolds-averaged equations, while the fluctuating component is modeled using turbulence models. RANS is the least computationally expensive out of all three approaches, but it is less accurate in capturing the details of the turbulent flow.

In this study, the RANS $k-\epsilon$ model will be used. This method will be employed such that the surface temperature can be coupled to a (turbulent) flow field. In the next subsections, the RANS $k-\epsilon$ model will be discussed in further detail.

2.3.1. Reynolds averaging

In the RANS approach, the conservation equations are statistically averaged before they are solved. An instantaneous property can be decomposed into a mean- and fluctuating component. The instantaneous velocity, $\hat{U}_i(x_i,t)$, can be decomposed as follows:

$$\hat{U}_i(x_i,t) = U_i(x_i) + u_i'(x_i,t), \tag{2.24}$$

where $U_i(x_i)$ is its mean component and $u_i'(x_i,t)$ its fluctuating component. The mean component is defined as:

$$U_i(x_i) = \lim_{T\to\infty} \int_0^T \hat{U}_i(x_i,t)dt. \tag{2.25}$$

It must be noted that the integration time must be sufficiently large compared to the turbulent time-scales. With the decomposition in mind, the left-hand side of the Navier-Stokes equation (equation 2.3), after Reynolds averaging, can be written as:

$$\rho\frac{\partial U_i}{\partial t} + \rho\frac{\partial \overline{\hat{U}_i\hat{U}_j}}{\partial x_j}. \tag{2.26}$$

The non-linear term in the equation above can be further expanded by applying Reynolds averaging. This is done as follows:

$$\overline{\hat{U}_i\hat{U}_j} = \overline{(U_i+u_i')(U_j+u_j')} = \overline{U_iU_j + U_iu_j' + u_i'U_j + u_i'u_j'} = U_iU_j + \overline{u_i'u_j'}, \tag{2.27}$$

where $\overline{u_i'u_j'}$ is also known as the Reynolds stress.

The other terms in equation 2.3 can be expanded and expressed in a similar manner as done above. This leads to the RANS equation:

$$\rho\frac{\partial U_i}{\partial t} + \rho U_j\frac{\partial U_i}{\partial x_j} = -\frac{\partial P}{\partial x_i} + \frac{\partial}{\partial x_j}\left[\mu\left(\frac{\partial U_i}{\partial x_j} + \frac{\partial U_j}{\partial x_i}\right) - \rho\overline{u_i'u_j'}\right] - \rho g_i\beta\Big(T - T_{ref}\Big). \tag{2.28}$$

The Reynolds stress, $\overline{u_i'u_j'}$, cannot be calculated directly and must therefore be modeled to close the RANS equation. This will be explained in the next subsection.

The Reynolds-averaged transport equation for energy is given as follows:

$$\rho c_p \left(\frac{\partial T}{\partial t} + U_j \frac{\partial T}{\partial x_j} \right) = \frac{\partial}{\partial x_j} \left[\lambda \frac{\partial T}{\partial x_j} - \rho c_p \overline{\theta u_j'} \right], \tag{2.29}$$

where $\overline{\theta u_j'}$ is modeled by the SGDH, as was discussed in the previous section.

2.3.2. The k-ϵ turbulence model

The k-ϵ turbulence model is a commonly used turbulence model based on the Boussinesq assumption. This states that the turbulent stress tensor can be expressed in terms of the strain rate tensor in the same fashion as Newtonian isotropic fluids, except that the viscosity is replaced by the turbulent eddy viscosity. The model consists of two additional transport equations for the turbulent kinetic energy, k, and the turbulent dissipation rate, ϵ. The model states that the turbulent viscosity, ν_t, relates to the shear components of the Reynolds stress in the following way:

$$\overline{u_i' u_j'} = -\nu_t \left(\frac{\partial U_i}{\partial x_j} + \frac{\partial U_j}{\partial x_i} \right) + \frac{2}{3} k \delta_{ij}, \tag{2.30}$$

where δ_{ij} stands for the Kronecker delta function. The turbulent kinetic energy, k, is defined as

$$k \equiv \frac{1}{2} \overline{u_i' u_j'} \tag{2.31}$$

and the turbulent viscosity, ν_t, is defined as

$$\nu_t = C_\mu k \tau = C_\mu \frac{k^2}{\epsilon}, \tag{2.32}$$

where τ represents the turbulent timescale and is equal to $\frac{k}{\epsilon}$ and C_μ is a model constant, given in table 2.1. The transport equation for k can then be found by subtracting equation 2.28 from equation 2.3, multiplying this by u_i', and, subsequently Reynolds averaging. This gives the following transport equation for k:

$$\underbrace{\frac{\partial k}{\partial t}}_{\text{time rate of change}} + \underbrace{U_j \frac{\partial k}{\partial x_j}}_{\text{convection}} = \underbrace{\frac{\partial}{\partial x_j} \left[\left(\nu + \frac{\nu_t}{\sigma_k} \right) \frac{\partial k}{\partial x_j} \right]}_{\text{diffusion}} + \underbrace{P_k}_{\text{production}} - \underbrace{\epsilon}_{\text{dissipation}} - \underbrace{g_j \beta \overline{\theta u_j'}}_{\text{sink/source}}. \tag{2.33}$$

In the equation above, σ_k is the eddy diffusivity, P_k represents the production of turbulent kinetic energy and S_k is an external sink/source term. The production of turbulent kinetic energy is then given as

$$P_k = -\overline{u_i' u_j'} \frac{\partial U_i}{\partial x_j} = \nu_t \left(\frac{\partial U_i}{\partial x_j} + \frac{\partial U_j}{\partial x_i} \right) \frac{\partial U_i}{\partial x_j} = 2 \nu_t S_{ij} S_{ij}, \tag{2.34}$$

where S_{ij} is the symmetric strain rate tensor and is defined as:

$$S_{ij} = \frac{1}{2} \left(\frac{\partial U_i}{\partial x_j} + \frac{\partial U_j}{\partial x_i} \right). \tag{2.35}$$

The dissipation of turbulent kinetic energy is defined as:

$$\epsilon \equiv \nu \overline{\left(\frac{\partial u_i'}{\partial x_j} \right)^2}. \tag{2.36}$$

This leads to the following transport equation for ϵ:

$$\underbrace{\frac{\partial \epsilon}{\partial t}}_{\text{time rate of change}} + \underbrace{U_j \frac{\partial \epsilon}{\partial x_j}}_{\text{convection}} = \underbrace{\frac{\partial}{\partial x_j} \left[\left(\nu + \frac{\nu_t}{\sigma_\epsilon} \right) \frac{\partial \epsilon}{\partial x_j} \right]}_{\text{diffusion}} + \underbrace{C_{\epsilon 1} \frac{\epsilon}{k} P_k}_{\text{production}} - \underbrace{C_{\epsilon 2} \frac{\epsilon^2}{k}}_{\text{dissipation}} + \underbrace{C_{\epsilon 3} g_i \beta \overline{\theta u_i'} \frac{\epsilon}{k}}_{\text{sink/source}}, \tag{2.37}$$

where $C_{\epsilon 1}$, $C_{\epsilon 2}$, $C_{\epsilon 3}$ and σ_ϵ are model coefficients and listed in table 2.1.

C_μ	$C_{\epsilon 1}$	$C_{\epsilon 2}$	$C_{\epsilon 3}$	σ_k	σ_ϵ
0.09	1.44	1.92	1.44	1.0	1.3

Table 2.1: Model coefficients for the standard k-ϵ model based on Launder and Sharma (1974).

2.3.3. Wall functions

In highly turbulent flow, velocity gradients near a surface may get very high, due to the thin viscous sublayer in that region caused by the no-slip boundary condition. This would require a very fine mesh in order to capture the turbulence in that region. In order to reduce the number of control volumes needed, wall functions are used. Wall functions are used to describe the flow behavior in the near-wall region, which is also known as the inner wall layer. This layer consists of three regions: a viscous sublayer, a buffer zone, and a logarithmic layer.

Log-law

The velocity profile in the near-wall region for the log-law is based on several assumptions. The first states that, in the viscous sublayer, the velocity does not depend on density, which is based on the fact that viscous forces dominate in this region. The second assumption states that, in the logarithmic region, inertial forces dominate and the velocity profile does not depend on the viscosity. After a dimensional analysis, this leads to the following equation:

$$U^+ = \begin{cases} y^+, & y^+ \leq 11.63 \\ \frac{1}{\kappa} \ln(E_r y^+) & y^+ > 11.63 \end{cases}, \tag{2.38}$$

where U^+ is the dimensionless velocity, given in equation 2.39, κ is the von Kármán constant ($\kappa = 0.41$), and E_r represents the roughness constant, which is an experimentally determined constant.

$$U^+ = \frac{U}{U_\tau} \tag{2.39}$$

In the equation above, U_τ stands for the friction velocity, which is expressed as follows:

$$U_\tau = \sqrt{\frac{\tau_w}{\rho}}, \tag{2.40}$$

where τ_w is the wall shear stress. The dimensionless distance from the wall, y^+, is defined as:

$$y^+ = \frac{y U_\tau}{\nu}. \tag{2.41}$$

Wall roughness

The roughness of a surface has a significant impact on the flow field. The log-law is derived with the assumption of smooth walls and must therefore be extended to include rougher surfaces. This is done by introducing the roughness length, e, which is expressed as follows (Pope, 2000):

$$e^* = \frac{U_\tau e}{\nu}, \tag{2.42}$$

where e^* represents the dimensionless roughness length. With this in mind and assuming a rough wall ($e^* \gg 1$), the log-law velocity profile is given as

$$U^+ = \frac{1}{\kappa} \ln\left(\frac{E_r}{e^*} y^+\right), \tag{2.43}$$

where E_r has a value of 30. For smoother walls, the value of $\frac{E_r}{e^*}$ can become unphysical. Therefore, to prevent this behavior, the wall function is limited by the following:

$$U^+ = \frac{1}{\kappa} \ln\left[\min\left(E, \frac{E_r}{\max(e^*, 0.1)}\right) y^+\right], \tag{2.44}$$

where E is the minimum roughness constant ($E = 8.432$) for a smooth wall.

3

Numerical methods

In order to model and solve the governing equations seen in the previous chapter, the equations must be discretized. In this chapter, the numerical methods used in this study will be given. These methods include the finite volume method, discretization schemes, and algorithms used to solve the system of equations.

3.1. Finite volume method

The finite volume method (FVM) is a numerical technique used to solve partial differential equations. It involves the subdividing of the total domain into a set of smaller control volumes and then solving the governing equations for each control volume. The general conservation equation for a physical quantity ϕ is given by

$$\underbrace{\frac{\partial(\rho\phi)}{\partial t}}_{\text{time rate of change}} + \underbrace{\vec{\nabla}\cdot(\rho\phi\vec{u})}_{\text{convection}} = \underbrace{\vec{\nabla}\cdot(\Gamma\vec{\nabla}\phi)}_{\text{diffusion}} + \underbrace{S_\phi}_{\text{source term}}, \tag{3.1}$$

where $\vec{\nabla}$ represents the gradient operator, $\vec{u}$ the velocity and Γ the transport coefficient of ϕ. The FVM can be applied to the conservation equation above by integrating over the volume of a grid cell, V. This results in the following equation:

$$\iiint_V \frac{\partial(\rho\phi)}{\partial t}dV + \iiint_V \vec{\nabla}\cdot(\rho\phi\vec{u})dV = \iiint_V \vec{\nabla}\cdot(\Gamma\vec{\nabla}\phi)dV, + \iiint_V S_\phi dV, \tag{3.2}$$

where V represents the volume of the grid cell. Gauss' theorem is employed to express the volume integral in terms of its fluxes on the boundaries of the control volume. Gauss' theorem is stated as follows:

$$\iiint_V \vec{\nabla}\cdot\vec{f}dV = \oiint_{A_V} \vec{f}\cdot d\vec{A}, \tag{3.3}$$

in which A_V is the area and $d\vec{A}$ the normal vector on this area. By applying Gauss' theorem on equation 3.2, the following is obtained:

$$\iiint_V \frac{\partial(\rho\phi)}{\partial t}dV + \oiint_{A_V} (\rho\phi\vec{u})\cdot d\vec{A} = \oiint_{A_V} (\Gamma\vec{\nabla}\phi)\cdot d\vec{A} + \iiint_V S_\phi dV. \tag{3.4}$$

In the equation above, two volume integrals have been replaced by surface integrals, which means that the values on the faces of the control volume are needed. The differencing schemes that are used for this are explained in the next section.
The volume integral of the sink/source term is approximated by taking the average value of this term in the control volume and multiplying this with the value of the control volume, V_P. This results in the following:

$$\iiint_V S_\phi dV \approx S_{\phi,P}V_P, \tag{3.5}$$

where $S_{\phi,P}$ is the average value of the source/sink term in the control volume.
The surface integrals are approximated by taking the sum of the normal fluxes on the respective part of the total area and multiplying this with the area itself. This is mathematically described as follows:

$$\oiint_{A_V} \vec{f} \cdot d\vec{A} \approx f_n A_n - f_s A_s + f_e A_e - f_w A_w + f_t A_t - f_b A_b, \tag{3.6}$$

where all subscripts resemble the cell faces in respective order: north, south, east, west, top, and bottom. This is schematically depicted in figure 3.1.

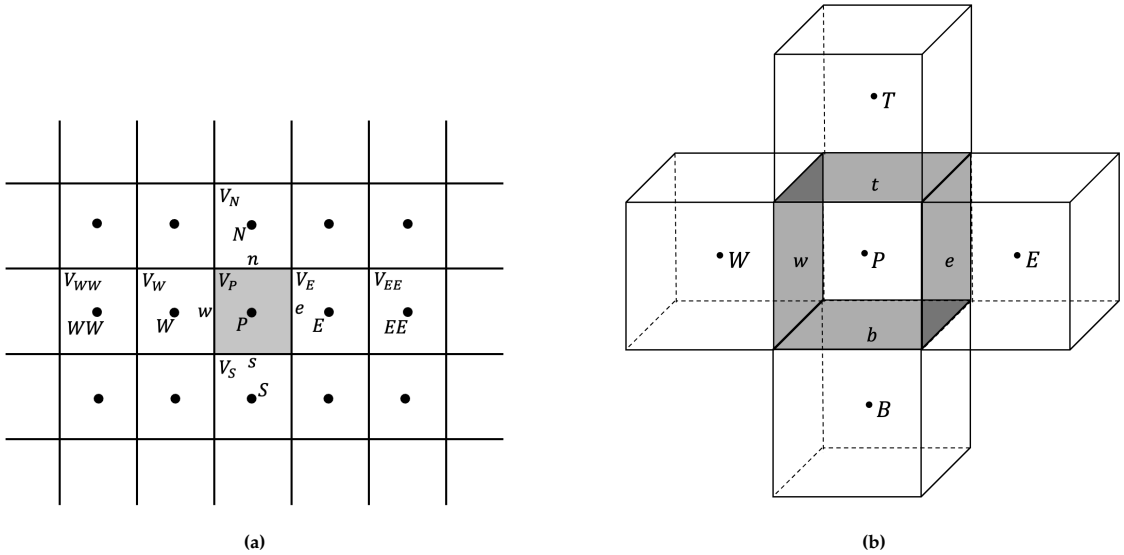

Figure 3.1: 2D (a) and 3D (b) schematic representation of the control volumes. The grey shaded area represents the control volume at interest, V_P. Note that cell face values are denoted with lowercase letters and cell center values with capital letters.

3.2. Discretization schemes

3.2.1. Upwind differencing scheme

The upwind differencing scheme (UDS) is a simple, unconditionally bounded, and first-order differencing scheme. It is called "upwind" because it projects upstream values onto the cell faces. This scheme is particularly useful for simulating flows where convection is dominant and where there is a dominant flow direction.

The UDS can be summarized as follows:

$$\Phi_e = \begin{cases} \Phi_P, & \text{if} \quad U \geq 0 \\ \Phi_E, & \text{if} \quad U < 0 \end{cases}, \tag{3.7}$$

where Φ is the conserved quantity and the subscripts denote cell center and cell face values according to figure 3.1. The scheme is also schematically depicted in figure 3.2.

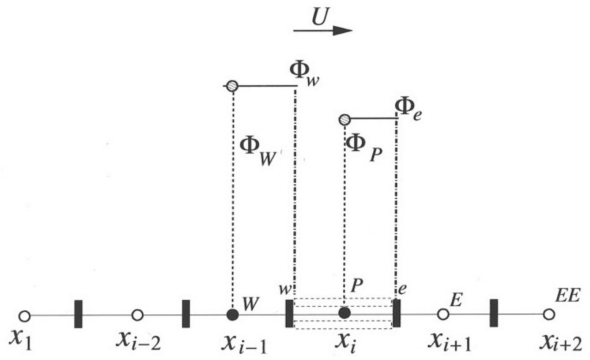

Figure 3.2: Schematic interpretation of the upwind differencing scheme (Hanjalić et al., 2007).

3.2.2. Central differencing scheme

The central differencing scheme (CDS) uses linear interpolations between the adjacent cells to estimate the cell face values. This scheme is mathematically formulated as follows:

$$\Phi_e = \lambda\Phi_E + (1-\lambda)\Phi_P, \tag{3.8}$$

where λ designates the interpolation factor which takes into account the non-uniformity of the grid cells. A schematic depiction of the other variables of CDS is given in figure 3.3. The CDS is easily applied and has a fast convergence rate. Its main drawback, however, is that it shows non-physical behavior for Péclet numbers greater than 2.

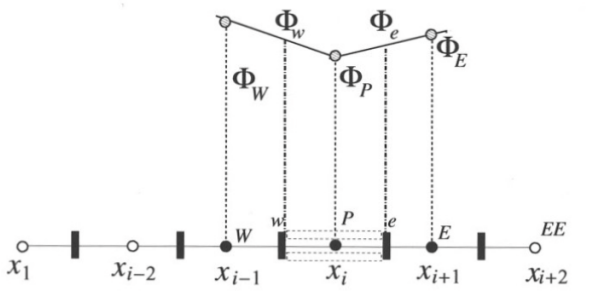

Figure 3.3: Schematic interpretation of the central differencing scheme (Hanjalić et al., 2007).

3.2.3. Gauss-Legendre quadrature

Gauss-Legendre quadrature is a method to approximate the integral of a function. This method is effective and accurate for straight-edged contours (Rao and Sastri, 1996). Gauss-Legendre quadrature approximates the integral of a function $f(x)$ over the interval [-1, 1] as follows:

$$\int_{-1}^{1} f(x)dx \approx \sum_{i=1}^{n} w_i f(x_i). \tag{3.9}$$

In the equation above, n represents the quadrature order, w_i resembles the quadrature weights and x_i represents the roots of the n^{th} Legendre polynomial. The weights are defined by the following formula (Abramowitz and Stegun, 1964):

$$w_i = \frac{2}{(1-x_i^2)(P_n'(x_i))^2}, \tag{3.10}$$

where $P_n(x)$ represents the n^{th} order normalized Legendre polynomial. A change of interval must be made to ensure that the Gauss-Legendre quadrature can be applied to all surfaces with contours in the interval [a, b]:

$$\int_a^b f(x)dx = \frac{b-a}{2}\int_{-1}^{1} f(\frac{b-a}{2}\xi + \frac{a+b}{2})d\xi, \tag{3.11}$$

where ξ resembles the transformed coordinate along the contour with the interval [-1, 1]. With this in mind, the Gauss-Legendre quadrature for a line with interval [a, b] can be stated as follows:

$$\int_a^b f(x)dx \approx \frac{b-a}{2} \sum_{i=1}^{n} w_i f(\frac{b-a}{2} x_i + \frac{a+b}{2}). \tag{3.12}$$

3.2.4. Trapezoidal rule

The trapezoidal rule is, just like the Gauss-Legendre quadrature, a method to approximate the integral of a function. This method can be applied to the integral of a function $f(x)$ over the interval [a, b] and is stated as follows:

$$\int_a^b f(x)dx \approx (b-a) \cdot \frac{1}{2}\Big[f(a) + f(b)\Big]. \tag{3.13}$$

The accuracy of the trapezoidal rule method increases when the interval [a, b] is divided into smaller sub-intervals. If the interval would be divided into N sub-intervals with each a length Δx, the trapezoidal rule looks as follows:

$$\int_a^b f(x)dx \approx \sum_{k=1}^{N} \frac{f(x_{k-1}) + f(x_k)}{2} \Delta x_k. \tag{3.14}$$

In this equation, x_{k-1} and k_k represent the lower- and upper limit of the sub-interval with length Δx_k. This method is relatively simple and straightforward as compared to the Gauss-Legendre quadrature method. However, the computational expenses of this method are generally higher than the Gauss-Legendre method (Rao and Sastri, 1996).

3.3. System of equations

3.3.1. Solving linear equations

A set of linear equations is obtained for the CFD simulations after discretizing the equations. This set of equations can be summarized in matrix notation:

$$A\vec{\phi} = \vec{q}, \tag{3.15}$$

where A represents the discretized coefficient matrix, $\vec{\phi}$ is a vector containing variable values and $\vec{q}$ is a vector that contains the discretized values of the sink/source terms. The unknowns, $\vec{\phi}$, are obtained by employing the Strongly Implicit Procedure (SIP), also known as Stone's method (Stone, 1968). This method uses an incomplete LU decomposition to acquire an iterative solution.

3.3.2. SIMPLE algorithm

In order to solve the transport equations, the pressure field must be known. However, the pressure distribution does not have its own equation. Therefore, it must be derived from the continuity equation and the Navier-Stokes equations. In this study, the Semi-Implicit Method for Pressure-Linked Equations (SIMPLE) is used to obtain information about the pressure distribution (Patankar, 1980).

The SIMPLE algorithm can be summarized as follows:

1. An initial guess is made for the pressure- and velocity fields.
2. The Navier-Stokes equations are solved for the intermediate velocity field using the guessed pressure- and velocity fields of the previous step.
3. The corrected pressure field will be solved with the velocity field from the previous step.
4. The new velocity field will be solved with the corrected pressure field.
5. Steps 2-4 are repeated until the solution has converged.

3.3.3. Newton-Rhapson method

The Newton-Rhapson method, also known as Newton's method, is an algorithm used to find the roots of a (set of) function(s). This method is particularly useful in determining the roots of a set of non-linear

functions, which is the case in the steady-state surface energy balance. The Newton-Rhapson method is well described by Grosan and Abraham (2008) and can be explained as follows.

A system of nonlinear equations, f, is defined as:

$$f(x) = \begin{bmatrix} f_1(x) \\ \vdots \\ f_n(x) \end{bmatrix},$$

where $x = (x_1, x_2, ..., x_n)$ and n refers to the number of equations and variables. The system of equations can be linearly approximated in a point x^k, where k stands for the number of iterations. The Jacobian matrix $J(x^k)$ for $f(x)$ can be expressed as:

$$J = \begin{bmatrix} \frac{\partial f_1}{\partial x_1} & \cdots & \frac{\partial f_1}{\partial x_n} \\ \vdots & \ddots & \vdots \\ \frac{\partial f_n}{\partial x_1} & \cdots & \frac{\partial f_n}{\partial x_n} \end{bmatrix}.$$

With the Jacobian known, f can be linearly approximated:

$$f(x_0) = f(x^k + t) \approx f(x^k) + J(x^k)t, \tag{3.16}$$

where $t = x_0 - x^k$ is the deviation between the k-th approximation of the roots, x^k, and the 'true' roots of f, x_0. A geometric interpretation of a linear approximation is shown in figure 3.4.

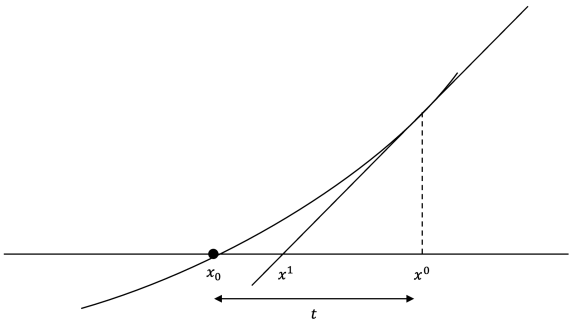

Figure 3.4: Geometric interpretation of a linear approximation of a function.

By setting the right hand side of equation 3.16 to zero, the following can be obtained:

$$J(x^k)t = -f(x^k). \tag{3.17}$$

With this in mind, the Newton-Rhapson algorithm is described below.

1. Guess an approximate solution x^0.
2. Compute $J(x^k)$ and $f(x^k)$.
3. Solve linear system $J(x^k)t = -f(x^k)$ for t.
4. Set $x^{k+1} = x^k + t$.
5. Set $k = k + 1$
6. Repeat steps 2-5 until the solution converges.

3.4. Scaling

In urban simulations, the numerical mesh typically contains large geometries, which can result in high computational costs and inefficient solution methods. To address this issue, scaling can be utilized to

reduce the size of the domain while preserving its original flow characteristics. However, scaling down large geometries to smaller domains can pose challenges, particularly when dealing with governing equations that do not scale linearly with size. In such cases, adjustments to the equations are necessary to accurately represent the larger original equations.

In the present study, the equations are scaled to $O(1)$ equations. This is done by scaling down the domain height to 1 m. This can be mathematically expressed as:

$$x_{\text{sc}} = \frac{x}{H_s}, \tag{3.18}$$

where H_s represents the height of the domain and x_{sc} the scaled domain. The scaling factor can therefore be expressed as:

$$f_{sc} = \frac{1}{H_s}. \tag{3.19}$$

In this study, the velocity variables are left as is; no scaling is applied to the velocity variables. Consequently, for proper scaling, other variables need to be scaled in order for the Reynolds number and the Grashof number to remain the same. The Reynolds number resembles the ratio between inertial forces and viscous forces and is expressed as

$$Re = \frac{UL}{\nu} = \frac{UL_{\text{sc}}}{\nu_{\text{sc}}}, \tag{3.20}$$

where the viscosity is scaled as

$$\nu_{\text{sc}} = f_{sc} \cdot \nu, \tag{3.21}$$

and the length scale is scaled as

$$L_{\text{sc}} = f_{sc} \cdot L. \tag{3.22}$$

The Grashof number resembles the ratio between the buoyancy forces and viscous forces and is expressed as

$$Gr = \frac{L^3 g\beta\Delta T}{\nu^2} = \frac{L^3_{\text{sc}} g\beta_{\text{sc}}\Delta T}{\nu^2_{\text{sc}}}, \tag{3.23}$$

where the thermal expansion coefficient, β, is scaled as

$$\beta_{\text{sc}} = f_{sc} \cdot \beta. \tag{3.24}$$

Besides that, scaling must also be employed for the turbulent characteristics. This means that the ratio between the length scales of the smallest eddies, η_e, and the largest eddies, l_e, must remain the same:

$$\frac{\eta_e}{l_e} = \left(\frac{\eta_e}{l_e}\right)_{\text{sc}}. \tag{3.25}$$

The length scale of the smallest eddies is described by the Kolmogorov length scale:

$$\eta_e = \left(\frac{\nu}{\epsilon}\right)^{1/4}. \tag{3.26}$$

The length scale of the largest eddies, also known as the integral length scale, can be expressed in terms of the turbulent dissipation rate and the turbulent kinetic energy:

$$l_e = \frac{k^{3/2}}{\epsilon}. \tag{3.27}$$

This means that the ratio between the two turbulent length scales can be expressed as:

$$\frac{\eta_e}{l_e} = \frac{(\frac{\nu}{\epsilon})^{1/4}}{\frac{k^{3/2}}{\epsilon}} = \frac{k^{3/2}}{(\nu\epsilon)^{3/4}} = \frac{k^{3/2}}{(\nu_{\text{sc}}\epsilon_{\text{sc}})^{3/4}}, \tag{3.28}$$

where the scaling of ϵ can be put as

$$\epsilon_{\text{sc}} = \frac{\epsilon}{f_{sc}}. \tag{3.29}$$

3.5. Error rates

In this study, two different error rates are used to investigate the quantitative quality of the results. These include the correlation coefficient, ρ_c, and the Normalized Mean Absolute Error, NMAE. The mathematical description of those error rates is discussed below.

The correlation coefficient is given as:

$$\rho_c = \frac{\sum(x_i - \bar{x})(y_i - \bar{y})}{\sqrt{\sum(x_i - \bar{x})^2}\sqrt{\sum(y_i - \bar{y})^2}}, \tag{3.30}$$

whereas the NMAE is given as

$$\text{NMAE} = \frac{1}{N}\sum\left|\frac{(y_i - x_i)}{y_i}\right|. \tag{3.31}$$

In these equations, x_i and y_i refer to the literature values and the modeled values, respectively. The bars over these quantities indicate a sample mean over all N numbers of that quantity. At last, the summations indicate a sum of iterator i over all N quantities.

4

Numerical implementation

In this chapter, a brief overview of the numerical implementation shall be given. This includes an overview of the SEB code used and built in this study and an overview of the coupling approach between the SEB model and CFD.

4.1. Overview of the SEB code

In this study, simulations are done in order to give a virtual description of reality. An overview of the code used in the simulations of the SEB model is given in figure 4.1. The code is written in Python (2023) and all rectangular boxes represent functions within the code. The simulation process can be divided into three stages: pre-processing, main-processing, and post-processing. The first two stages are described in figure 4.1. The pre-processing stage consists of the formation of the grid and the calculation of the view factor. The grid consists of the central points of all facets and their four vertex coordinates. The inputs for the grid generation are the width, W, length, L, and height, H, of the buildings, and the number of facets in all three directions, N_x, N_y and N_z. Subsequently, with the grid generation, the view factor matrix is calculated and stored. This completes the pre-processing stage.

The main-processing stage consists of three principal components. First, the shading factor (also known as the sun-lit factor) is calculated. This requires the solar azimuthal angle and solar zenith angle, which are given as model input and can be found online (NOAA, 2023). Next, the ingoing- and outgoing shortwave radiation on each facet is calculated, which includes multiple reflections. The solar irradiance, I, the diffusive sky radiation, D_{sky}, the albedo, and the absorptivity are given as inputs to the shortwave radiation computations and are based on ASHRAE (2001). This study assumes clear-sky conditions and uses radiative properties that conform to materials such as concrete. Finally, the surface temperatures are computed. This is done by taking the view factor, the shortwave radiative fluxes, the conduction parameters and convection parameters. Again, the conduction parameters are based on values conforming to that of concrete. The convection parameters, however, are based on CFD. The coupling process between CFD and the SEB model is described in the next section.

After the main-processing stage, the post-processing stage follows. This stage consists of analyzing the data through plotting, error rates, or other types of tools. Besides that, in this stage the surface temperatures are exported to CFD as surface boundary conditions. CFD data analysis is done in Tecplot (2022), where, among others, different (3D or 2D) contour plots can be made.

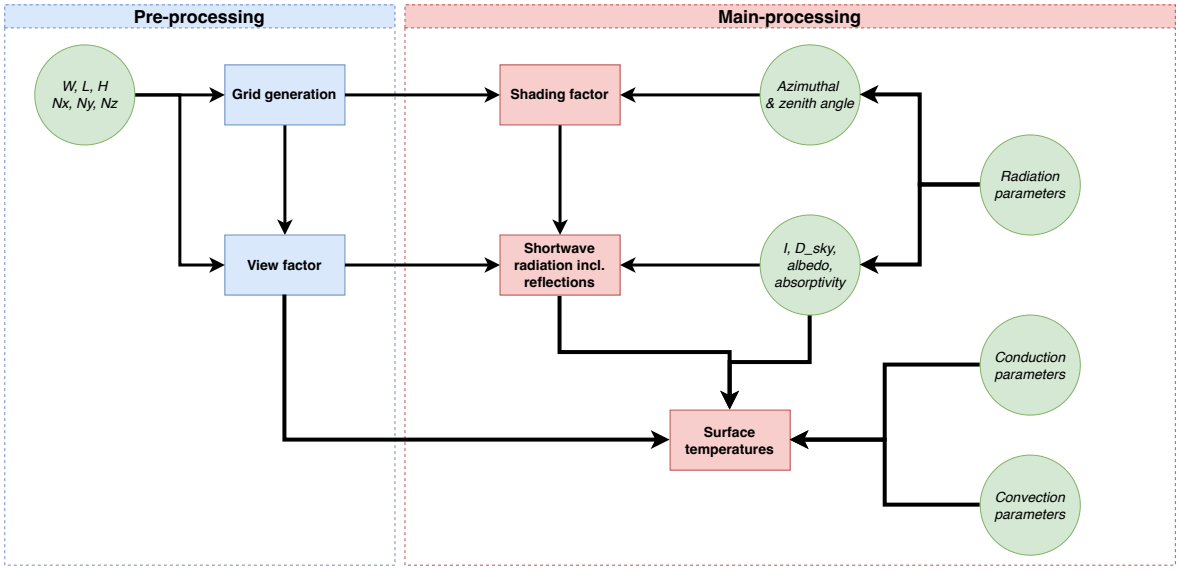

Figure 4.1: An overview of the SEB code. The blue area and boxes indicate the pre-processing stage and functions, respectively. The red area and boxes indicate the main-processing stage and functions, respectively. The green highlighted boxes designate input values and parameters.

4.2. Coupling between SEB model and CFD

In order to compute the surface temperatures, convection parameters are needed. Therefore, this requires coupling between the SEB model and CFD. In this study, the in-house CFD code is used, which is mainly written in Fortran (2021). A detailed overview of this code can be seen in the master thesis of de Bruin (2022). Coupling is done in two ways (see figure 4.2). The first approach couples the two by extracting the turbulent viscosity of the CFD simulation and giving it as input to the SEB model. This method uses the nearest neighbor estimate to relate the CFD cells to the SEB facets. The second approach couples the two by computing surface temperatures with the SEB model and giving it as input to the CFD model. It must be noted that both approaches are one-way coupling approaches. This means that one model influences the other, but not the other way around. The model could be extended to two-way coupling by combining the two one-way coupling approaches.

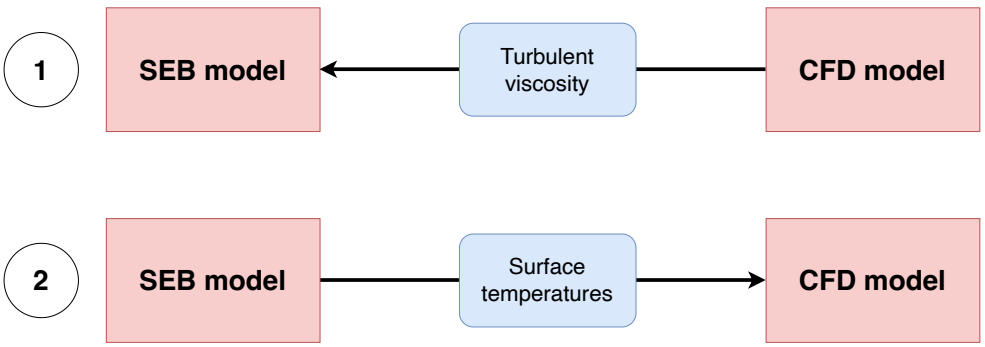

Figure 4.2: An overview of the two different one-way coupling approaches used in this study.

5

Results and Discussions

5.1. Case 1: Validation of the shortwave radiation model

The shortwave radiation model is validated with the experimental albedo data from Aida (1982). In Aida's famous experimental study, the effect of surface irregularity of an urban structure on the anomalous absorption and reflection of incident solar radiation is examined. Specifically, the diurnal variation of the effective albedo of three urban structures is studied. The effective albedo of an urban structure is defined as the ratio between the incident radiation on the urban structure and the radiation reflected by the urban structure. This, therefore, tells something about the reflectivity of an urban structure. In the present model, the diurnal variation of the effective albedo is compared with Aida's measurements. Aida's measurements were performed on the top of a building on the campus of Yokohama National University in Japan. The global solar radiation and the reflected radiation from the urban structures were observed by Aida with an accuracy of 95 %.
Besides comparison with Aida's data, the current model is also compared to simulated data of Schrijvers (2020). Schrijvers' radiation model is based on the Monte Carlo method, which is significantly more computationally expensive than the current model.

5.1.1. Simulation set-ups

The diurnal variation of the effective albedo is determined for two days: December 3rd, 1977, and June 15th, 1978. These dates correspond to the measurement dates of Aida. The sun's azimuthal angle, ϕ_s, and the sun's zenith angle, θ_s, of those specific days are extracted from the site of National Oceanic and Atmospheric Administration (NOAA, 2023). These angles can be found in appendix C.

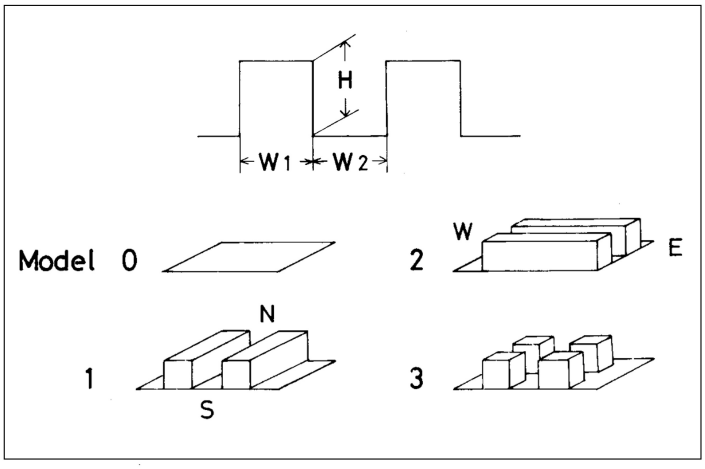

Figure 5.1: An overview of the geometric models used in the shortwave radiation model validation (Aida, 1982).

The geometric models used by Aida and also in this study are schematically displayed in figure 5.1. Geometric model 0 represents a flat surface, models 1 and 2 represent street canyons with different orientations, and model 3 represents a patched block canyon. In the present study and Aida's study, the width of the canyon, W_2, and the width of the building, W_1, are equal, i.e., $W_1 = W_2 = W$. In his experiments, Aida used geometric model 0 as a reference case to study the diurnal variation of the albedo factor of a flat surface. In this study, these diurnal varying values are used to determine the effective albedo of geometric models 1, 2, and 3. Specifically, these values are used as albedo factor of the roofs of the buildings in geometric models 1, 2, and 3, as is done in literature (Fortuniak (2008); Arnfield (1988)). In table 5.1, relevant simulation parameters are given that are used for the December and June simulations. The albedo factor of 0.40 corresponds to that of concrete and the values for the solar irradiance and diffusion factor are taken from ASHRAE (2001). The diffusive sky radiation is then defined as $D_{\text{sky}} = C \cdot I$, where C is the diffusion factor. The SEB model assumes clear-sky conditions, which was also the case for Aida's experiments.

Parameter	December	June
Albedo factor, α (-)	0.40	0.40
Diffusion factor, C (-)	0.057	0.177
Solar irradiance, I (Wm^{-2})	1417	1336

Table 5.1: Parameter values for the simulations done for the two days that are considered: 3$^{\text{rd}}$ of December 1977 and 15$^{\text{th}}$ of June 1978.

Parameter	Model 1	Model 2	Model 3
Height over width ratio, H/W	1	1	1
Length over width ratio, L/W	100	100	1
Facet grid size, ($N_i \times N_j$)	5×5	5×5	3×3
Gauss-Legendre order	150	150	50

Table 5.2: Parameter values for the simulations done for the two days that are considered: 3$^{\text{rd}}$ of December 1977 and 15$^{\text{th}}$ of June 1978. Here, the models 1, 2, and 3 refer to the used geometric models.

The pre-processing parameters for the different geometric models are given in table 5.2. It must be noted that the length-over-width ratio is high for geometric models 1 and 2. This is done to mimic an infinite canyon and, subsequently, to reduce edge effects, such as an increased sky-view factor near the edges of the canyon. The values for the facet grid size and Gauss-Legendre order were determined after a parametric study. More on this in the discussion in the next section.

In the model 3 case, extra walls are placed around the domain to mimic the infinite 3D canyon which is used by Aida. This type of geometry is shown in figure 5.2 and is based on Grylls et al. (2021). The walls are placed at the same distance, W, from the buildings and have a height, H, equal to the buildings' heights.

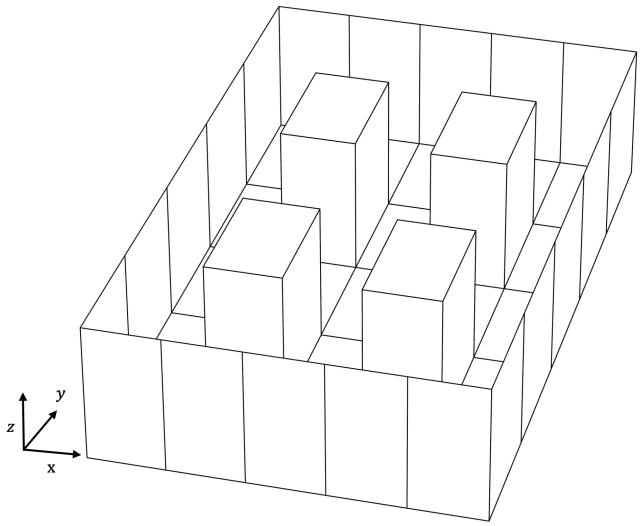

Figure 5.2: An overview of the geometry of model 3 used in this study. The walls around the domain have the same height as the buildings.

5.1.2. Results

In this section, the simulation results obtained with the aforementioned parameter values are compared to experimental values for geometric models 1, 2, and 3. Besides that, different parametric studies have been done. These include a study of the convergence of the shortwave radiation after many reflections, a study of the effect of the number of slices in the vertical direction on the albedo factor, a view factor convergence and validation study, and a validation study of the sun-lit factor. First, the simulation results for the effective albedo will be discussed.

Effective albedo

In this subsection, the simulation results for the effective albedo are compared to measurement values of geometric models 1, 2, and 3, which are schematically displayed in figure 5.1. Besides experimental data of Aida (1982), the simulation results of Schrijvers (2020) are also included in the validation of model 3. These results are obtained from a Monte-Carlo-based radiation model. The results for all three geometric models are presented in figure 5.3. In all figures, the experimental results for geometric model 0 and a fit through these results are given. This is done to showcase the diurnal variability of the albedo factor of a flat surface. The quantitative results are given in table 5.3.

Qualitatively speaking, the simulation results for model 1 and model 2 are in good agreement with the experimental data. This can be backed up with quantitative measures, such as the correlation coefficient, ρ_c, and the Normalized Mean Absolute Error (NMAE), which are given in table 5.3. The early morning and late afternoon results for both model 1 and model 2 in December, however, slightly deviate from the experimental results.

The results for model 3 are in lesser agreement with the experimental values, as compared to models 1 and 2. The model 3 results show a decent qualitative similarity with experimental values, but the quantitative results, however, do not show good agreement with experimental results. The results do not show a good correlation with the experimental data and the average error falls outside the measurement uncertainty. The results of the present study do seem to slightly outperform the Monte-Carlo-based results of Schrijvers. Especially considering that the computational time of Monte-Carlo-based simulations is significantly longer than non-Monte-Carlo-based computations.

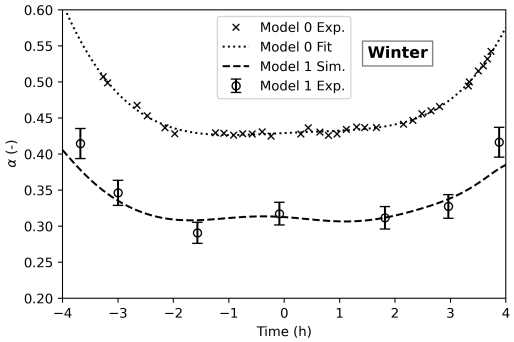

(a) Model 1 (December 3rd, 1977).

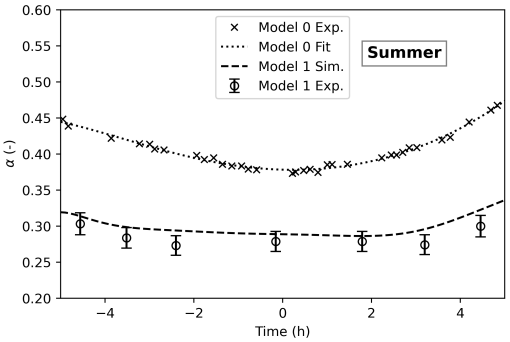

(b) Model 1 (June 15th, 1978).

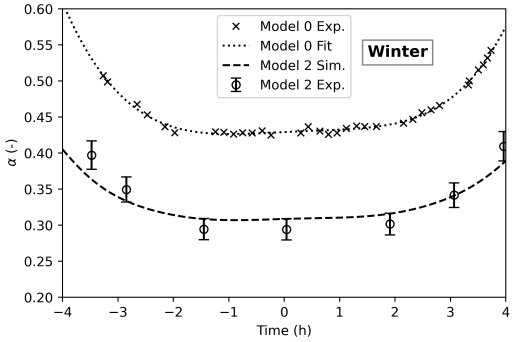

(c) Model 2 (December 3rd, 1977).

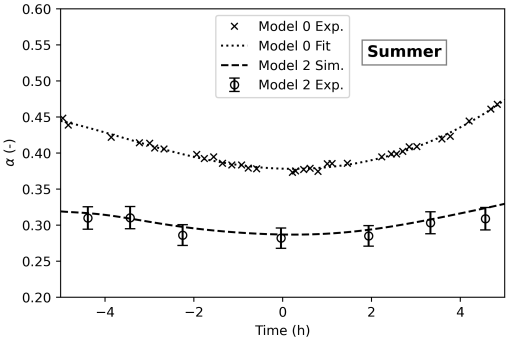

(d) Model 2 (June 15th, 1978).

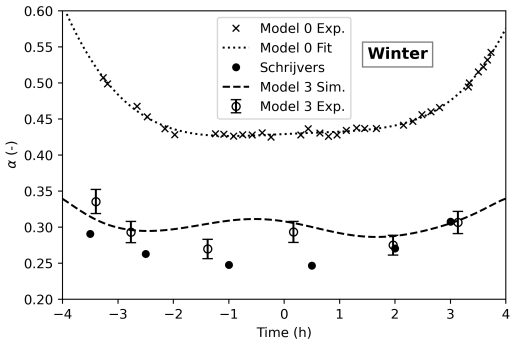

(e) Model 3 (December 3rd, 1977).

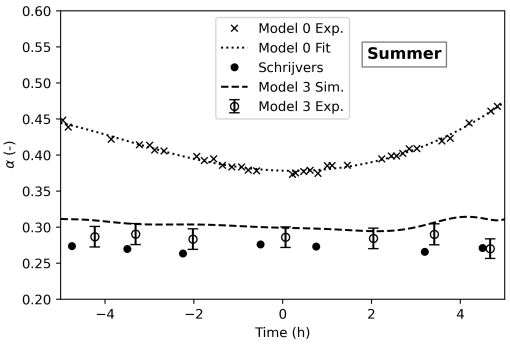

(f) Model 3 (June 15th, 1978).

Figure 5.3: Comparison of the simulated results with the experimental results of the effective albedo of geometric models 1-3. The horizontal axis designates the time in hours relative to noon and the vertical axis designates the effective albedo factor. All error bars resemble an error of 5 %. *Note: Both Aida's and Schrijvers' data are digitized.*

Error rate	Model 1 (Dec/Jun)	Model 2 (Dec/Jun)	Model 3 (Dec/Jun)
Correlation coefficient, ρ_c (-)	0.98/0.88	0.98/0.92	0.62/-0.57
Normalized Mean Absolute Error (%)	4.47/5.44	4.76/2.50	5.2/6.9

Table 5.3: Quantitative comparison of simulated results and experimental results for geometric models 1-3.

One of the possible reasons for this deviation is the angular- and spectral dependence of the albedo factor. For simplicity, in this study, the albedo factor inside the canyon is kept constant at 0.40. However, since the albedo factor is dependent on the angle of the sun, as is seen from the model 0 experimental data, this could lead to some deviations from the experimental values of the effective albedo. Besides that, the

spectral dependency of the albedo factor is also not taken into account in this study. Since the spectral intensities of the incident radiation may vary during the day, due to a different atmospheric decomposition.

Another possible reason behind the deviation of the simulated effective albedo is the uncertainty in the experimental design of Aida. In Aida's experiments, the incident- and reflected radiation is measured by one upward-looking pyranometer and one downward-looking pyranometer. The position of the downward-looking pyranometer was kept 0.3 m above the top of the blocks at the center in all three models. Although Aida stated that about 95 % of the radiation is captured by the pyranometers, it is not clearly stated from which specific area of the model setup this radiation is coming. This could have led to a mismatch in the simulated effective albedo.

Besides the uncertainty in Aida's results, the assumption that reflections are diffusive and that the radiosity (radiant flux leaving a surface) is uniform across the facets could also have led to the deviation from Aida's results. In this study, reflections are assumed to be diffusive and no specular reflections are taken into account. It could be that for certain sun positions the total amount of reflected radiation is therefore higher or lower than the experimental value.

In the upcoming sections, the impact of other factors that play a role in determining the effective albedo will be studied. First, the view factor convergence and validation will be discussed.

View factor convergence rate and validation

The view factor algorithm is tested for three geometries (cases) for which the analytical value for the view factor is known. The analytical formulae and the geometries for the three cases are given in appendix A. First, the Gauss-Legendre quadrature method is tested against the trapezoidal rule for its accuracy and speed. The results for the view factor calculation of case 1 are shown in figure 5.4. The results show the superiority of the Gauss-Legendre method over the trapezoidal method in speed and accuracy. Although the trapezoidal method converges to the analytical value when the order increases, the Gauss-Legendre method converges even faster with lower computational costs. The calculated values for the other two cases show similar behavior and are given in table A.1.

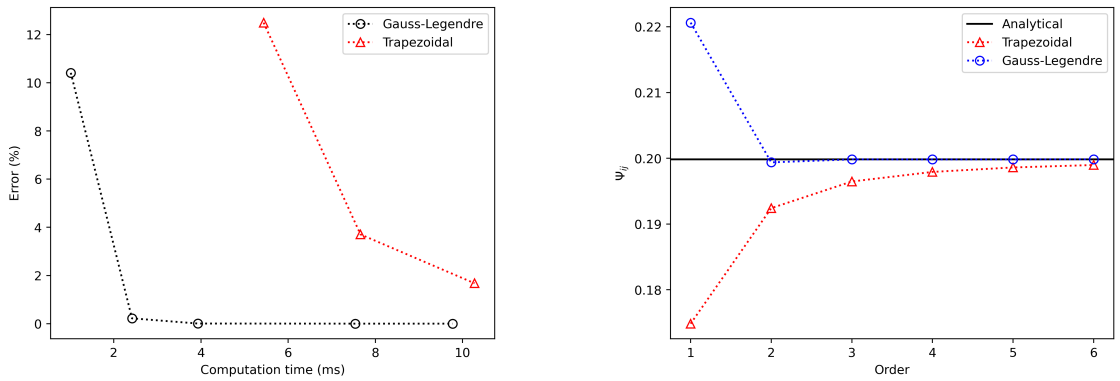

Figure 5.4: Two comparisons between the Gauss-Legendre method and the Trapezoidal method for calculating the view factor of case 1 (see appendix A). In subfigure (a) the computation time is compared with the relative error for different orders of the two methods. In subfigure (b) the value for the calculated view factor is set against the number of line segments used the analytical value.

In figure 5.5, a view factor convergence study is presented. The maximum relative change in the view factor is shown for increasing Gauss-Legendre order and for three different canyon L/W ratios. It can be seen that for a low L/W, the view factor converges rather fast. However, for $L/W = 100$ the view factor needs a high Gauss-Legendre order to converge. Therefore, in the model 1 experiment of Aida, an order of 150 is chosen to make sure the view factor has converged.

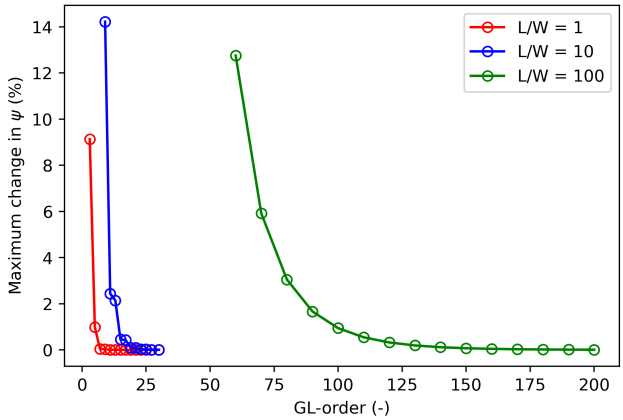

Figure 5.5: The maximum percentage change of the view factor is plotted against the Gauss-Legendre order for three different L/W ratios: 1, 10, and 100. The view factor of the north-south oriented street canyon (geometric model 1).

Effect of grid refinement

The effect of grid refinement on the effective albedo factor will be discussed in this subsection. This is studied for model 1, the N-S oriented canyon, and for three different solar zenith angles: 10 °, 45 °, and 80 °. The solar azimuthal angle is kept constant at 90 °, such that the solar position is perpendicular to the canyon. The results are presented in figure 5.6. In figure 5.6a, the effective albedo factor of the canyon (roofs excluded) is given against the number of slices in the vertical direction. The number of slices basically resembles the amount of grid cells in the vertical direction. In figure 5.6b, the percentage change in the albedo factor is presented against the number of slices.

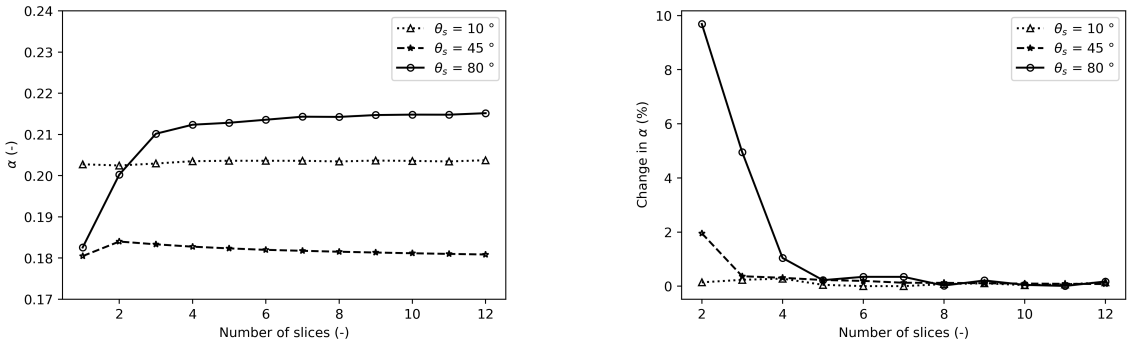

(a) (b)

Figure 5.6: Figure (a) shows the effective albedo of a north-south oriented street canyon versus the number of slices in the vertical direction for three different solar zenith angles. Figure (b) shows the relative change in the albedo versus the number of slices for three different zenith angles.

As can be seen from the figures above, the albedo factor converges asymptotically with an increase in the number of slices. This shows that after approximately 5 grid cells in the vertical direction the albedo factor has converged and further grid refinement has little effect on the outcome of the effective albedo. This is in line with what is found by Fortuniak (2008).

Sun-lit factor validation

The sun-lit factor validation is done by evaluating the sun-lit factor at four different times during the day, each with a corresponding solar azimuthal- and zenith angle. The results are shown in figure 5.7. In these plots, the sun-lit factor can be interpreted as a shadow with different intensities. The black color resembles a full shading and white represents a fully sun-lit facet, i.e., no shading. The solar positions correspond to the 21st of June in Amsterdam.

The results show realistic shadow patterns for the different times during the day. The shadows rotate around the z-axis, which corresponds to the rotation of the sun during the day. Besides that, the shadow length gets shorter around noon (figure 5.7c), which corresponds to a lower solar zenith angle during the middle of the day. Overall, it can be said that the sun-lit factor correctly calculates the shadows formed by objects, such as buildings.

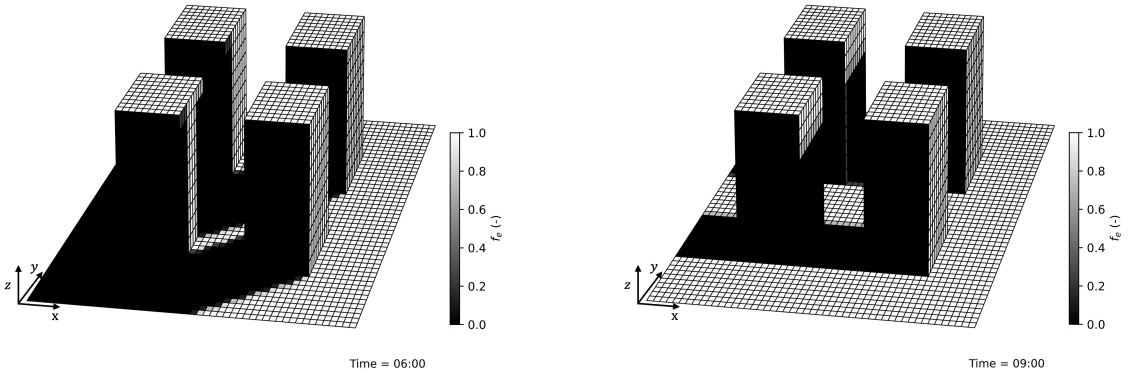

(a) $\phi_s = 56°$, $\theta_s = 86°$

(b) $\phi_s = 103°$, $\theta_s = 51°$

(c) $\phi_s = 215°$, $\theta_s = 33°$

(d) $\phi_s = 277°$, $\theta_s = 65°$

Figure 5.7: Four images showing the sun-lit factor of each facet at different times during the day. The solar positions correspond to the 21st of June in Amsterdam. The camera angle is set at an elevation angle of 22° and an azimuthal angle of 169° measured clockwise from the positive y-axis. In these images, the positive y-axis represents the true north.

Shortwave radiation convergence rate

In this subsection, the convergence rate of the shortwave radiation after multiple reflections is presented. The incoming shortwave radiation on different facets after each reflection is presented in figure 5.8a. All four different colors indicate a different type of facet (east-facing, west-facing, etc.). In figure 5.8b, the fraction difference between each subsequent reflection is presented with the reflection criterion, ϵ_c, given as a dashed horizontal line. The parameters and their values used in this specific study are listed in table 5.4.

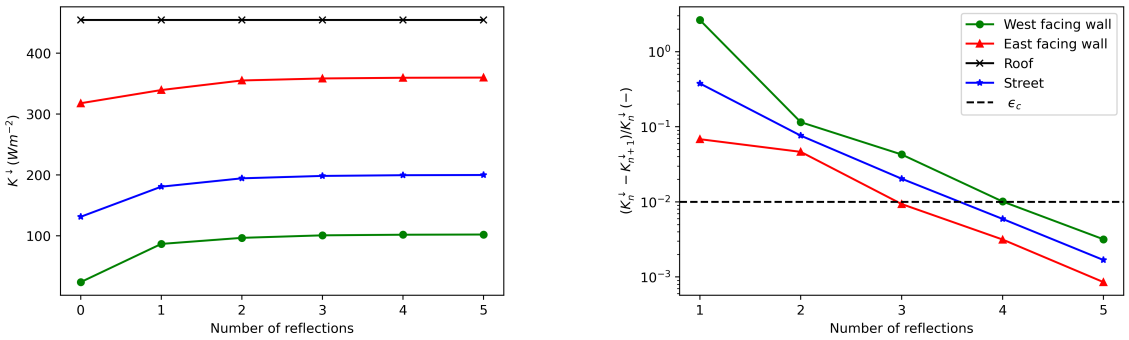

(a) (b)

Figure 5.8: Figure (a) represents the incoming shortwave radiation after each reflection striking differently oriented facets. Figure (b) shows the relative error in the shortwave radiation after each reflection. The dashed line resembles the convergence criterion, ϵ_c.

Parameter	Value
Albedo factor, α (-)	0.70
Diffusion factor, C (-)	0.1
Solar irradiance, I (Wm^{-2})	500
Reflection convergence criterion, ϵ_c (%)	1
Sun azimuthal angle, ϕ_s (°)	90
Sun zenith angle, θ_s (°)	36

Table 5.4: Parameter values for the simulations done for evaluating the convergence rate for the shortwave radiation after multiple reflections.

As can be seen from figure 5.8, the shortwave radiation striking each facet nicely converges after 5 reflections. This is in line with the number of reflections needed for convergence by Grylls et al. (2021), which is in the range of 5-10.

5.2. Case 2: Infinite street canyon

The infinite street canyon case is used to validate different parts of the SEB model. These parts include the longwave radiation model, the conduction model, and the sensible heat flux model. The results are compared with case study results of Schrijvers (2020). In this case, the effect of different height-over-width ratios (H/W) of the street canyon on different surface energy fluxes and the surface temperature is investigated.

5.2.1. Simulation set-ups

Three different cases are considered for the evaluation of the different parts of the SEB model. These include the case of radiative equilibrium (case 01), the case where the conductive heat flux is added (case 02), and the case where the sensible heat flux is also added (case 03). An overview of these cases is given in table 5.5. For all three cases, different H/W ratios of an infinite street canyon are considered. The geometry used in the SEB model is schematically shown in figure 5.9. In this figure, the red highlighted area shows the slice that is taken from the 3D simulation to convert it to a 2D approximation. This approximation can be done since the solar azimuthal angle is 270 °, which falls exactly in the x-z plane. On the right-hand side of figure 5.9, the 2D case is schematically shown where each part of the canyon has a specific number, which is later used in plotting.

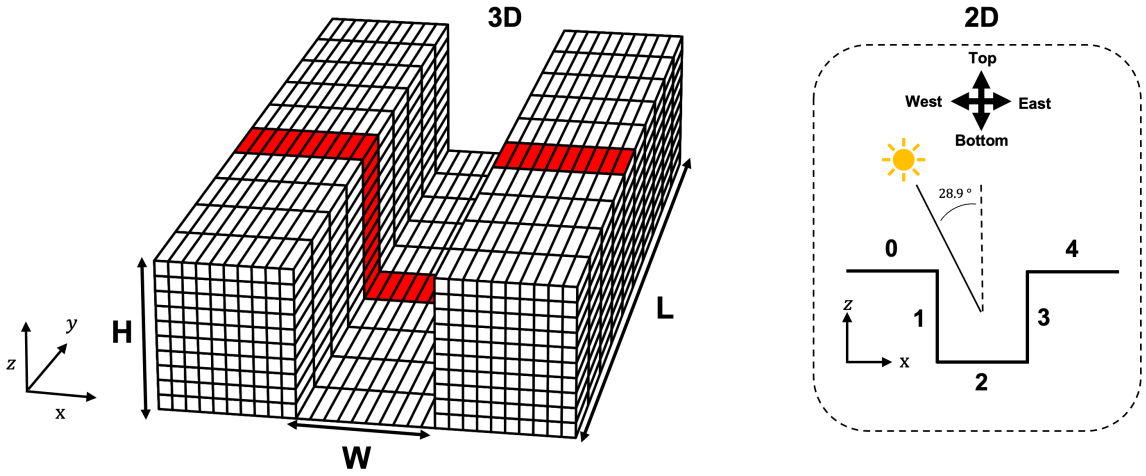

Figure 5.9: A schematic representation of the geometry used in this case study. A slice (marked in red) is taken from the 3D model to convert the results to 2D. The different parts of the slices are numbered according to the inset shown on the right. This numbering is also used in the plots later in this section. In this case study, the positive y-axis represents the true north.

Case	K	L	G	H
01	+	+		
02	+	+	+	
03	+	+	+	+

Table 5.5: The three cases which are considered in this study. Case 01 represents the case in radiative equilibrium, case 02 is the case where the conductive heat flux is added, and case 03 is the case where the sensible heat flux is also added to the equation.

In order to model the sensible heat flux, the SEB model is coupled with the in-house CFD code. The CFD simulation set-up is shown in figure 5.10. The set-up consists of an array of 14 street canyons which are placed a distance W apart. Air with a constant and homogeneous velocity, U_{in}, is given as input to the domain. By using an array of obstacles, the most downwind street canyons experience a fully developed flow pattern, which is similar to the case of Schrijvers (2020). One-way coupling between the SEB model and CFD model is done by extracting the turbulent viscosity profile from the street canyon between block 12 and block 13. Subsequently, the turbulent viscosity profile is put into the sensible heat flux part of the SEB.

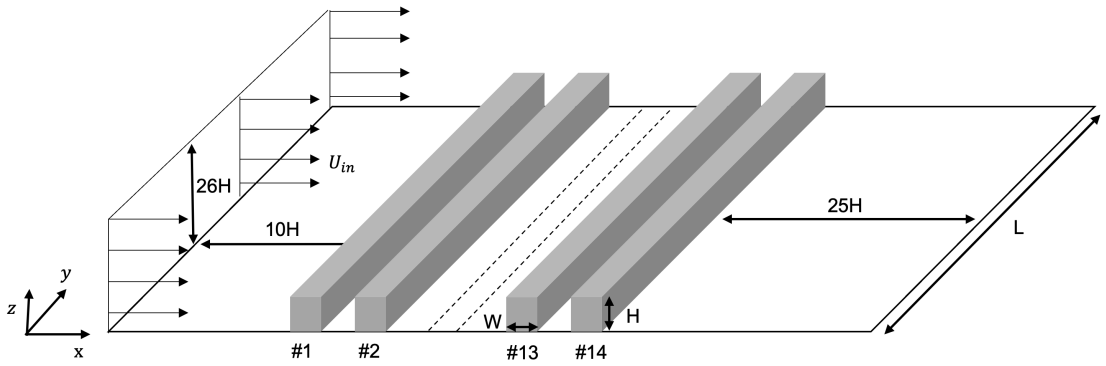

Figure 5.10: A schematic representation of the simulation set-up for the CFD simulations. For imaging purposes, the two dotted lines indicate the part where obstacles 3-12 are left out.

In table 5.6, all geometric values are given for the three different H/W ratios. In this table, N_x, N_y, and N_z indicate the number of facets along the different directions.

Parameter	$H/W = 0.5$	$H/W = 1$	$H/W = 2$
Canyon width, W (m)	50	25	25
Canyon length, L (m)	150	150	150
Canyon height, H (m)	25	25	50
Facet grid size $(N_x \times N_y \times N_z)$	$(10 \times 1 \times 10)$	$(10 \times 1 \times 10)$	$(10 \times 1 \times 10)$

Table 5.6: Geometric values for the three different H/W ratios. The main distinguishing factor for the models is their height-over-width ratio.

In table 5.7, all relevant parameter values used in this study are given, which match the parameter values used in Schrijvers' study. The radiation intensities and solar angles correspond to solar noon in Amsterdam, the Netherlands, on June 21st. An overview of the solar angles can be found in appendix C. The conductive and radiative material properties correspond to typical values for brick and concrete and are taken constant over all surface areas. The layer thickness, however, is different for street surfaces and building surfaces. At this thickness, d, the temperature is kept at a constant temperature T_∞. For buildings, this can be interpreted as an extremely efficient air-conditioning unit able to maintain a constant temperature at a specified distance. This results in energy generation or dissipation at distance d inside the material.

	Radiation
Diffusive sky radiation, D_{sky}	84.2 Wm^{-2}
Longwave absorptivity, ζ	0.95
Longwave emissivity, ε	0.95
Longwave sky radiation, L_{sky}	325 Wm^{-2}
Shortwave albedo factor, α	0.40
Solar azimuthal angle, ϕ_s	270 °
Solar irradiance, I	950 Wm^{-2}
Solar zenith angle, θ_s	28.9 °
	Heat conduction
Interior temperature, T_∞	293 K
Thermal conductivity, λ	0.72 $Wm^{-1}K^{-1}$
Thickness building, d	0.25 m
Thickness street, d	1 m
	Computational Fluid Dynamics
Air temperature, T_a	20 °C
Cell expansion factor	1.1
Inlet velocity, U_{in}	4 ms^{-1}
Minimal cell size	$(x \times y \times z) = (1m \times 1m \times 1m)$
Maximum cell size	$(x \times y \times z) = (25m \times 25m \times 25m)$

Table 5.7: All parameter values used in this case study if not stated otherwise. These values are based on Schrijvers (2020).

5.2.2. Results

In this section, the simulation results of the current study will be compared to the simulations of Schrijvers (2020). These results include the surface energy fluxes, the surface temperatures, the effect of grid refinement, and the diurnal variation of the surface energy fluxes and surface temperatures. First, the results for the surface energy fluxes will be discussed.

Surface energy fluxes

The surface energy fluxes of case 01 will be discussed in this subsection for three different H/W ratios. This case resembles a situation where only shortwave radiation and longwave radiation fluxes are present in the surface energy balance. Four different energy fluxes are considered: the net shortwave radiation, K, the diffusive longwave radiation, L_{sky}, the environmental longwave radiation, L_{env}, and the outgoing longwave radiation, $L^{\uparrow}$. The results for the four different fluxes are given in figure 5.11. The horizontal axes show five different regions which correspond to the inset shown in figure 5.11c and on the right-hand side in figure 5.9. All the scaled distances represent normalized distances. The three different colors represent the three different H/W ratios and the dashed line corresponds to Schrijvers' data. The correlation coefficient and NMAE are also computed for all energy fluxes. These values can be found in appendix B.

Qualitatively speaking, the simulated surface fluxes are in good agreement with the results of Schrijvers. All results have a very similar shape as Schrijvers' data and show a high correlation, which is backed up by the correlation coefficients found in appendix B. The $H/W = 2$ case, however, does show a discrepancy, which is most evident in figure 5.11d. The possible reasons for this will be discussed further in this section.
The NMAE values also show, in general, a good agreement with the results of Schrijvers. For the $H/W = 1$ case, all NMAE values fall below 5.5 %. The $H/W = 0.5$ case shows similar results except for the net shortwave radiation flux where the NMAE is 12 %. The $H/W = 2$ case underperforms in this respect, with the NMAE for the net shortwave radiation at 12.3 % and for L_{sky} at 13.7 %.

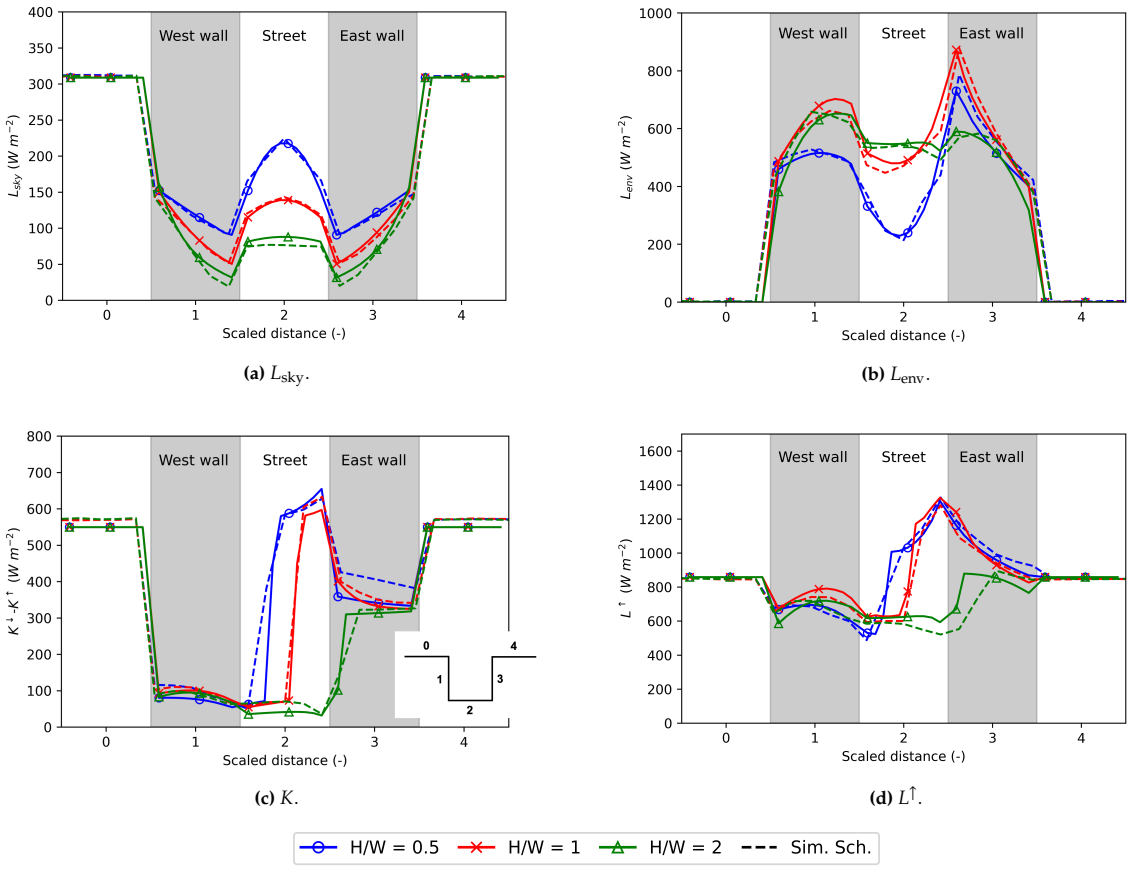

(a) L_{sky}. **(b)** L_{env}. **(c)** K. **(d)** $L^{\uparrow}$.

Figure 5.11: Comparison of the simulated surface energy fluxes and the results of Schrijvers (2020) for three different H/W ratios for case 01. In all plots, the vertical axis shows the energy fluxes in Wm^{-2} and the horizontal axis shows the scaled distance, which is in accordance with the inset in figure (c). Figure (a) shows the incoming longwave radiation from the sky, figure (b) shows the environmental longwave radiation, figure (c) shows the net shortwave radiation, and figure (d) shows the outgoing longwave radiation. *Note: Schrijvers' data is digitized.*

Although the digitization of Schrijvers' results has been done with much care, this could be a possible reason for the deviation from Schrijvers' results. Besides that, since Schrijvers did not provide an average of his Monte Carlo simulations, the results were quite noisy. In the example of net shortwave radiation on a flat surface, Schrijvers' results show a deviation of approximately 3-4 % from the mean. The combination of digitization and noisiness of Schrijvers' results could therefore lead to the (small) mismatch between the current study and Schrijvers'.

Another possible reason for the deviation is the 2D approximation. Schrijvers' results are from a 2D model where his results are taken from line elements. The current model, however, is fully 3D, and the found values are therefore taken from surface area elements. A ramification of this is the mismatch in boundary conditions. Schrijvers employs periodic boundary conditions in the north and south direction of the canyon. This means that radiation emitted or reflected by surfaces can only strike other surfaces or leave the canyon through the top side of the canyon. In the current 3D model, no periodic boundary conditions have been employed. This means that radiation can also leave the canyon through the north and south side of the canyon. Besides that, the canyon has a finite length, which also influences the temperatures inside the canyon. This is due to the change in geometric proportions (L/H or L/W), which causes a change in the view factor. The mismatch in boundary conditions and the finite canyon length could therefore be part of the drivers behind the deviation from Schrijvers' results.

A third possible reason behind the deviation from Schrijvers' results is the accuracy of Schrijvers' results itself. The results of $L^{\uparrow}$, for example, show quite a mismatch in the $H/W = 2$ case. Schrijvers' results

show a peak in the middle of the east wall, while the current study's results show a peak at the beginning of the east wall. If we take into account a solar zenith angle of 28.9 °, the sun-lit part of the east wall begins at approximately 0.1H for the $H/W = 2$ case. This can be seen by the peak of K in the east wall of the current study's results. With that in mind, it would seem reasonable that $L^{\uparrow}$ would also peak at the same position. This is the case for the current study, but not for Schrijvers' results. Therefore, it could very well be that Schrijvers made a mistake in plotting or processing his data.

Surface temperatures

In this subsection, the simulated surface temperatures will be discussed and compared with Schrijvers' results for cases 01, 02, and 03. The results are shown in figure 5.12, where each subplot designates a different H/W ratio. The black color indicates case 01, the blue color resembles case 02, and the red color designates case 03. The dotted line is literature data from Schrijvers (2020). The NMAE and correlation coefficient of the surface temperatures are given in appendix B.

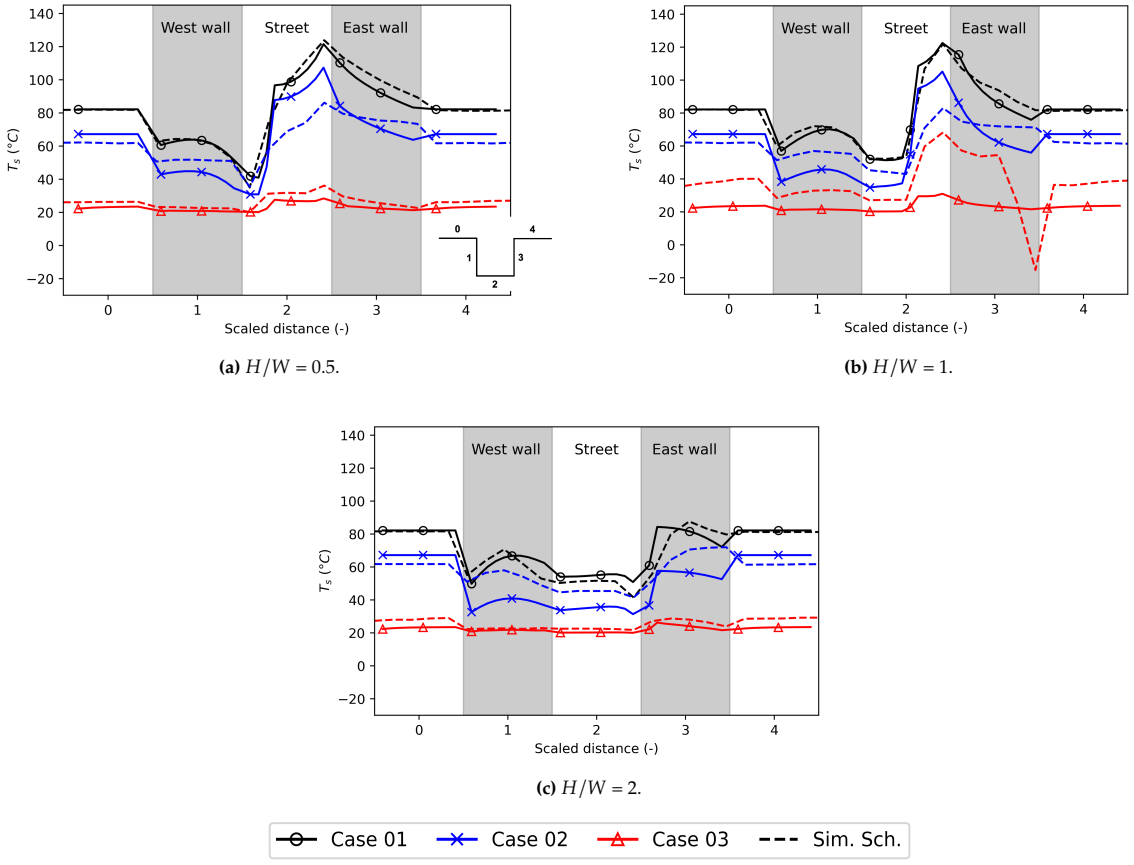

(a) $H/W = 0.5$.

(b) $H/W = 1$.

(c) $H/W = 2$.

Figure 5.12: Comparison of the simulated temperatures of the current study and Schrijvers' simulations for the three cases. The horizontal axis shows the scaled distance of the five different parts of the 2D canyon, which are schematically given in figure (a). The black color indicates case 01, the blue color resembles case 02, and the red color designates case 03. *Note: Schrijvers' data is digitized.*

The results for case 01 show a good qualitative agreement with Schrijvers' results. This is in line with the results of the surface fluxes discussed in the previous subsection. Since $L^{\uparrow}$ is a function of T_s, the results for T_s are directly linked to the results of $L^{\uparrow}$ in case 01. As was seen in the previous subsection, the result for the $H/W = 2$ ratio shows the largest deviation from Schrijvers, both qualitatively and quantitatively. The possible reasons behind the deviation were discussed in the previous subsection.

The results for case 02 show a lesser agreement with Schrijvers' results. The results still acquire a correlation of more than 0.75 and show a similar shape as Schrijvers' data. The values of the surface

temperature, however, do give a larger deviation, which can be seen qualitatively and is also backed up quantitatively by the NMAE values.
The most obvious reason for deviation in the results for case 02 is the difference in boundary conditions for the conductive heat flux, G. In the current study, the boundary condition is modeled by assigning a fixed interior temperature T_∞ at a distance d inside the material. Schrijvers, however, employs a zero-flux boundary condition at a distance d inside the material. In his study, Schrijvers did a comparison between these two different boundary conditions and their effect on the surface temperature. This was done in a case where, next to the conductive heat flux, the sensible heat flux was also added. These results showed differences in surface temperatures between 1-30 K. Since the results for case 01 showed a good agreement and all conduction parameter values are similar to Schrijvers', it is very likely that the mismatch is due to the difference in boundary conditions.

At first, the results for case 03 show a relatively good qualitative agreement for $H/W = 0.5$ and $H/W = 2$, but show a bad agreement with $H/W = 1$. The quantitative results, however, do show quite a discrepancy between the current study's results and Schrijvers'. The NMAE values are all above 12 % and the correlation coefficients are all below 0.9.
The mismatch in surface temperatures in case 03 could be due to the difference in the boundary conditions of the conductive heat flux. As was seen above, the differences between literature surface temperatures and this study's surface temperatures for case 02 were quite significant. However, for case 03, the sensible heat flux is dominant. This can be seen from the surface energy fluxes plot (figure 5.17), which will be discussed later. Therefore, the effect of the error in the conductive heat flux is not likely to be the main driver behind the mismatch in case 03.

A likely possible driver behind the error in case 03 is the difference in coupling between CFD and SEB; this study uses a simplified one-way coupling, whilst Schrijvers uses a two-way coupled approach. The implementation of the sensible heat flux was highly simplified in this study by assuming a constant surrounding air temperature. This can lead to an over-cooling of the surface temperatures (or over-heating if $T_a > T_s$), which therefore explains the underestimation compared to Schrijvers' results.

A second likely possible driver is the method of computation of the temperature gradient in the sensible heat flux. The gradient is computed by taking the difference between T_a and T_s and dividing this over the wall distance. Here, T_a is fixed and T_s is solved for. The distance from the wall, however, over which the gradient is taken is unclear. In this study, a constant wall distance of 0.5 m is assumed. This distance corresponds to the cell size near the walls. This wall distance, however, does greatly influence the surface temperatures. The dependency of the surface temperature on this wall distance could therefore be one of the possible drivers behind the error in case 03.

A third possible driver is the method of extraction of ν_t from the CFD simulation to the SEB model. In this case study, the near-surface values of ν_t are extracted and subsequently interpolated to match the coordinates of the facets of the canyon. In this process, accuracy can be lost due to two reasons. First, since the interpolation is an estimation, it can lead to inaccuracies. Second, the near-surface ν_t values are taken from a finite distance from the wall which is equal to the cell size. This could also lead to inaccuracies since there could be a variation of ν_t within the cell itself.

The most significant deviation from Schrijvers for case 03 is found with $H/W = 1$. This shows large differences in peak temperatures of about 30 K. However, there does seem to be an inconsistency in Schrijvers' results. The $H/W = 1$ results for case 03 of Schrijvers show a much larger surface temperature profile than $H/W = 0.5$ and $H/W = 2$. This does physically not make sense, since all variables stay put except the H/W ratio. Besides that, Schrijvers' results show unphysical behavior on the east wall of $H/W = 1$, where a sharp decrease in surface temperature is found. Schrijvers explains that this is due to a local very high ν_t. Therefore, it could be that Schrijvers' results for $H/W = 1$ are inaccurate and thus lead to the deviation from the current study's results.

Effect of grid refinement

In this subsection, the effect of grid refinement on the surface temperature distribution will be discussed. This will be discussed for cases 01 and 02 with $H/W = 1$. The canyon grid is refined in 5, 8, 10, and 15 horizontal and vertical slices. The surface temperatures for these four different cases are given in figure 5.13. This figure shows two surface temperature distributions for case 01 (a) and case 02 (b).

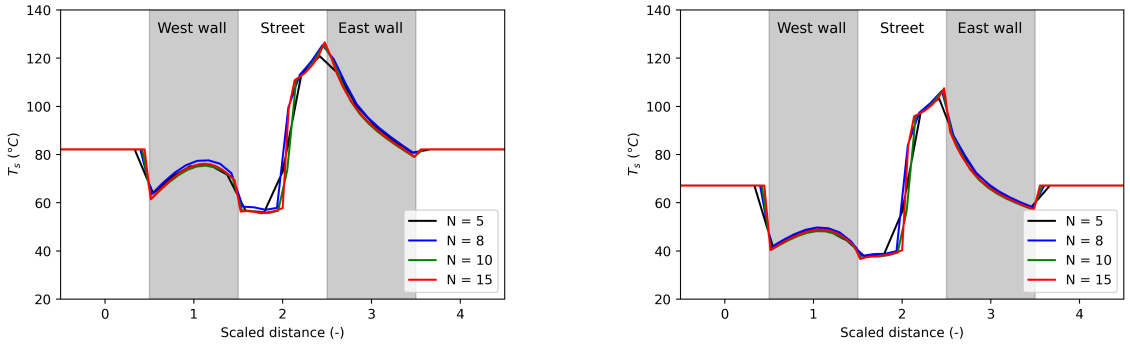

(a) Case 01. **(b)** Case 02.

Figure 5.13: Grid refinement study for $H/W = 1$. The plotting is done according to the inset shown in figure 5.9.

From the figures above it can be seen that for more than 8 slices, the surface temperature distribution converges. This can be seen most evidently from the point separating the shaded part from the sun-lit part of the canyon, which is around the middle of the street. Besides that, it can be seen that with a higher amount of slices, the peak surface temperature converges to the corner of the street canyon. This is in line with what is found by Schrijvers (2020). The relative error between the surface temperatures with more than 8 slices falls below 1 %, which is very little. Thus, the grid is sufficiently refined for $N \geq 8$.

Diurnal variation of the surface temperature

In this subsection, the diurnal variance of the surface temperature will be discussed. This is approximated by simulating different times during the day since the current study's model is inherently steady state. This diurnal variance will be discussed for $H/W = 1$. The solar values correspond to the 21st of June in Amsterdam with clear-sky conditions. The diurnal variation of the solar zenith angle is given in figure 5.14. In this figure, the dashed line indicates the time of solar noon, i.e., the time when the sun is at its highest. Because the street canyon is a 2D approximation, the solar azimuthal angle must coincide with the XZ-plane. Therefore, in the morning, the solar azimuthal angle is equal to $\pi/2$ and, in the afternoon, the solar azimuthal angle is equal to $3\pi/2$.

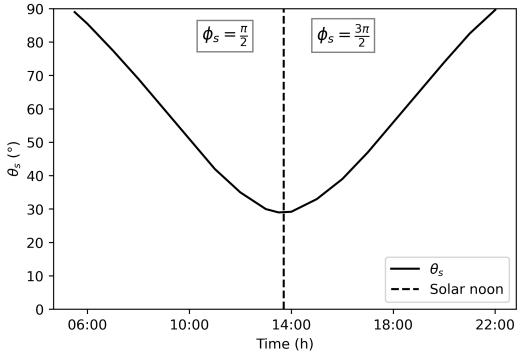

Figure 5.14: A graph showing the relation between the solar zenith angle, θ_s, and time on the 21st of June in Amsterdam. Besides that, the solar noon time is also given as a dashed line.

The surface temperature across the canyon for four different times during the day is given in figure 5.15. This includes case 01 (5.15a), case 02 (5.15b) and case 03 (5.15c). In these figures, the four different colors indicate four different times during the day: 06:00 (black), 12:00 (green), 14:00 (red), and 18:00 (blue).

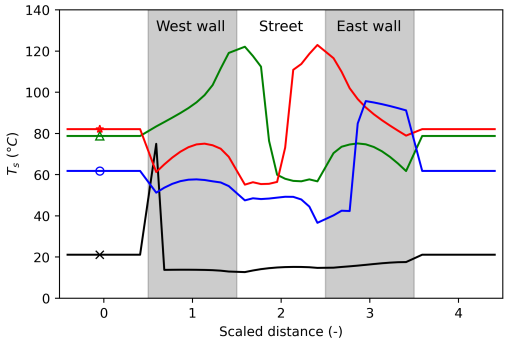

(a) Case 01.

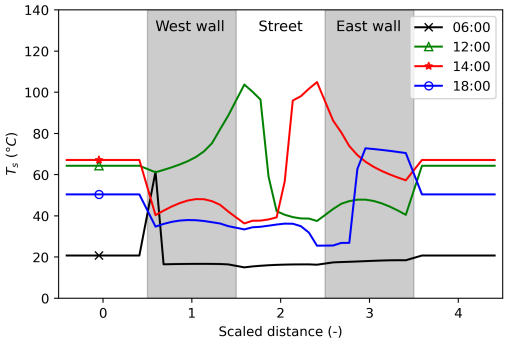

(b) Case 02.

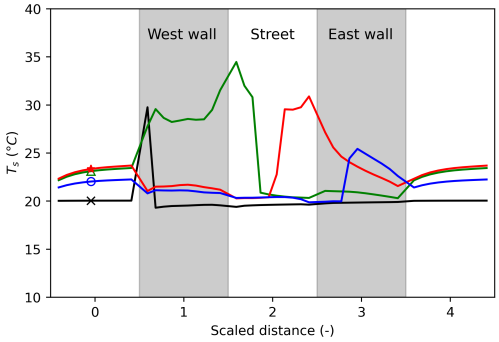

(c) Case 03.

Figure 5.15: Surface temperature of the 2D canyon for four different times during the day, shown in the legend of figure (b). The plotting is done according to the inset shown in figure 5.9. The three plots represent case 01 (a), case 02 (b), and case 03 (c). *Note: A different temperature scale is used for figure (c).*

The three different cases, shown above, show a similar pattern for the different times during the day. The most obvious difference between them is the magnitude of the surface temperatures; the shapes look similar. Besides that, for 06:00, a sharp peak can be seen on the top of the west wall. This is as expected since at this time the sun sits very low and is coming from the east. This results in an almost complete shading of the canyon surfaces, which is also seen back in the surface temperatures.

The diurnal variation of the mean surface temperature per surface is given in figure 5.16 for cases 01-03. The mean surface temperatures are given for the east- and west walls, roof, and street. Each color indicates a different surface of the canyon, which can be seen in the legend of the figure.

The diurnal variation of the mean surface temperatures in case 01 is in line with what is physically expected. For the average roof temperature, a cosine behavior is seen which follows the position of the sun directly. The average street temperature shows a semi-cosine behavior with temperatures a little lower than the roof temperatures. The heating of the street is mostly due to reflections of the walls and environmental longwave radiation since the street is mostly shaded during the day. Even though the street is not completely sun-lit at solar noon, the average temperature matches the roof temperature. This is due to the longwave trapping effect: other hot surfaces heat the street with their emitted longwave radiation. The east- and west walls show symmetric heating. This is as expected, since at solar noon the solar azimuthal angle flips from $\pi/2$ to $3\pi/2$.

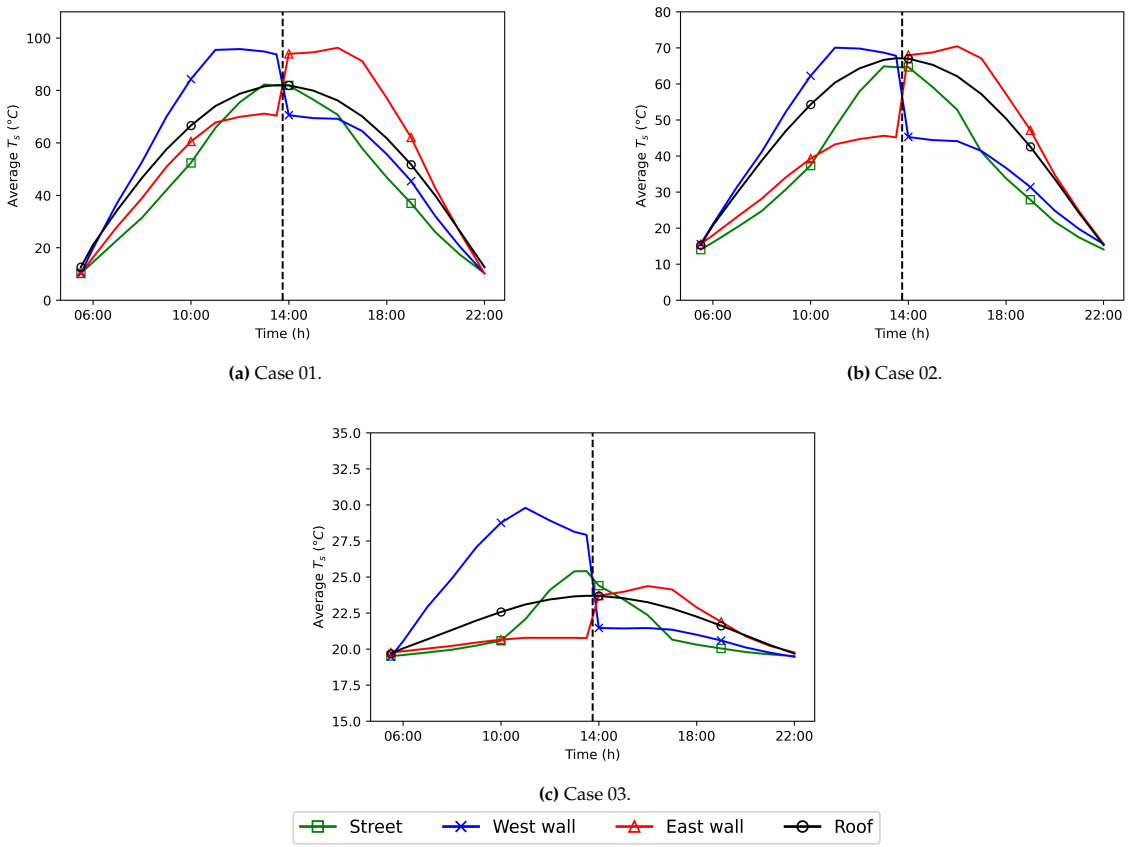

(a) Case 01.

(b) Case 02.

(c) Case 03.

Figure 5.16: Diurnal variation of the mean surface temperatures, T_s, for cases 01-03, given per part of the street canyon. Black indicates the average roof temperature, blue represents the west wall, red represents the red wall and green indicates the average street temperature. *Note: Different scales are used for the surface temperatures.*

The diurnal variation of the mean surface temperatures in case 02 is similar to that of case 01. The important distinction here lies in the difference between street temperature and roof temperature. Since the temperatures of all walls are cooled by conduction, less longwave radiation is emitted to the street. This explains the larger difference between roof temperature and street temperature in case 02 compared to that of case 01.

Besides the roof temperature, all surface temperatures of case 03 show asymmetric diurnal variation. When comparing the east- and west-wall temperatures, it can be seen that the west wall reaches significantly higher temperatures than the east wall. This is caused by a lower near-wall turbulent viscosity at the west wall and a higher near-wall turbulent viscosity at the east wall. Since the sensible heat flux is dominant in case 03, this explains the large difference between the two. The average street temperature also shows asymmetry, since the peak temperature does not coincide with solar noon. This is explained by the fact that the street temperature is highly influenced by the wall temperatures. As the sum of the east- and west-wall temperatures is higher before solar noon than it is after solar noon, the street temperature is also higher before solar noon than after solar noon.

Diurnal variation of the surface energy fluxes

The surface energy fluxes across the canyon for case 03 and $H/W = 1$ are given in figure 5.17 for four different times during the day. All colors indicate different energy fluxes, given in the legend below the figure. Note that negative values for the surface fluxes designate energy fluxes leaving the surface, whilst positive surface fluxes designate fluxes striking the surface.

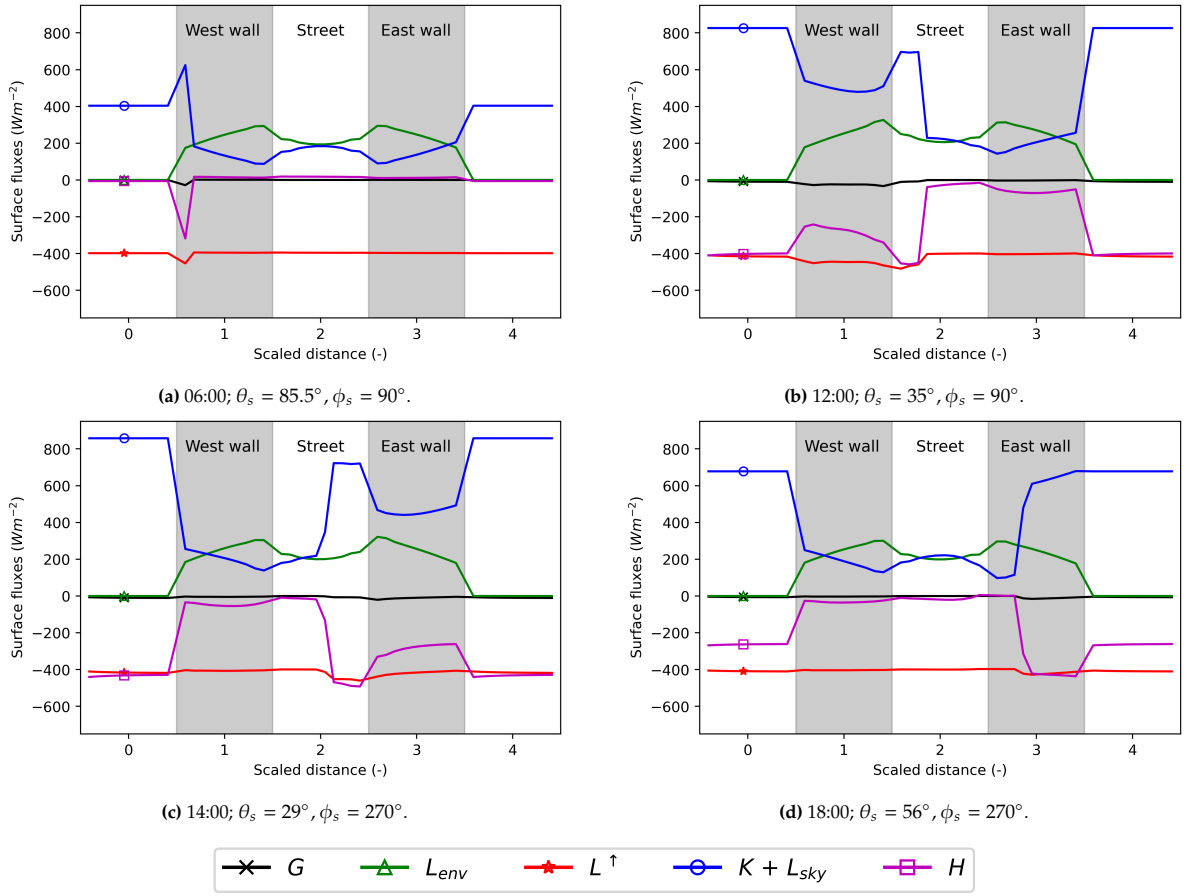

(a) 06:00; $\theta_s = 85.5°, \phi_s = 90°$.

(b) 12:00; $\theta_s = 35°, \phi_s = 90°$.

(c) 14:00; $\theta_s = 29°, \phi_s = 270°$.

(d) 18:00; $\theta_s = 56°, \phi_s = 270°$.

Figure 5.17: A figure showing the surface fluxes in the 2D street canyon for case 03 at different times during the day. The different colors indicate different surface fluxes, shown in the legend. The different times include 06:00 (a), 12:00 (b), 14:00 (c), and 18:00 (d).

The first thing to note is that the sum of all surface fluxes is equal to zero at all times. This is physically correct, since, at the surface, all energy fluxes must balance out according to the SEB. The second thing to note is that the conductive heat flux is almost negligibly small compared to the other energy fluxes. This shows that under the conditions of case 03, thermal radiation and convection are dominant over conduction. What can also be noted is that L_{env} and $L^{\uparrow}$ are very similar across all four times during the day and do not show a big variance. This can be explained by looking at figure 5.15c, where the surface temperature across the canyon is given for the four times for case 03. There, the largest temperature difference is approximately 14-15 K, which results in differences in $L^{\uparrow}$ of around 90 Wm^{-2}. Therefore, differences in $L^{\uparrow}$ seem very small in figure 5.17. This also results in little differences in L_{env}, since this is directly dependent on $L^{\uparrow}$.

The incoming radiation ($K + L_{\text{sky}}$) is independent from the surface temperature. This only depends on solar angles and intensities. The discussion on these fluxes is already done earlier in this section. The sensible heat flux is strongly dependent on the turbulent viscosity and surface temperature. As was seen in the diurnal variation of the mean surface temperatures, the turbulent viscosity is higher at the east wall than at the west wall. This explains the slightly larger sensible heat flux at the east wall at 12:00 compared to the sensible heat flux at the west wall at 14:00. Besides that, what stands out is that the sensible heat flux seems to follow the mirrored shape of the incoming radiation. This makes physical sense, since the main driver behind surface heating is the incoming radiation and the sensible heat flux is stronger for higher surface temperatures.

5.3. Case 3: Infinite parallel plates

The longwave radiation model and conduction model are also validated with a case where the analytical solution is known. This case consists of two infinite parallel walls during nighttime. In this case, longwave radiation and conduction are the only two physical mechanisms that are considered. In the next section, more details will be discussed concerning the simulation set-up and parameters.

5.3.1. Simulation set-up

The simulation set-up is presented in figure 5.18. The figure shows two infinite walls with each a wall temperature T, thickness d, emissivity ε, inner temperature T_∞, and longwave absorptivity ζ. With this in mind, the steady-state energy surface balance over wall 1 is given by the following equation:

$$-\lambda \frac{T_1 - T_{\infty,1}}{d_1} - \varepsilon_1 \sigma T_1^4 + \varepsilon_2 \zeta_1 \sigma T_2^4 = 0, \tag{5.1}$$

where σ is the Stefan-Boltzmann constant ($\sigma \approx 5.67 \times 10^{-8} W m^{-2} K^{-4}$). For wall 2 the surface energy balance is similar:

$$-\lambda \frac{T_2 - T_{\infty,2}}{d_2} - \varepsilon_2 \sigma T_2^4 + \varepsilon_1 \zeta_2 \sigma T_1^4 = 0. \tag{5.2}$$

These equations can be solved for T_1 and T_2 to acquire the analytical solution. This is tested with the simulated solution. Two tests are considered: One emissivity dependency test and one inner temperature difference test. The parameters used in this study (if not stated otherwise) are given in table 5.8.

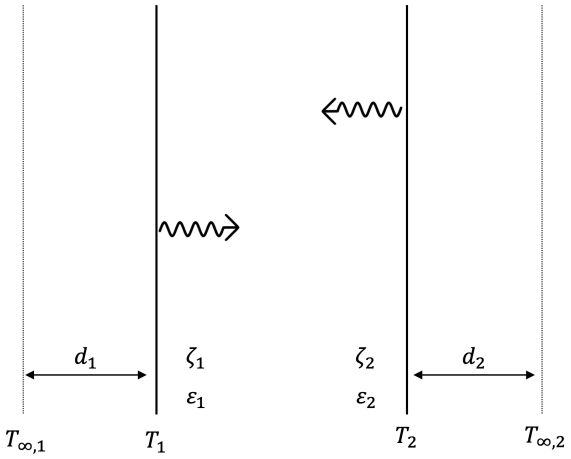

Figure 5.18: A schematic presentation of two infinite parallel walls with temperatures T_1 and T_2, emissivities ε_1 and ε_2, wall thicknesses d_1 and d_2, and internal temperatures $T_{\infty,1}$ and $T_{\infty,2}$.

Parameter	ε dependency	T difference dependency
Emmisivity, ε (-)	0-1	0.95
Absorptivity, ζ (-)	1	1
Wall thickness, d (m)	1	1
Inner wall temperature 1, $T_{\infty,1}$ (K)	293	293
Inner wall temperature 2, $T_{\infty,2}$ (K)	273	273-293

Table 5.8: Parameter values for the simulations done for the two tests in the infinite parallel wall case.

5.3.2. Results

The results for the two tests are given in figure 5.19. In figure 5.19a, the surface temperature is determined for a varying emissivity. In figure 5.19b, the surface temperature is calculated for a varying temperature difference between $T_{\infty,1}$ and $T_{\infty,2}$.

The results for both the emissivity dependency test and temperature difference dependency test have a very good correspondence with the analytically found values. A lower emissivity results in a lower radiant heat flux, which, as physically expected, results in the temperature drawn towards the inner wall temperature. Besides that, from figure 5.19b, it can be seen that a higher inner wall temperature difference results in lower surface temperature. This makes sense since a higher temperature difference results in stronger heat transportation from the warmer wall to the colder wall.

Overall, it can be said that the longwave radiation model and conduction model correctly describe the physical mechanisms. The results are in good agreement with the analytical solutions.

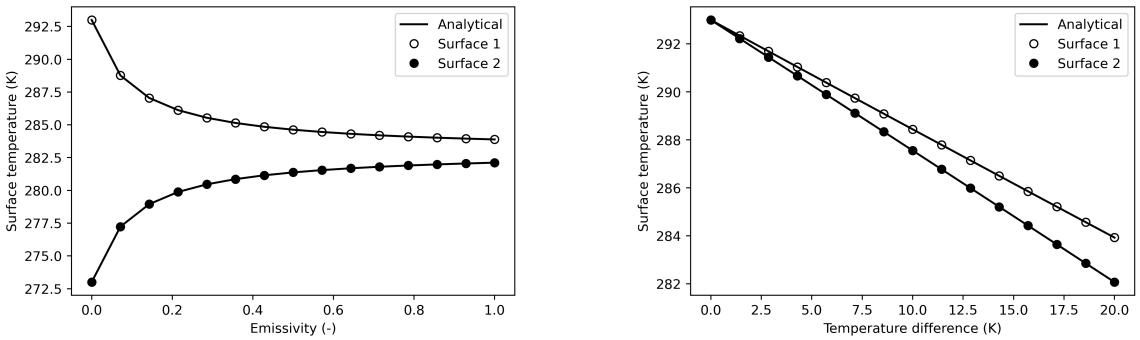

Figure 5.19: A comparison between the current model and the analytical solution for the infinite parallel wall case. Figure (a) shows the dependency of the surface temperature of the two different infinite walls on the emissivity, where $\varepsilon_1 = \varepsilon_2$. Figure (b) shows the surface temperature of each facet against the temperature difference between the two internal temperatures $T_{\infty,1}$ and $T_{\infty,2}$.

5.4. Case 4: 3D street canyon

The 3D street canyon case is done to showcase the capabilities of the current model and give insights into the distribution of the surface temperature and surface energy fluxes present in this kind of geometry. Besides that, the results are compared to the results found in the infinite street canyon case (section 5.2) such that there can be made a distinction between 2D- and 3D effects.

5.4.1. Simulation set-ups

The 3D street canyon consists of 4 buildings with height H and width W with an intersection area in between them. The simulations are done for three different H/W ratios: $H/W = 0.5$, $H/W = 1$ and $H/W = 2$. A schematic image of the simulation set-up of the SEB model is given in figure 5.20, where also the position of the sun is given. Here, the street canyon width is equal to the width of the buildings, W. The red highlighted area designates the street area which is later used in contour plotting. The geometric quantities for the three different simulation set-ups are given in table 5.9. In total, 2624 facets are used in this set-up. All relevant parameters for the SEB model are given in table 5.11. The solar intensities are based on Schrijvers (2020) and represent solar noon in Amsterdam on the 21st of June under clear-sky conditions. The conductive and radiative material properties correspond to typical values for brick and concrete and are taken constant over all surface areas.

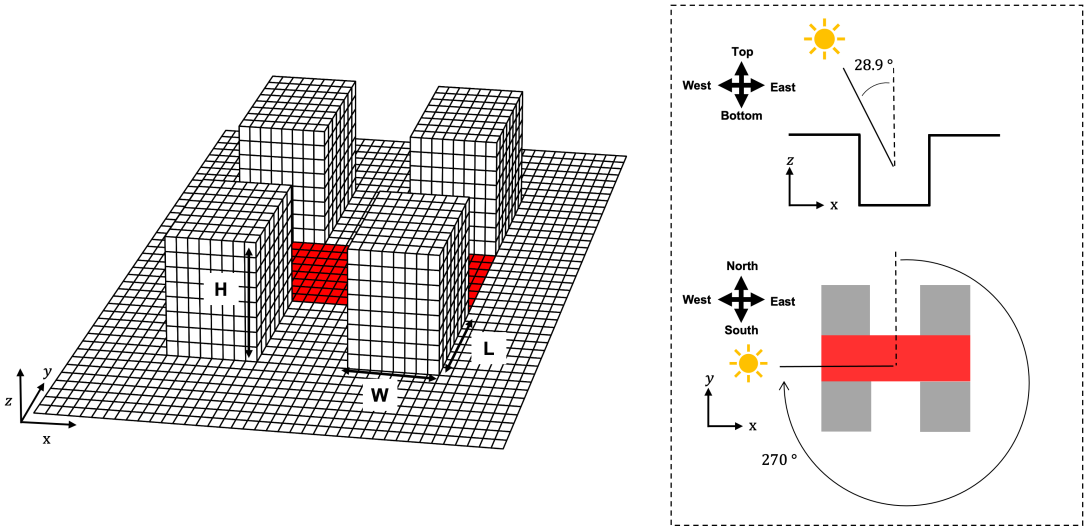

Figure 5.20: A schematic overview of the simulation domain used in the SEB model. Here, the street canyon width is equal to the building width, W. The red areas indicate the area used in the contour plots later in this section.

Parameter	$H/W = 0.5$	$H/W = 1$	$H/W = 2$
Canyon width, W (m)	50	25	25
Canyon length, L (m)	50	25	25
Canyon height, H (m)	25	25	50
Horizontal facet size $(l_x \times l_y)$	$(6.25m \times 6.25m)$	$(3.13m \times 3.13m)$	$(3.13m \times 3.13m)$
Vertical facet size $(l_x/l_y \times l_z)$	$(6.25m \times 3.13m)$	$(3.13m \times 3.13m)$	$(3.13m \times 6.25m)$

Table 5.9: Geometric values for the three different H/W ratios. Here, l_x represents the facet width in the x-direction, l_y represents the facet length in the y-direction and l_z represents the facet height in the z-direction.

To model the sensible heat flux, a CFD simulation is done. This simulation is done with the in-house CFD model. A pragmatic approach is used to couple the CFD model with the SEB model. Values of the turbulent viscosity are fed into the SEB model using a nearest neighbor algorithm. The algorithm determines for each facet the nearest CFD cell. The value of the turbulent viscosity of that CFD cell is then transposed onto the facet. The simulation set-up for the in-house CFD model is schematically

given in figure 5.21. Air with a constant and homogeneous velocity, U_{in}, is given as input to the domain. The temperature of the air is kept constant at 20 $°C$. An overview of the relevant parameters used for the CFD model is given in table 5.11.

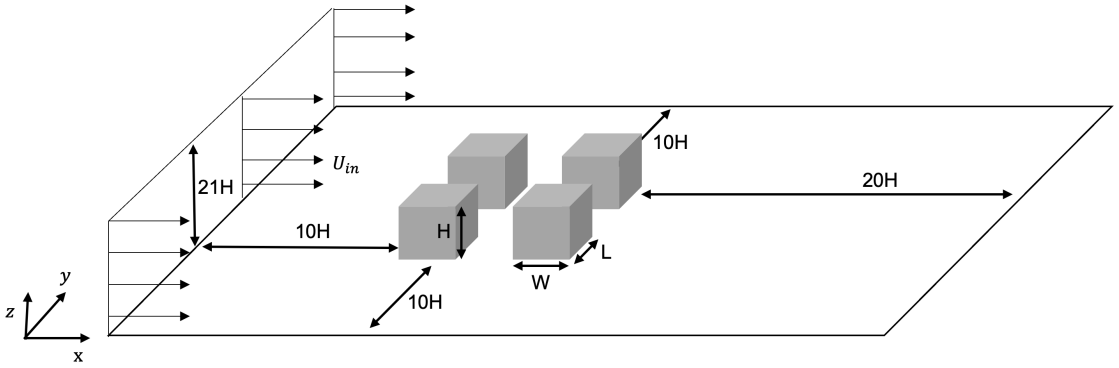

Figure 5.21: A schematic overview of the simulation set-up for the CFD model.

Different cases are considered in the computations of the surface temperatures. These cases are listed in table 5.10. This is done to differentiate the effect and contribution of the different surface energy fluxes to the surface temperature.

Case	K	L	G	H
01	+	+		
02	+	+	+	
03	+	+	+	+

Table 5.10: The three cases which are considered in this study. Case 01 represents the case in radiative equilibrium, case 02 is the case where the conductive heat flux is added, and case 03 is the case where the sensible heat flux is also added to the equation.

	Radiation
Diffusive sky radiation, D_{sky}	84.2 Wm^{-2}
Longwave absorptivity, ζ	0.95
Longwave emissivity, ε	0.95
Longwave sky radiation, L_{sky}	325 Wm^{-2}
Shortwave albedo factor, α	0.40
Solar azimuthal angle, ϕ_s	270 °
Solar irradiance, I	950 Wm^{-2}
Solar zenith angle, θ_s	28.9 °
	Heat conduction
Interior temperature, T_∞	20 $°C$
Thermal conductivity, λ	0.72 $Wm^{-1}K^{-1}$
Thickness building, d	0.25 m
Thickness street, d	1 m
	Computational Fluid Dynamics
Air temperature, T_a	20 $°C$
Cell expansion factor	1.1
Inlet velocity, U_{in}	4 ms^{-1}
Minimal cell size	$(x \times y \times z) = (1m \times 1m \times 1m)$
Maximum cell size	$(x \times y \times z) = (25m \times 25m \times 25m)$

Table 5.11: All parameter values used in this case study, which are based on Schrijvers (2020).

5.4.2. Results

In this section, the results will be discussed of the 3D street canyon case. First, contours of the street temperature will be given for case 01 and case 03. Secondly, surface temperature profiles will be discussed and compared to results found in the infinite street canyon case. After that, near-surface turbulent viscosity contours will be presented. Then, the contours of all surface energy fluxes present in case 03 will be discussed and the diurnal variation of the street temperatures. Lastly, a grid refinement study and the effect of air velocity on the surface temperatures will be discussed.

Street temperature contours

In this subsection, the street temperature contours will be evaluated. The area of interest is highlighted in red in figure 5.20. The street temperatures will be considered for cases 01 and 03. The contours of case 02 are left out in this section but can be found in appendix D.3. The contours for case 01 are given in figure 5.22 and the contours for case 03 are given in figure 5.23. In these figures, the horizontal- and vertical axes designate the normalized $x-$ and $y-$directions. Note that all plots in figure 5.22 have different color bar ranges. The vertical dashed lines indicate where the area of the intersection resides.

The first thing that stands out is that all street temperature contour plots are symmetric along the $y/L = 0.5$ line. This is in line with what was physically expected since the geometry and all other parameter values are symmetric along this line. Therefore, this is a confirmation of the fidelity of the SEB model.

For case 01, the shape of the contour plots is different for each H/W ratio, especially at the intersection area. For all three aspect ratios, the west side of the street is warmer than the east side. This difference is most significant for $H/W = 2$. For $H/W = 2$, the sun-lit surface area of the two eastern buildings is larger than for the other two aspect ratios. This results in a larger L_{env} striking the west street area compared to $H/W = 1$ and $H/W = 0.5$.
Besides the uneven heating of the street area, another thing that stands out is the great difference in temperatures between the different H/W ratios. The larger the H/W ratio, the larger the temperature. This is the result of the longwave trapping effect, where the longwave radiation gets trapped inside the street canyon. This also explains the lower temperatures at the intersection area. Here, radiation can leave the street canyon easier, since the sky view factor is greater in this area compared to the west- and east-street areas. The difference in temperatures shows that the SEB model correctly describes and models the longwave trapping effect.

For case 03, the shape of the contours are very similar for different H/W ratios. Besides that, the values of the street temperatures are somewhat alike. At the upstream part of the street (west street area), the temperatures are around 24 $^\circ C$ and at the downstream part of the street (east street area), the temperatures increase to approximately 28 $^\circ C$. The fact that the contour shape and temperatures are alike shows that the sensible heat flux is dominant under these conditions. The contour shape found in case 01 is completely turned around in case 03.

Besides the difference in contour shapes between case 01 and case 03, the values for the street temperatures also differ significantly. Case 01 shows temperatures between 87-105 $^\circ C$. Note that these temperatures are hypothetical temperatures, which follow directly from the balance between longwave- and shortwave radiation fluxes. The surface temperatures are, however, in line with Garratt (1992) as stated by Schrijvers (2020). Garratt suggested that for dry and dark soils with low thermal conductivity surface temperatures may occur of around 90-100 $^\circ C$, considering a simplified form of the SEB. Besides that, the ranges of street temperatures found in this study also correspond to values found by Schrijvers (2020).

The temperature ranges for case 02 are about 15-20 $^\circ C$ lower compared to case 01 (see appendix D.3). Here, the conductive heat flux merely serves as a simple cooling mechanism and the shape of the contours remains similar to those in case 01. When the sensible heat flux is added (case 03) the surface temperatures drop by approximately 60 $^\circ C$ compared to case 02. This is a significant decrease and shows, again, that the sensible heat flux is the most dominant cooling mechanism under these conditions. This can also be seen from the similarity between the contour shapes of the temperature and the turbulent viscosity contours (figure 5.27), which will be discussed later on.

Although the contour shapes and temperature ranges do seem convincing, there are some aspects to take note of. The conduction modeling in the SEB model, for example, is highly simplified. First of all, the current model assumes conduction to be linear. This is not always the case, especially when dealing with different materials inside the conductive layer. Second, a set interior temperature at a distance d inside the material is used as a boundary condition for the conductive heat flux. This leads to an artificial heat source or sink inside the material. A more realistic approach is to use a zero-flux boundary condition (Grylls et al. (2021); Suter (2019); Schrijvers (2020)). Although this makes computations more complex, it does make the model more realistic.

Another important thing to consider is the simplified modeling of the sensible heat flux. To model the sensible heat flux, the turbulent viscosity values are transposed onto the facet via the nearest neighbor algorithm. This may lead to inaccuracies when the facet sizes are significantly smaller or greater than the CFD cell sizes. Besides that, the Simple Gradient Diffusion Hypothesis (SGDH) is used to model the sensible heat flux. Other methods, such as the Generalized Gradient Diffusion Hypothesis (GGDH) could lead to more accurate results. Chao (2010) showed that, for mean concentrations, GGDH is preferred over SGDH. If the same holds for temperatures, it could lead to better results for this study as well.

The third point of discussion is the one-way coupling approach between the CFD- and SEB models. This approach assumes that the surrounding air is kept at a constant temperature and is not affected by the warmer surfaces. The pitfall of one-way coupling is the over-cooling of the surfaces; the colder surrounding air acts as a very efficient heat sink. Besides that, in modeling the sensible heat flux, the temperature gradient between the air- and surface temperature is linearized. The linearization may lead to inaccuracies since a distance must be specified over which the gradient is taken. In this study, this is set to 0.5 m, such that it matches the results of Schrijvers in the infinite street canyon case. This value, however, heavily influences the strength and magnitude of the sensible heat flux. Therefore, it is more realistic to use a two-way coupled approach.

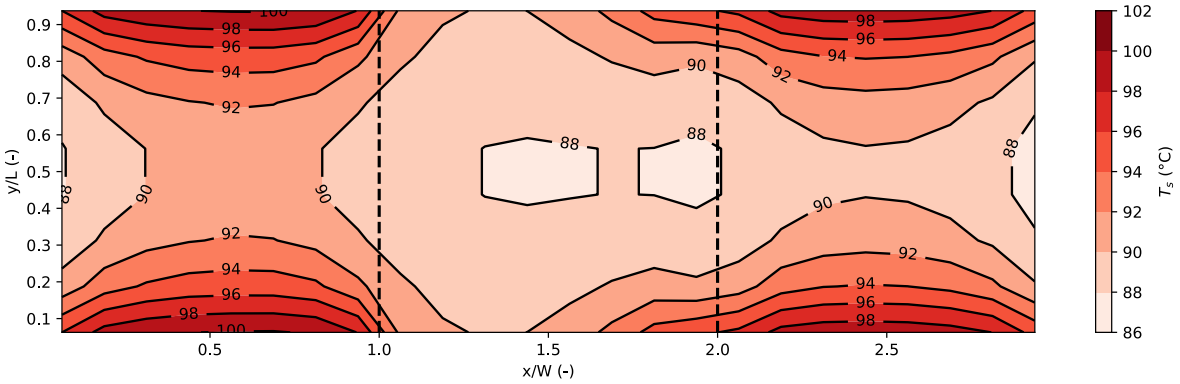

(a) $H/W = 0.5$.

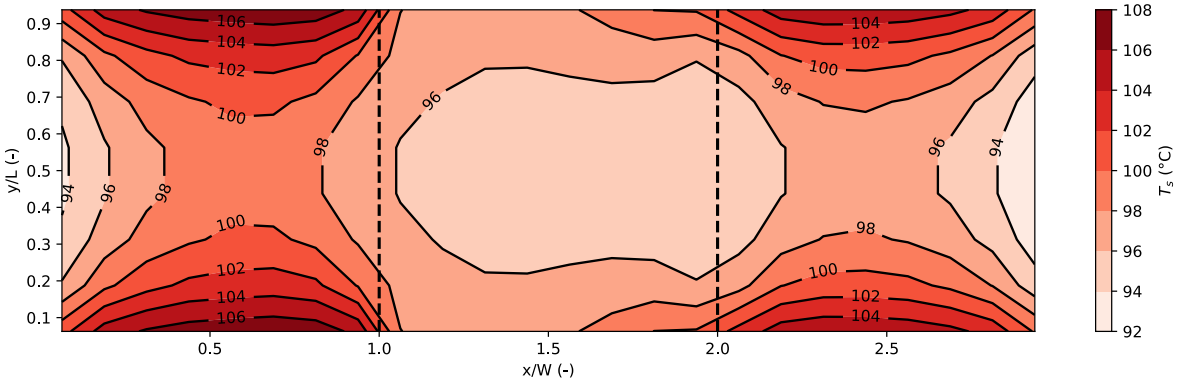

(b) $H/W = 1$.

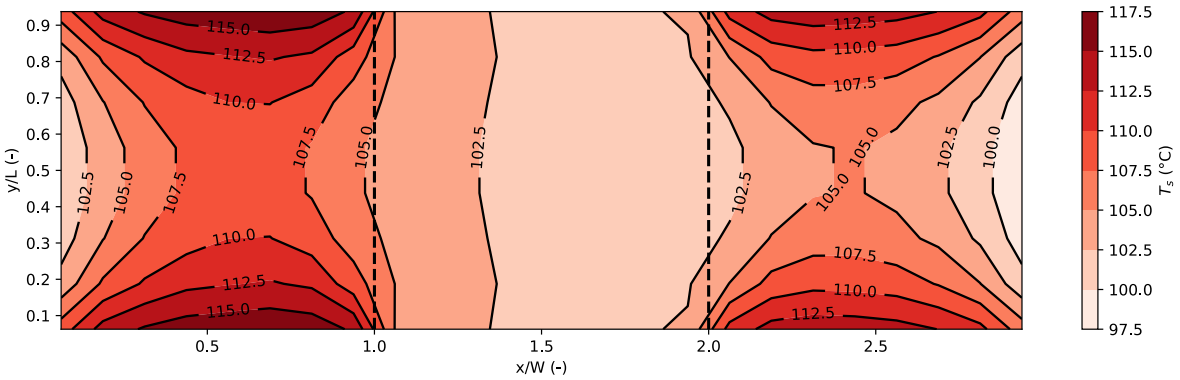

(c) $H/W = 2$.

Figure 5.22: Contours of the street temperatures for case 01 at the street area highlighted in figure 5.20. The vertical dashed lines separate the intersection area from the rest of the street area. *Note: The color bar ranges differ per plot.*

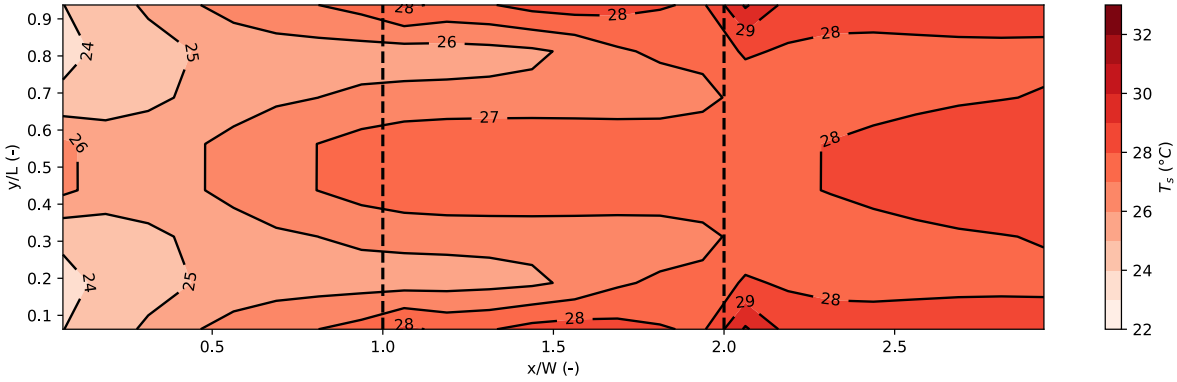

(a) $H/W = 0.5$.

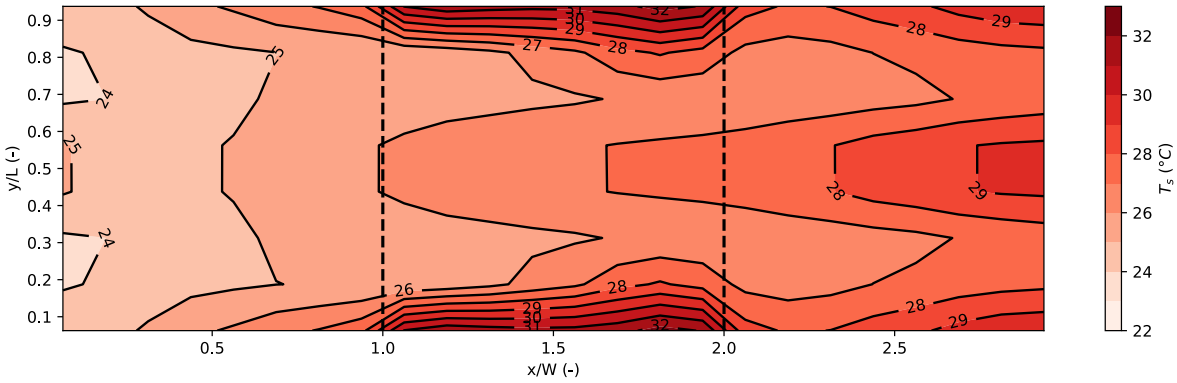

(b) $H/W = 1$.

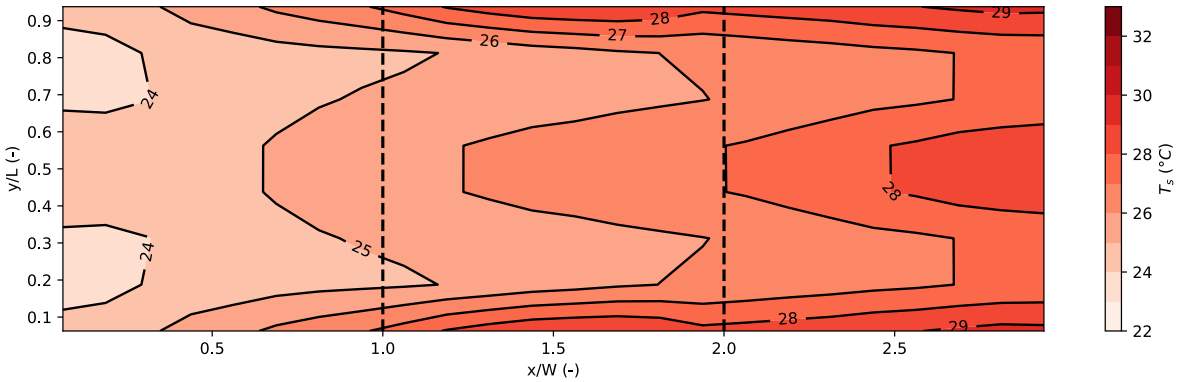

(c) $H/W = 2$.

Figure 5.23: Contours of the street temperatures for case 03 at the street area highlighted in figure 5.20. The vertical dashed lines separate the intersection area from the rest of the street area.

Surface temperature profiles

In this subsection, six different surface temperature profiles will be presented and discussed. The locations of these profiles are schematically depicted in figure 5.24. The profiles are numbered according to the left-hand side of the figure. This numbering is later used in plotting. Profiles 1-3 are compared to 2D profiles, which were found in the infinite street canyon case, to showcase the difference between a 2D street canyon and a 3D street canyon.

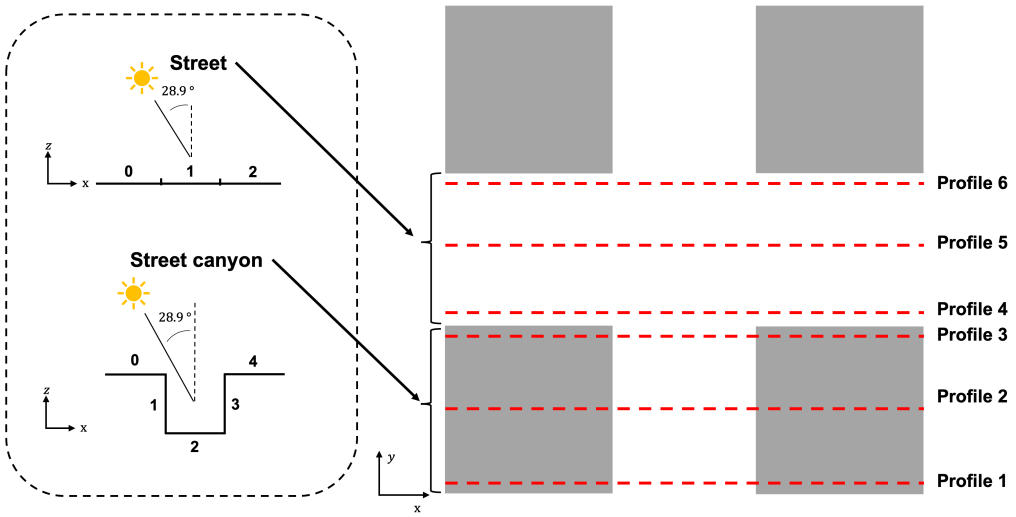

Figure 5.24: A schematic overview of the profiles that are presented in this subsection. On the right, a top view of the geometry is shown where buildings are shown in grey. The numbering on the left-hand side is used for plotting purposes later on in this subsection.

Temperature profiles 1, 2, and 3 are given for $H/W = 2$ and case 01 and 03 in figure 5.25. In these figures, the colors indicate the different profiles, as can be seen from the legend at the bottom. The dashed line represents temperature profiles found in the infinite street canyon case. Plotting is done according to the numbered inset shown at the bottom left in figure 5.24. The results for the other H/W ratios can be found in appendix D.1.

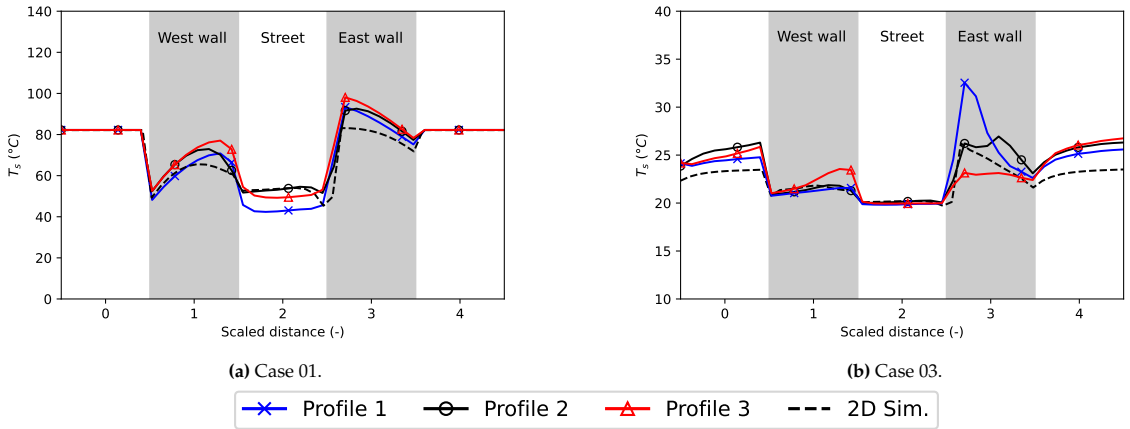

(a) Case 01. **(b)** Case 03.

Figure 5.25: Street canyon temperature profiles for $H/W = 2$ and cases 01 and 03. The plotting is done according to the schematic on the bottom left of figure 5.24. Note that some markers are left out for imaging purposes.

For cases 01 and 03, the temperature profiles 1-3 deviate slightly from the 2D simulated profile. Profile 2 is the closest to the 2D profile for both cases 01 and 03. This makes sense since profile 2 represents the temperature profile in the middle of the street canyon and is therefore closest to an infinite street canyon approximation. Profile 1 has a street temperature of around 10 °C lower than the 2D simulation due to fewer surrounding buildings that irradiate this part of the street canyon. Profile 3 is, therefore, closer to the 2D simulation, since there is more irradiance by other surfaces on that part of the street canyon.

Profile 1 in figure 5.25b shows a high peak at the bottom of the east wall compared to profiles 2 and 3. This is caused by a smaller turbulent viscosity near the bottom of the southern part of the east wall compared to that of the northern part of the east wall. Here, clearly, 3D turbulent effects are displayed; the turbulent viscosity depends on x, y, and z, whereas for the infinite canyon case, it only depends on x and z. Besides that, it must be noted that in the infinite street canyon case, an array of buildings was used. In the 3D canyon case, merely one set of 4 buildings was used. With this difference in mind, the temperature profiles in figure 5.25b look remarkably similar.

Street temperature profiles 4-6 are given for $H/W = 2$ and cases 01 and 03 in figure 5.26. Plotting is done according to the numbered inset shown at the top left in figure 5.24. Again, the results for the other H/W ratios can be found in appendix D.1.

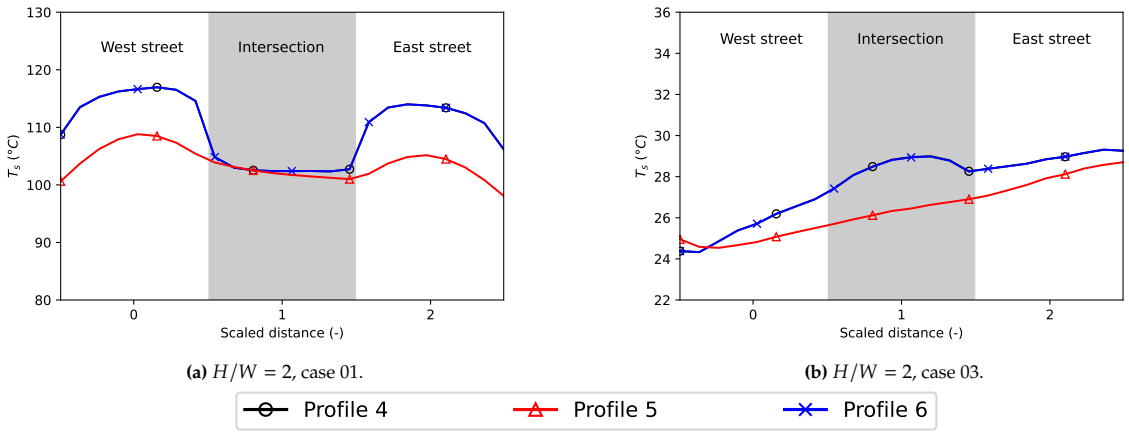

(a) $H/W = 2$, case 01.

(b) $H/W = 2$, case 03.

Figure 5.26: Street temperature profiles for $H/W = 2$ and cases 01 (a) and 03 (b). The plotting is done according to the schematic on the top left of figure 5.24. Note that some markers are left out for imaging purposes.

Profiles 4 and 6 overlap perfectly for both case 01 and case 03. This showcases again the line symmetry present in this configuration. In case 01, all profiles show a higher west street temperature compared to the east street temperature. As was seen in the temperature contours (figure 5.22), this is physically correct, since L_{env} is larger at the western part of the street than at the eastern part of the street. The intersection shows a lower temperature for all profiles in case 01. Profile 5 shows lower street temperatures since it is further away from the building walls and therefore receives less longwave radiation from other surfaces.

In the street temperature profiles of case 03 (figure 5.26b), the temperatures are higher at the east street compared to the temperatures at the west street. This is the opposite of what is seen in case 01. The lower street temperatures at the west street are a result of higher convective cooling at the west street compared to the east street. This is due to a higher turbulent viscosity at the west street compared to the east street, which can be seen from the turbulent viscosity contours in figure 5.27.
When case 01 is compared to case 03, it can be concluded that the convective cooling mechanism is very dominant. The sensible heat flux cools down the surface temperatures to moderate temperatures of 20-35 °C. Besides that, the street temperatures in case 03 follow a different pattern compared to the temperatures in case 01. This is also due to the higher sensible heat flux at the west street compared to the east street.

Turbulent viscosity contours

The (non-dimensional) turbulent viscosity contours are presented in figure 5.27. Here, the turbulent viscosity refers to the near-surface turbulent viscosity. The turbulent viscosity was extracted from the CFD simulations using the nearest neighbor algorithm. For each facet, the turbulent viscosity of the nearest CFD cell was selected.

The turbulent viscosity contours of the different aspect ratios all have a similar shape. At the western part of the street (upstream), ν^* is higher than at the eastern part of the street (downstream). The non-dimensional turbulent viscosity for $H/W = 2$ shows slightly higher values compared to the other two aspect ratios. It can be seen that there are lower values for ν^* at the top and bottom of the intersection area of the $H/W = 1$ case. This is caused by a lower turbulent kinetic energy in that region and this explains the higher surface temperatures in those areas for the $H/W = 1$ case (figure 5.23b).

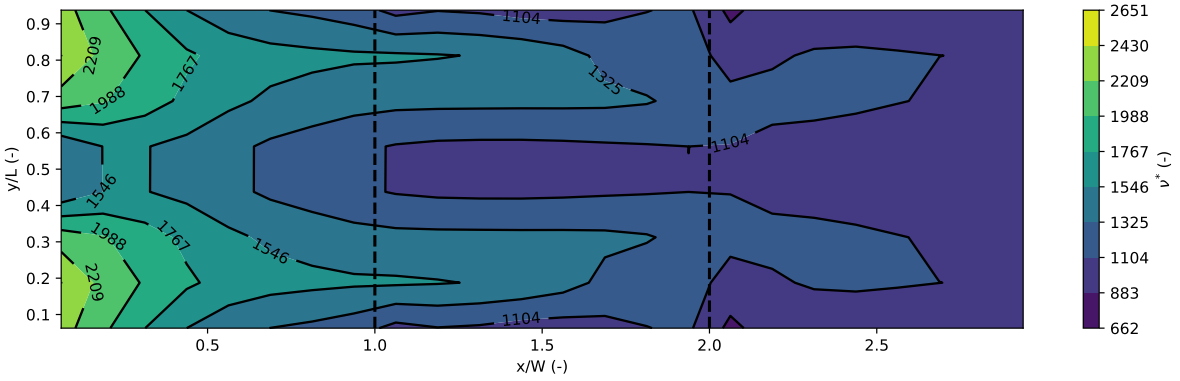

(a) $H/W = 0.5$.

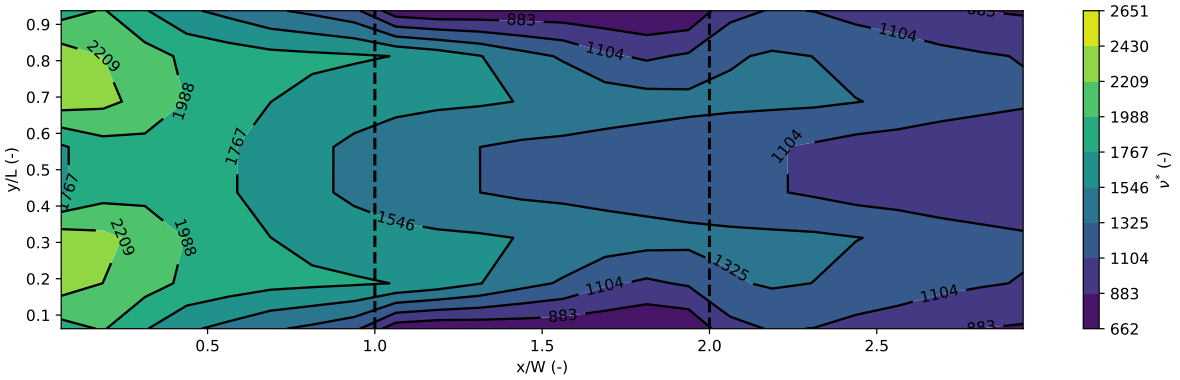

(b) $H/W = 1$.

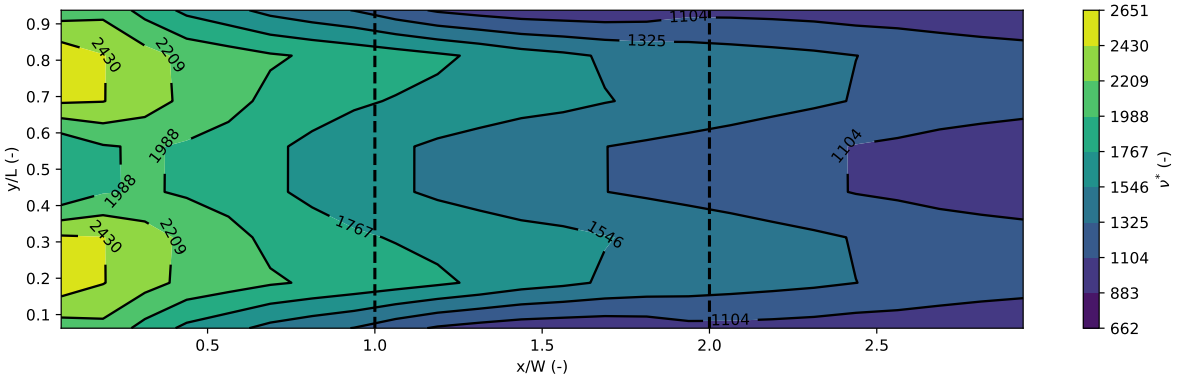

(c) $H/W = 2$.

Figure 5.27: Contours of the non-dimensional turbulent viscosity at the street area highlighted in figure 5.20, where $\nu^* = (\nu_t - \nu)/\nu$. The vertical dashed lines separate the intersection area from the rest of the street area.

Surface energy flux contours

Here, a study is presented of the contribution of different surface energy fluxes to the surface temperatures. Contours of the surface energy fluxes for case 03 and $H/W = 1$ are shown in figure 5.28. Note that H, $L^{\uparrow}$ and G are energy fluxes leaving the surface and L_{env} and $K + L_{\text{sky}}$ are energy fluxes striking the surface. It can be seen that all surface fluxes balance out, which is necessary in a steady-state simulation. The surface energy flux contours show the subservience of the conductive heat flux to the other heat fluxes. The conductive heat flux is in this case more than 10 times smaller than the sensible heat flux and the other radiative fluxes, which makes it almost negligible. It can therefore, again, be concluded that the sensible heat flux is the most dominant cooling mechanism in this case.
What can also be noted is the large difference in L_{env} across the street. This explains the higher surface temperatures near the building walls and the cooler temperatures at the intersection area, seen in figure 5.22. Therefore, figure 5.28b demonstrates the longwave trapping effect.

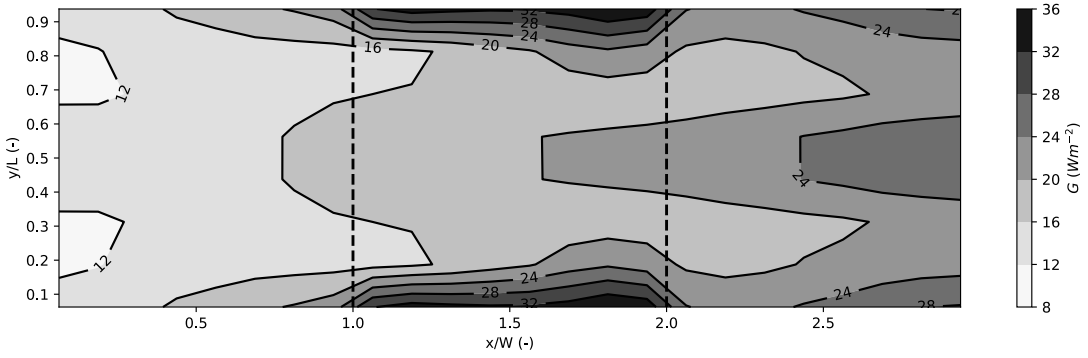

(a) G.

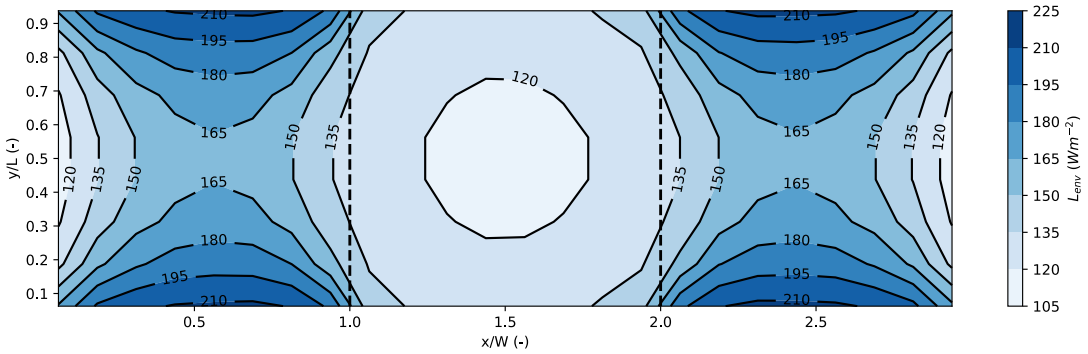

(b) L_{env}.

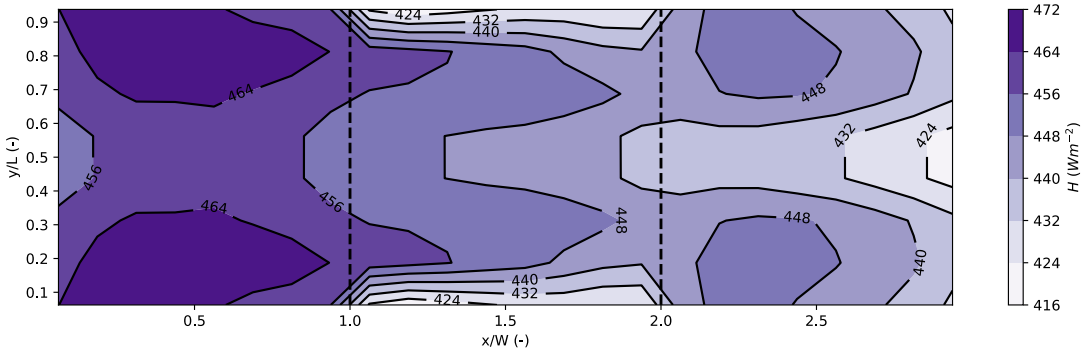

(c) H.

Figure 5.28: Contours of the surface energy fluxes for case 03 and $H/W = 1$ at the street area highlighted in figure 5.20. The vertical dashed lines separate the intersection area from the rest of the street area. Note that H, $L^{\uparrow}$ and G are energy fluxes leaving the surface and L_{env} and $K + L_{\text{sky}}$ are energy fluxes striking the surface.

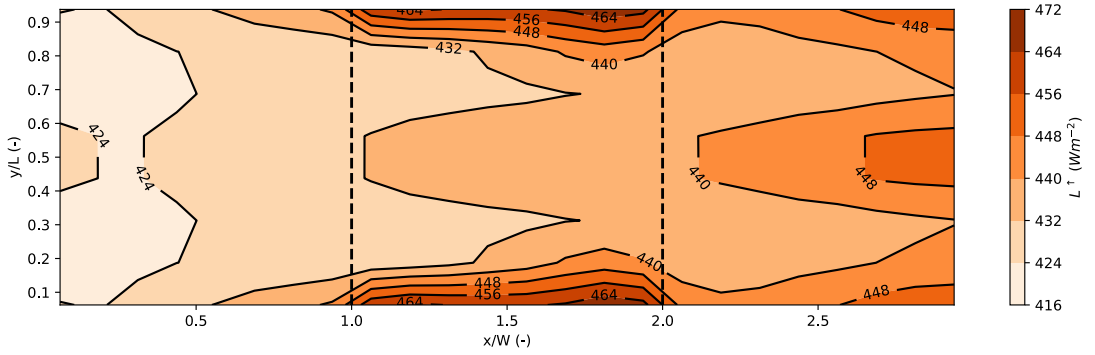

(d) $L^{\uparrow}$.

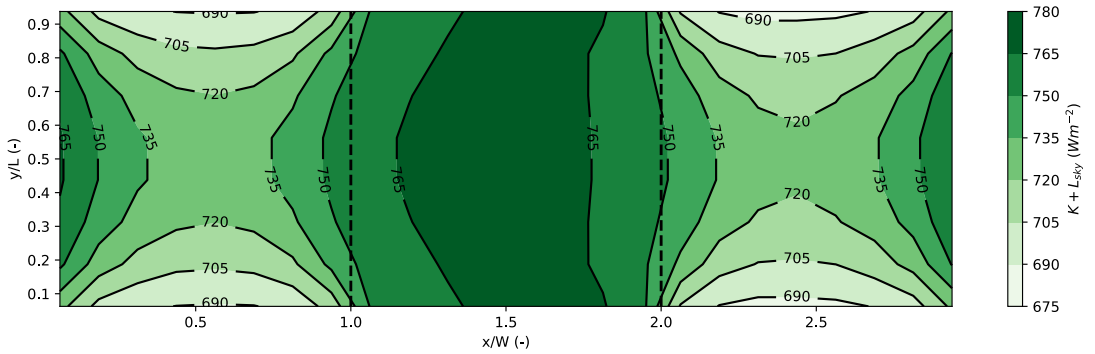

(e) $K + L_{\text{sky}}$.

Figure 5.28: Contours of the surface energy fluxes for case 03 and $H/W = 1$ at the street area highlighted in figure 5.20. The vertical dashed lines separate the intersection area from the rest of the street area. Note that H, $L^{\uparrow}$ and G are energy fluxes leaving the surface and L_{env} and $K + L_{\text{sky}}$ are energy fluxes striking the surface.

Diurnal surface temperature variation

Contours of the diurnal variation of the street temperature at four different times during the day are shown in figure 5.29. This includes 06:00 (a), 12:00 (b), 15:00 (c) and 21:00 (d). Again, the solar positions conform to the 21st of June in Amsterdam. The figures resemble the street temperature at the red highlighted area in figure 5.20. Besides that, 3D plots of the full simulated domain are given in appendix D.3 for the same point of time. All parameters except the solar angles are kept constant over the different points of time.

It is clear that shadowing has a great influence on the surface temperature. In figure 5.29a and 5.29d, a large part of the street is shaded due to a high solar zenith angle (i.e., a low solar elevation angle). In figure 5.29b and 5.29c, a smaller part of the street is shaded due to a low solar zenith angle. The effect of shading is evident: effectively all shaded parts have temperatures between 18-20 $°C$. The non-shaded parts of the street reach significantly higher temperatures of 24-34 $°C$.

In an experimental study done in Indonesia, Ibrahim et al. (2018) found that concrete pavements may reach temperatures varying between 25-38 $°C$ during the day. In another experimental study done at the University of California, Berkeley, Guan (2011) measured average brick pavers temperatures of around 37.3 $°C$ at solar noon. Although these experiments were done in different conditions compared to the current model, it can be said that the street temperatures found in this study give realistic values. The shaded street surface temperatures, however, are slightly lower than what was found in literature. This may be caused by the difference in air temperature at the measurement site and in the simulation. The study by Ibrahim et al. (2018) was done in Indonesia where maximum air temperatures were measured at 32.5 $°C$, which is significantly higher than the air temperature of 20 $°C$ used in this study. Therefore, this could have led to the difference in surface temperatures. Besides that, it was reported that the experiments were done under low wind speed conditions. Although exact values are not given, this could also lead to a deviation from the literature results.

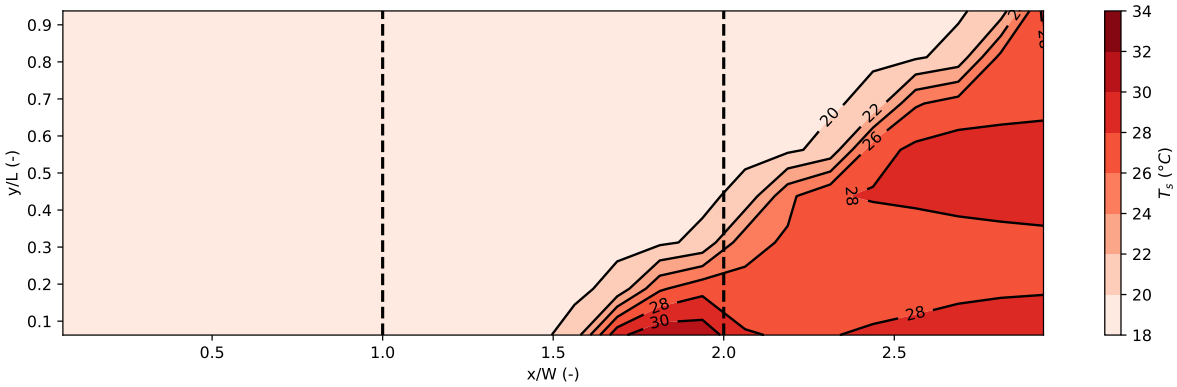

(a) 06:00; $\theta_s = 86°, \phi_s = 56°$.

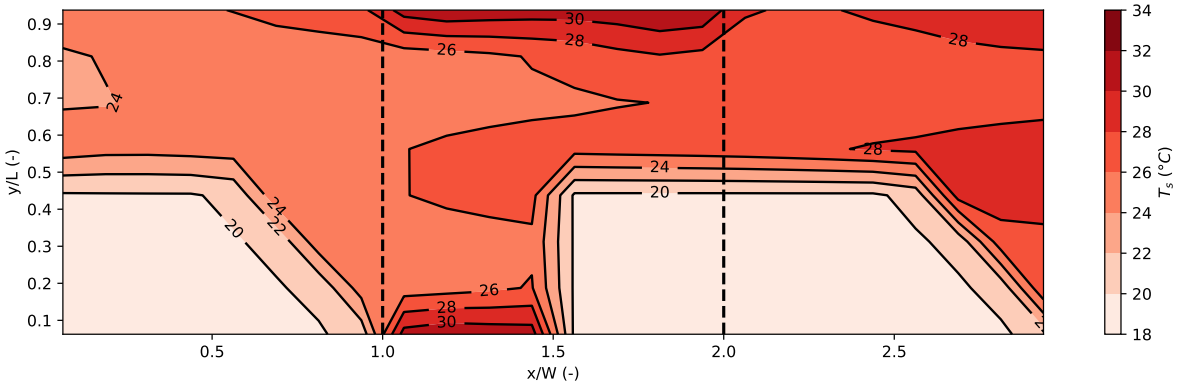

(b) 12:00; $\theta_s = 35°, \phi_s = 136°$.

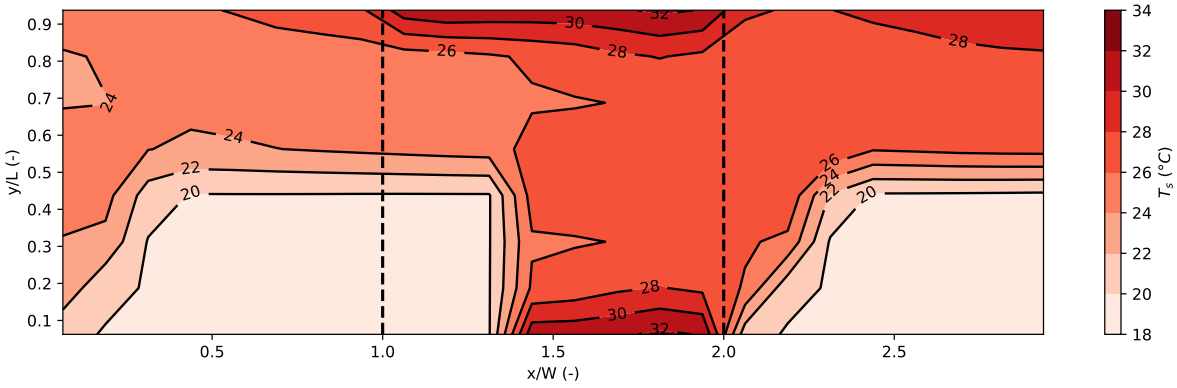

(c) 15:00; $\theta_s = 33°, \phi_s = 215°$.

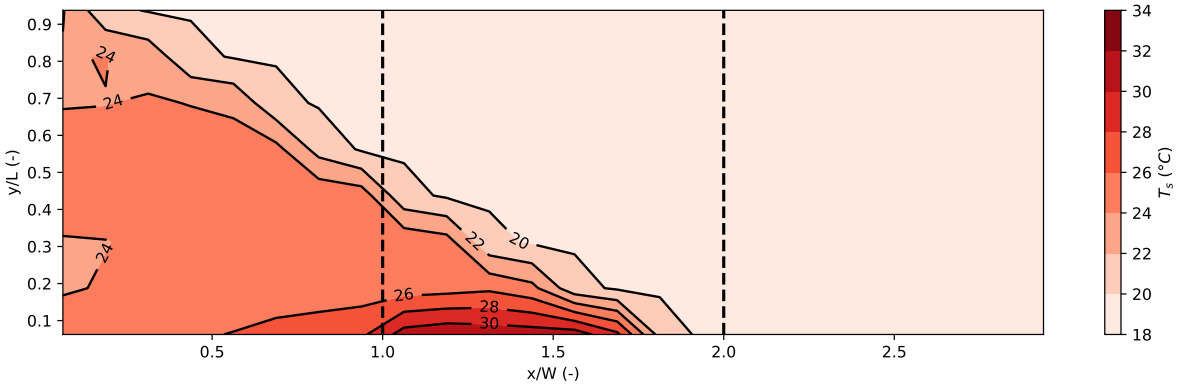

(d) 21:00; $\theta_s = 83°, \phi_s = 299°$.

Figure 5.29: Contours of the street temperature at different times during the day for $H/W = 1$ and case 03 at the area highlighted red in figure 5.20. The vertical dashed lines separate the intersection area from the rest of the street area.

Effect of grid refinement

The effect of grid refinement of the SEB model is discussed in this section. The results are given in figure 5.30, where four different facet sizes are used to plot the surface temperature in case 03. Here, $H/W = 1$, the solar azimuthal angle, ϕ_s, is equal to 136 ° and solar zenith angle, θ_s, is 35°. These solar angles conform to 12:00 in Amsterdam on the 21st of June. From the figures, it may be concluded that from $N = 8$, i.e., a facet size of 3.13 $m \times 3.13$ m, the surface temperature contour is sufficiently converged. Therefore, this facet size is also used in this study.

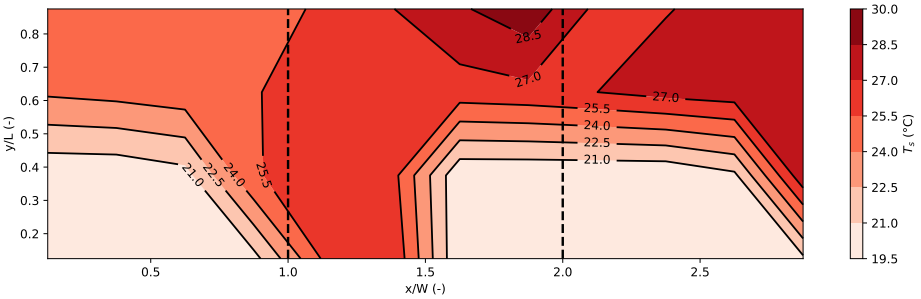

(a) $N = 4$; facet size $6.25m \times 6.25m$.

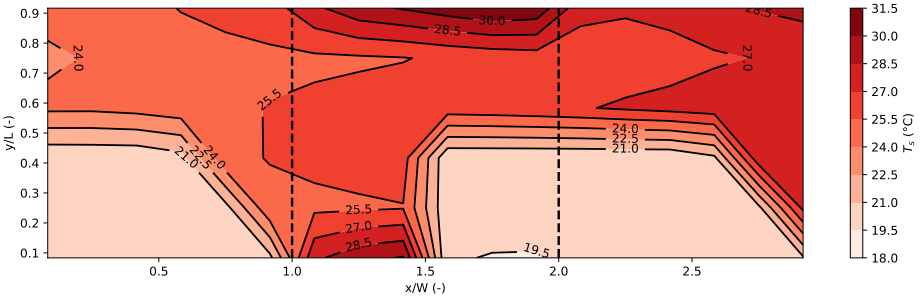

(b) $N = 6$; facet size $4.17m \times 4.17m$.

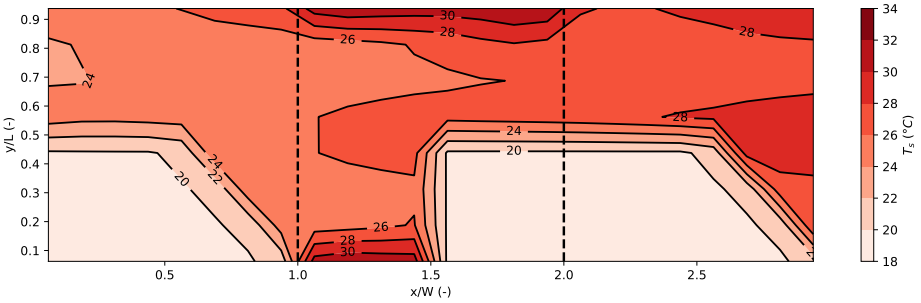

(c) $N = 8$; facet size $3.13m \times 3.13m$.

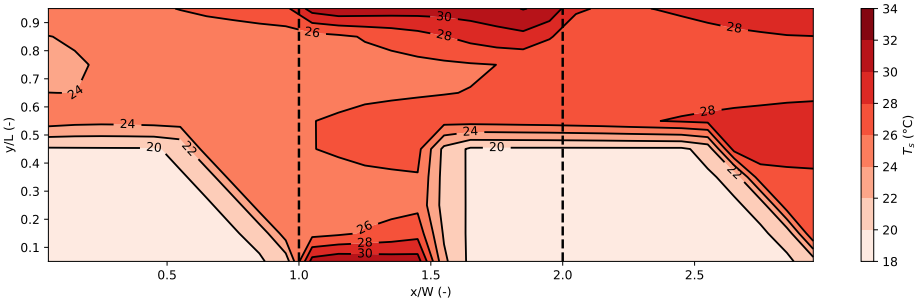

(d) $N = 10$; facet size $2.5m \times 2.5m$.

Figure 5.30: Four surface temperatures with different grid sizes for case 03 of the street area highlighted in figure 5.20. Here, $H/W = 1$, $\phi_s = 136°$ and $\theta_s = 35°$. The vertical dashed lines separate the intersection area from the rest of the street area.

Effect of air velocity

In this section, the effect of air velocity on surface temperatures is discussed. This has been done by comparing three different inlet velocities, U_{in}: 1 m/s, 2 m/s, and 4 m/s. The results are given in figure 5.31. It is clear that for higher inlet velocities, the surface temperatures are lower. This makes physical sense since less heat can be transported away from the surface with lower velocities of the surrounding medium. Therefore, this parametric study strengthens the fidelity of the current model.

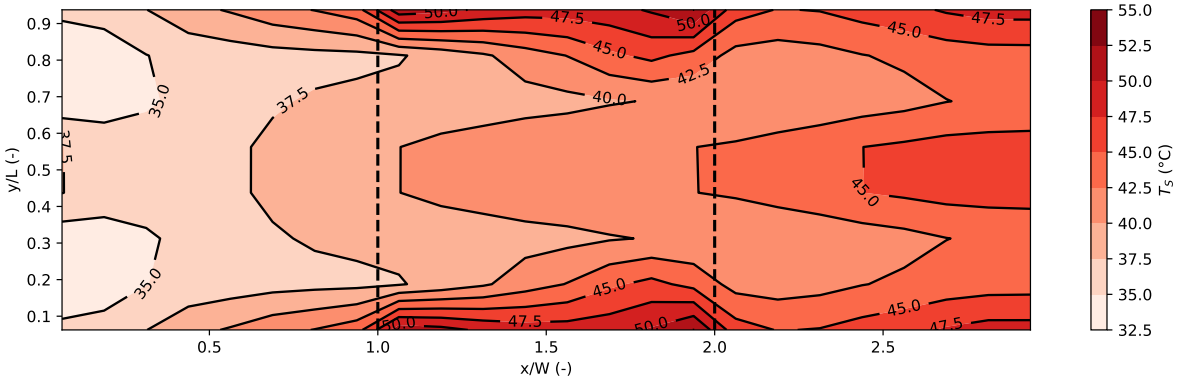

(a) $U_{in} = 1\ m/s$.

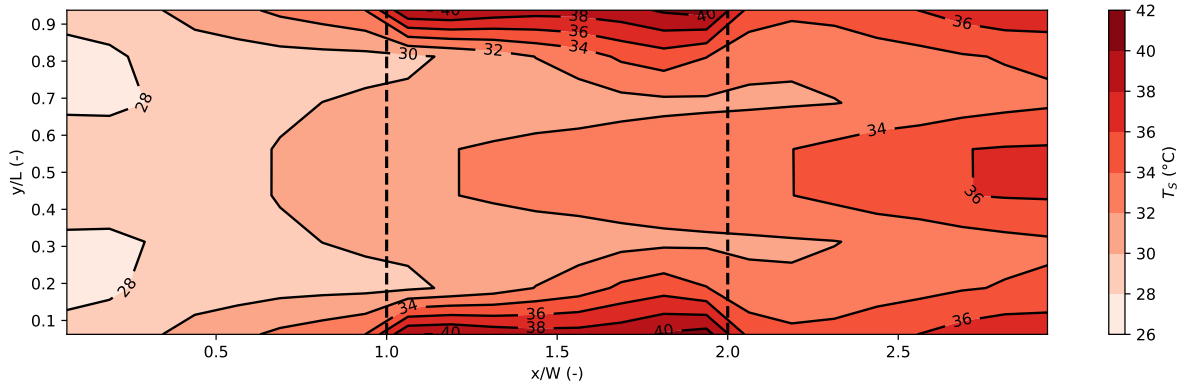

(b) $U_{in} = 2\ m/s$.

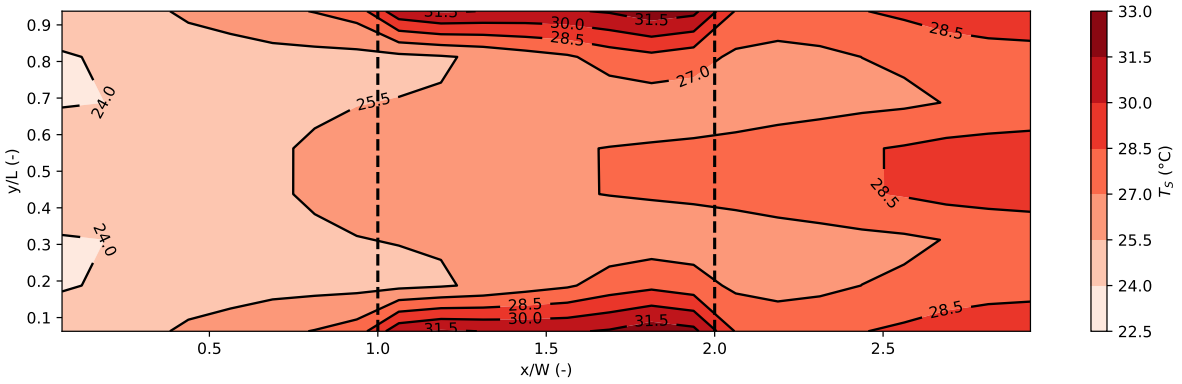

(c) $U_{in} = 4\ m/s$.

Figure 5.31: Surface temperatures with different inlet velocities for case 03 of the street area highlighted in figure 5.20. The vertical dashed lines separate the intersection area from the rest of the street area. *Note: The color bar ranges differ per plot.*

5.5. Case 5: Effect of wall heating on flow characteristics

This case studies the effect of wall heating on flow characteristics in a 2D street canyon and is based on the study of Cai (2012). In his study, Cai uses LES to model flow characteristics with different types of wall heating and compares this with wind-tunnel experiments of Kovar-Panskus et al. (2002). Cai distinguishes two heating scenarios: (1) the roof and the entire downstream wall are heated, called 'the opposing case', and (2) the roof and the entire upstream wall are heated, called 'the assisting case'. Besides that, this simulation was also done by Suter (2019) to validate his sensible heat flux model. Although Cai and Suter use LES with periodic boundary conditions, it is attempted to reproduce their results with the current model. The goal of this case study is to showcase the CFD model's capabilities to simulate flow under the influence of buoyancy. On top of that, the effect of non-homogeneous heated walls is also studied, where wall boundary conditions are provided by the SEB model.

5.5.1. Simulation set-ups

The simulation set-up is similar to the infinite street canyon case (section 5.2) and is given in figure 5.32. The simulation is completely done with the CFD model, i.e., the SEB model was not used. The SEB model is merely used to provide the non-homogeneous boundary conditions in the second part of this case. Only the walls of building 12 and building 13 are heated. This ensures that the flow is developed before it reaches the heated walls. The assisting- and opposing cases are schematically given in figure 5.33. In the assisting case, the wall of building 12 and both roofs of building 12 and 13 are heated. In the opposing case, the wall of building 13 and both roofs of building 12 and 13 are heated. All heated wall temperatures are kept constant at 29 $°C$, which matches Cai (2012) and Suter (2019). The rest of the walls are adiabatic. The inlet air has temperature, T_{in}, of 20 $°C$ and has a constant and homogeneous velocity, U_{in}, of 2.5 m/s. The building height H, building width W, and street width are all equal to 18 m. The canyon length L is set to 60 m to speed up the simulations. In this case, the focus lies on the street canyon between building 12 and 13. Therefore, the velocity vector fields and temperature fields between these two buildings will be discussed. All relevant simulation parameters are given in table 5.12. With this set-up, a 2D approximation is made by focusing on the plane $y = L/2$ and therefore the results can be compared to Cai and Suter.

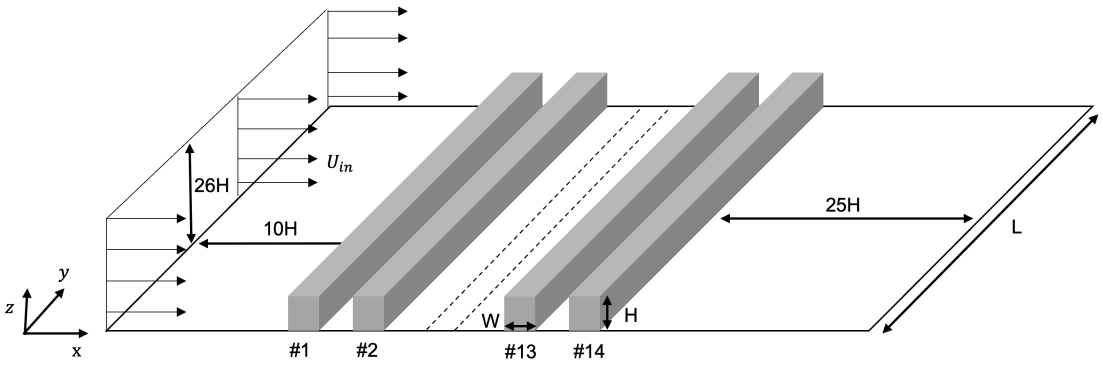

Figure 5.32: A schematic representation of the simulation set-up. For imaging purposes, the two dashed lines indicate the part where obstacles 3-12 are left out.

	Simulation parameters
Inlet air temperature, T_{in}	20 $°C$
Heated wall temperature, T_0	29 $°C$
Inlet velocity, U_{in}	2.5 ms^{-1}
Cell expansion factor	1.1
Minimal cell size	$(x \times y \times z) = (0.3m \times 1m \times 0.3m)$
Maximum cell size	$(x \times y \times z) = (25m \times 25m \times 25m)$

Table 5.12: All parameter values used in this case study if not stated otherwise.

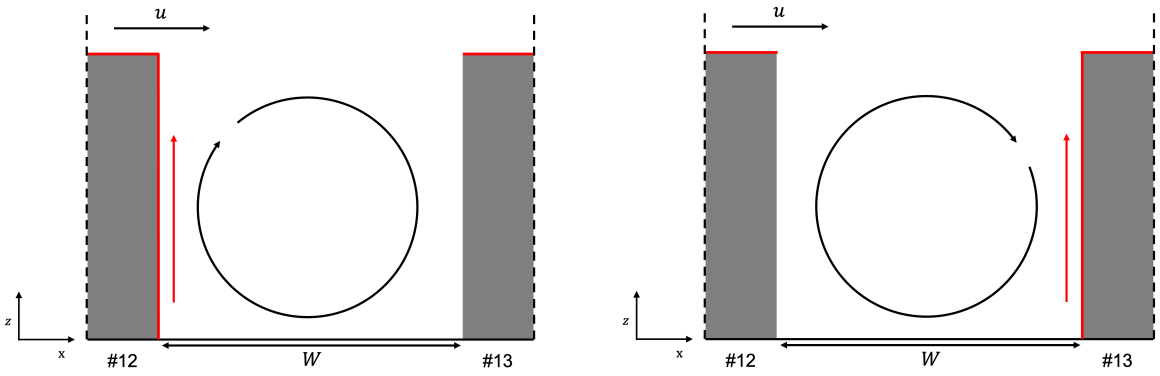

(a) Assisting case. **(b)** Opposing case.

Figure 5.33: A schematic overview of the assisting case (a) and the opposing case (b). The red lines indicate the walls that are heated, the rest of the walls are left adiabatic. For imaging purposes, the figure only shows the street canyon between building 12 and building 13.

Besides the simulation set-up stated above, another simulation is done that couples the SEB model and the CFD model. This simulation set-up is similar to the one stated above but only differs in the temperature distribution of the walls. The heated walls, depicted as red lines in figure 5.33, are divided into five line segments each. These line segments are given a temperature that is taken from the output of the SEB model. This simulation is done to showcase the capabilities and prospects of coupling between the SEB model and the CFD model. The parameters used in this case study for the SEB model are given in table 5.13. In the opposing case, the solar azimuthal angle is at 270 °, and in the assisting case it is at 90 °.

	Radiation
Diffusive sky radiation, D_{sky}	84.2 Wm^{-2}
Longwave absorptivity, ζ	0.95
Longwave emissivity, ε	0.95
Longwave sky radiation, L_{sky}	325 Wm^{-2}
Shortwave albedo factor, α	0.40
Solar irradiance, I	950 Wm^{-2}
Solar zenith angle, θ_s	50 °
	Heat conduction
Interior temperature, T_∞	20 °C
Thermal conductivity, λ	0.72 $Wm^{-1}K^{-1}$
Thickness building, d	0.25 m
Thickness street, d	1 m

Table 5.13: All parameter values used in this case study for the SEB model.

5.5.2. Results

The results for the velocity vector fields for both the assisting- and opposing cases are given in figure 5.34. The results for the temperature fields for the two cases are shown in figure 5.35. All results are compared to vector fields found by the LES of Cai (2012). The results of Suter (2019) are left out in this section. Note that the origin of the axes of Cai and the color bar used by Cai differ from those used in this study.

The vector fields show good agreement with the vector fields of Cai (2012). It can be seen that in this study's results and Cai's results the magnitude of the vectors is greater in the assisting case than in the opposing case. Besides that, a small vortex is seen in the bottom right of the canyon in the opposing case which matches the literature results. Also, it can be noted that the center vortex in the assisting case is at location $(x/W, z/H) = (0.5, 0.5)$, which matches with Cai. The location of this vortex has shifted in the opposing case to approximately $(x/W, z/H) = (0.57, 0.57)$. Although this location does not exactly

match Cai's results, it does shift in the same direction.

The temperature fields do not show good agreement with the temperature fields found by Cai (2012). It can be observed that, for both the assisting- and opposing cases, the temperature values are lower than the literature values. Besides that, the shape of the temperature fields is dissimilar. What the results of the current study do have in common with literature values is the overheating of the opposing case compared to the assisting case. It can be observed that the average air temperature inside the canyon is higher in the opposing case than in the assisting case. This is in line with what is found by Cai.

The large differences between the temperature fields of the current study and Cai's study is likely due to a difference in boundary conditions. Cai (2012) and Suter (2019) use periodic boundary conditions in their simulations, which are not used in this study. The use of periodic boundary conditions facilitates constant heating of the street canyon; the hot air leaving the simulation domain is, again, fed into the system. In the simulations of Cai (2012), the simulation is run for 20 turnover times. This results in higher air temperatures inside and above the street canyon, which is also seen in the results of Cai (figure 5.35).

A slight difference in the *wall Richardson number* could also have led to the mismatch in the results. The wall Richardson number is used by Cai to provide the ratio between thermally generated kinetic energy and wind-generated kinetic energy. It is defined as

$$Ri_w = \frac{gH(T_r - T_0)}{T_r U_r^2},$$

where T_r is the mean air temperature above roof level, H is the wall height, g is the acceleration of gravity, T_0 the heated wall temperature and U_r the mean wind speed at 2.5H above roof level. In this case, $T_r = T_{in}$. In Cai's simulations, $Ri_w = -1.27$ is adopted. According to the formula above, this study uses $Ri_w = -0.69$. Although the difference between these two is small, it could have led to dissimilarities in results.

This study's grid makes use of the cell expansion factor, which increases cell sizes when further away from the walls. The grid is thus inhomogeneous, which can also be seen from the difference in density of the velocity vectors in figure 5.34a and 5.34b. The grid inhomogeneity could lead to an inaccuracy in the location of the center vortex. In further research, it is therefore recommended to homogenize and refine the grid in between the buildings.

To speed up the simulations, the length of the canyon, L, was set to 60 m. This means that the length-over-height ratio (L/H) of the canyon was 3.33. This is on the low side, considering Santamouris et al. (1999), Giovannini et al. (2013) and Coronel and Álvarez (2001) found significant 3D effects on the airflow in canyons with L/H ratios between 1.25-5.5. However, since the current simulation is set in a complete 2D fashion (inlet velocity is only in x-direction), it could be argued that at $y = L/2$ the 3D effects are minimal. In further research, it is recommended to increase the canyon length to ensure the 2D approximation is accurate.

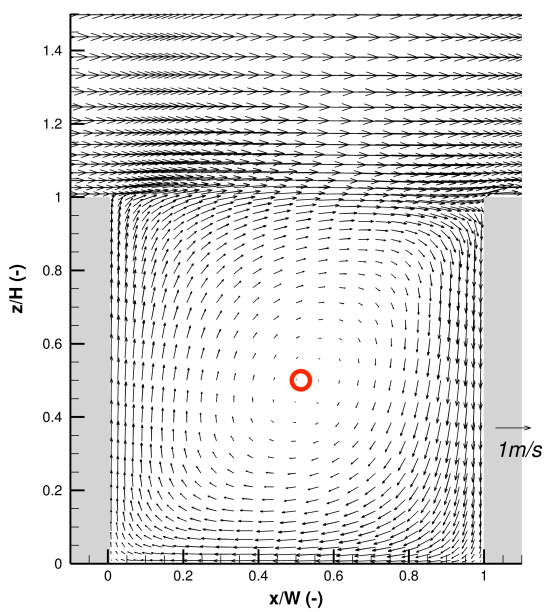

(a) Assisting case current study.

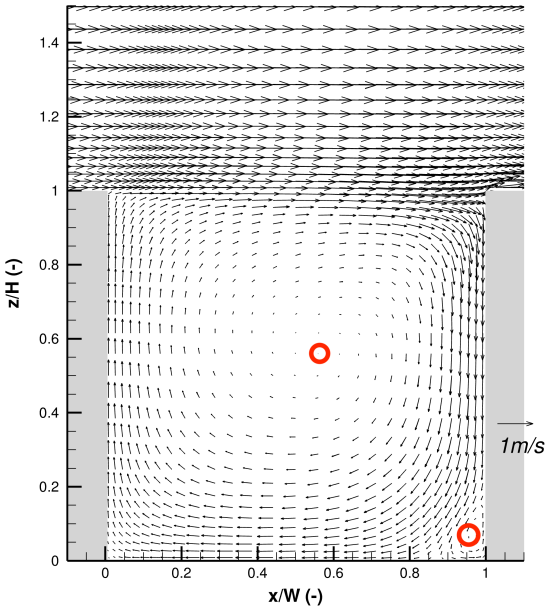

(b) Opposing case current study.

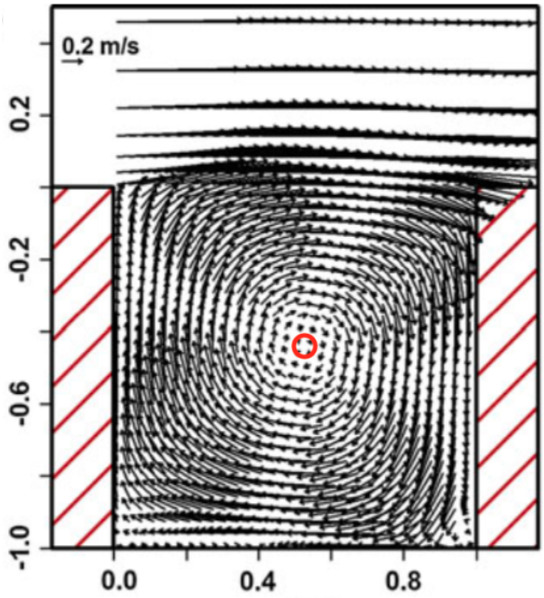

(c) Assisting case Cai (2012).

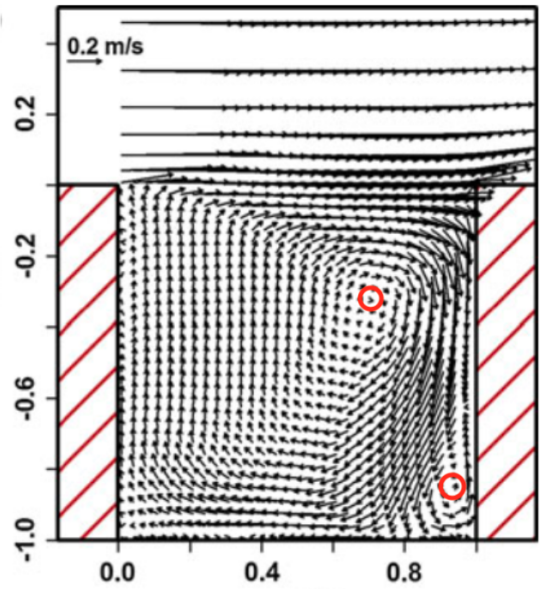

(d) Opposing case Cai (2012).

Figure 5.34: An overview of the current study's results for the vector fields (top row) and the results of Cai (2012) (bottom row). The left column represents results of the assisting case and the right column represents results from the opposing case. The red circles indicate the location of the vortices.

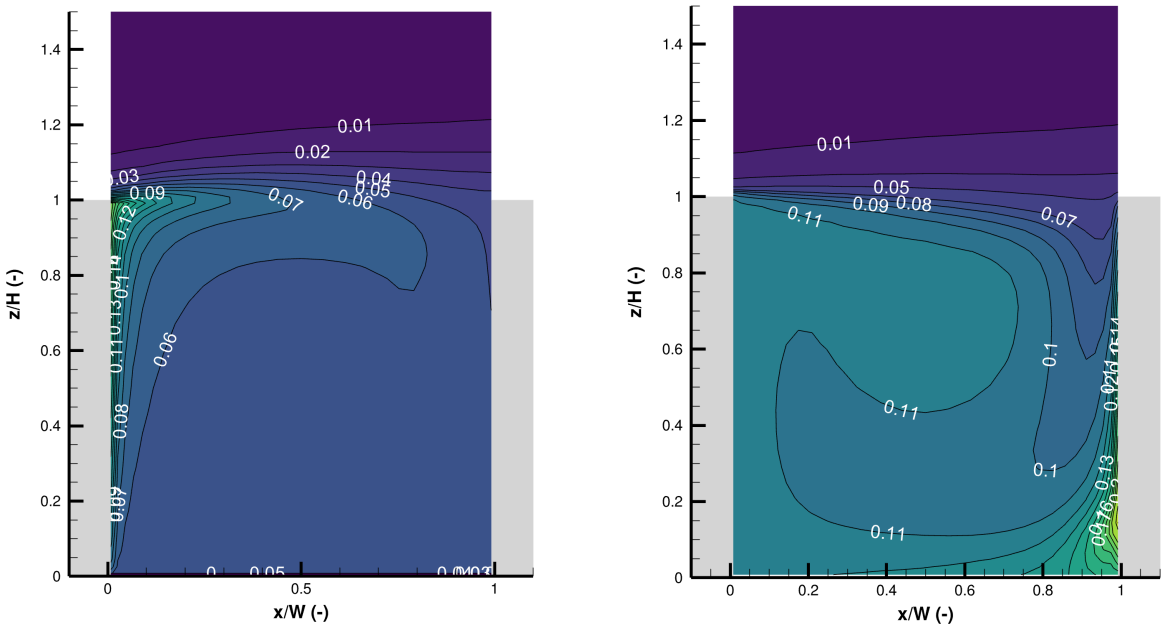

(a) Assisting case current study.

(b) Opposing case current study.

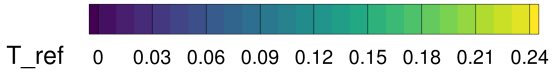

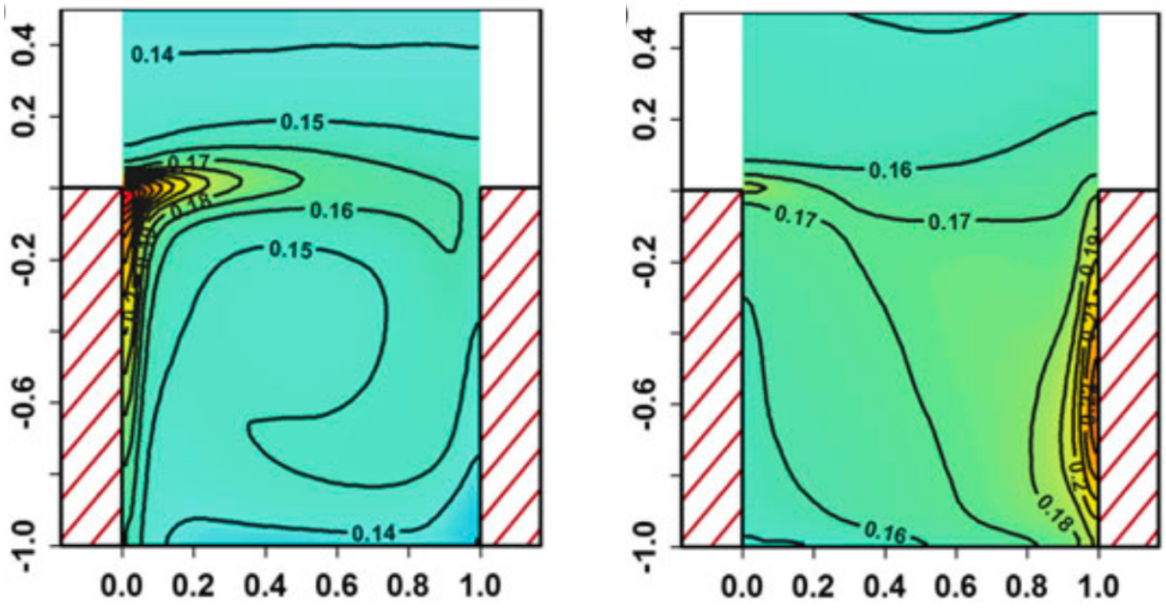

(c) Assisting case Cai.

(d) Opposing case Cai.

Figure 5.35: The normalized temperature fields for the current study (top row) and Cai (2012) (bottom row). Here, the normalized temperature is $T_{ref} = (T - T_0)/\Delta T$, where ΔT is the temperature difference between the heated wall and air above roof level. *Note: A different range and type of color bar is used in Cai's results.*

Coupling between SEB- and CFD model

In the previous section, the walls and roofs were kept at a constant and homogeneous temperature. In this section, the walls and roofs will be kept at a constant but inhomogeneous temperature taken from the output of the SEB model simulation. The assigned wall temperatures are shown in figure 5.36 for both cases. Note that for the assisting case, only the west wall temperatures and roof temperatures are used, the rest of the surfaces are kept adiabatic in the CFD simulations. For the opposing case only the east wall temperatures and roof temperatures are used, the rest is again kept adiabatic. The results are shown in figure 5.37.

What stands out from figure 5.37 is that the results of the velocity field of the assisting case for the inhomogeneous heated walls are similar to the results of the homogeneous heated walls (see previous section). The temperatures are, however, a significant amount higher, which is due to higher wall temperatures of above 45 °C. The opposing case results for the inhomogeneous heated walls also show higher temperatures compared to the homogeneous heated walls case. The velocity field shows multiple vortices and shows a different pattern compared to the homogeneous case.

Both velocity vector fields show unphysical behavior near the walls. This is especially evident in the opposing case, at the bottom right corner of the street canyon. The most likely reason for this is the large differences in temperatures of the line segments. Each heated wall is divided into five line segments, where to each line segment a temperature is provided from the SEB model. For the current solar position and simulation parameters, the lower part of the heated wall is shaded. This results in a temperature difference of approximately 20 °C between the first line segment, which is shaded, and the second line segment, which is sun-lit (see figure 5.36). The unphysical behavior shows that there is a lot of room for improvement. Improvements can be made by refining the grid of the SEB model and of the CFD model. Due to time constraints, this was not realizable in this study.

The temperature fields of the assisting- and opposing cases are quite different. The temperature field for the assisting case shows that there is a significant amount of mixing in the street canyon, which is also backed up by its velocity vector field. The temperature field of the opposing case shows a degree of stratification, apart from the temperatures at the heated wall. The buoyancy forces, in this case, are significantly more dominant compared to the homogeneous heated walls case. This could have led to a partly stratified temperature field for the opposing case.

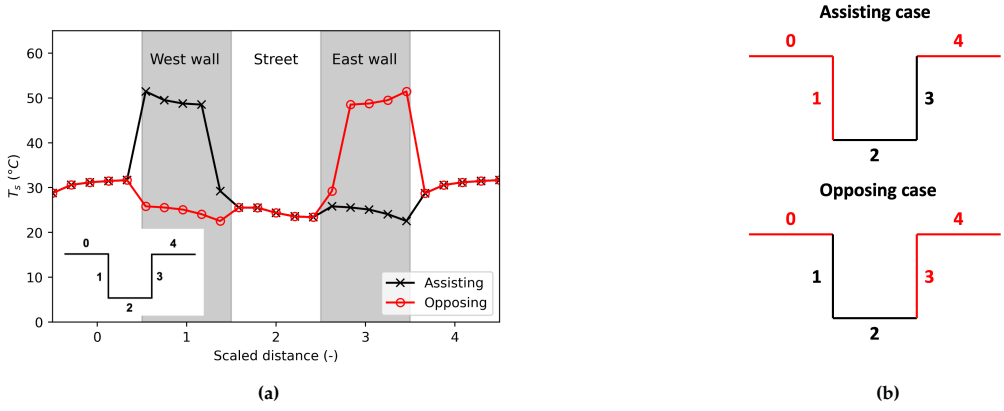

Figure 5.36: The temperature profiles used as input to the CFD simulations plotted in figure (a). Note that only the parts of the profile are used that coincide with the red highlighted parts in figure (b). The plotting is done according to the inset shown in the bottom left.

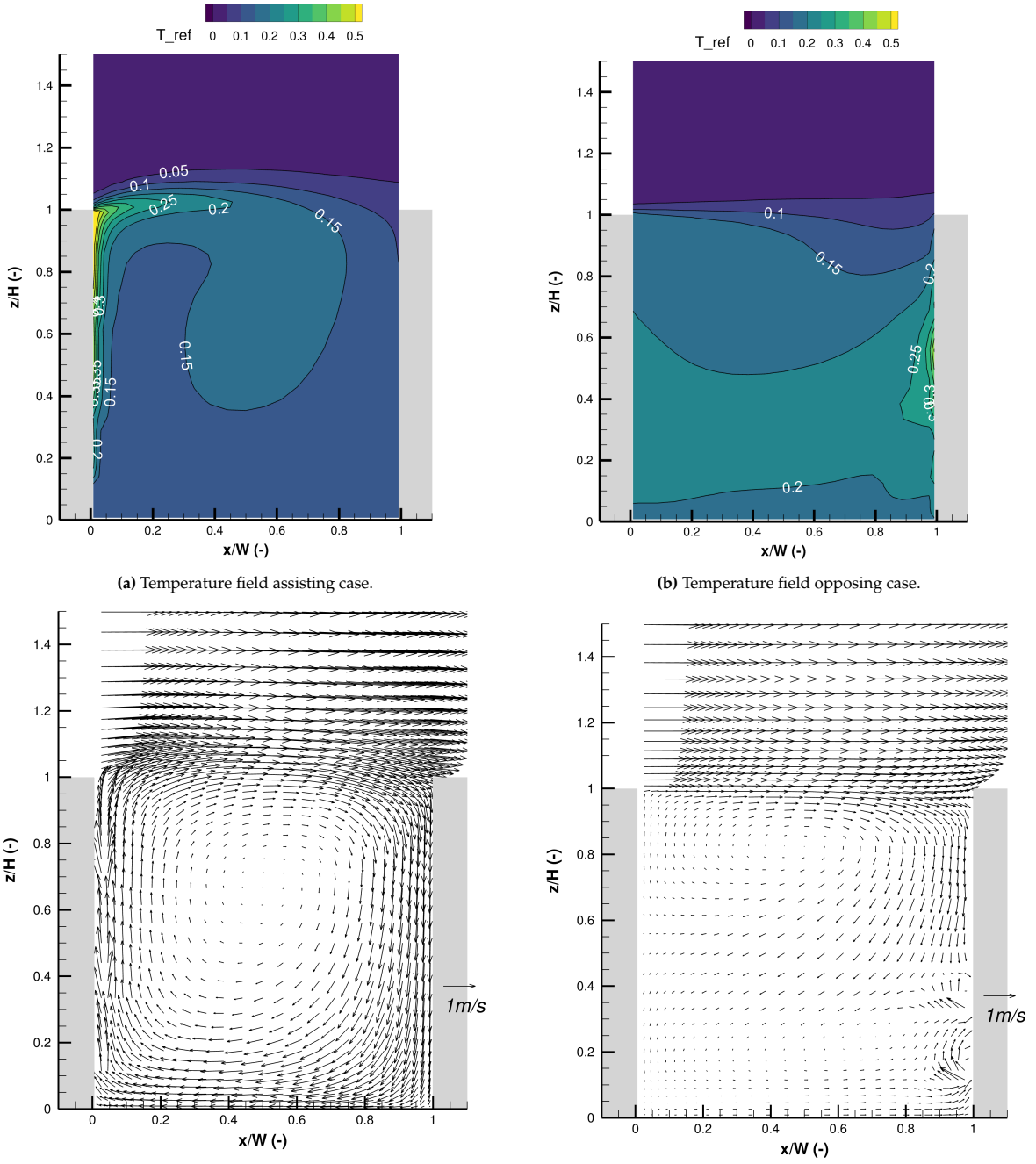

(a) Temperature field assisting case.

(b) Temperature field opposing case.

(c) Velocity field assisting case.

(d) Velocity field opposing case.

Figure 5.37: The normalized temperature fields (top row) and their velocity vector fields (bottom row) for the case of coupling between SEB- and CFD model. Here, the normalized temperature is $T_{ref} = (T - T_0)/\Delta T$, where ΔT is 9 °C and T_0 is 20 °C. The left column designates the assisting case results and the right column designates the opposing case results.

Stability of the solution

In this section, the stability of the solution of the non-homogeneous heated walls case will be discussed. The motivation behind this is the unphysical behaviour that was seen in the previous results. The stability check is done by running the simulation results of figure 5.37 for 15,000- and 30,000 iterations longer. The results are shown in figure 5.38 for the assisting case and in figure 5.39 for the opposing case.

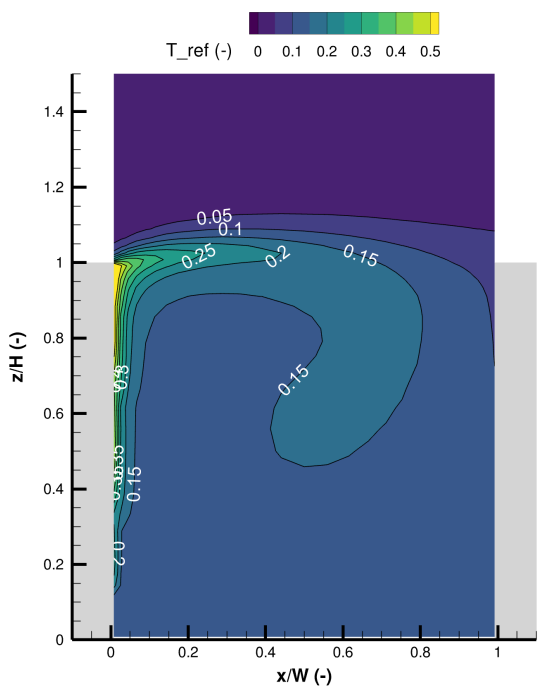

(a) 15k iterations more.

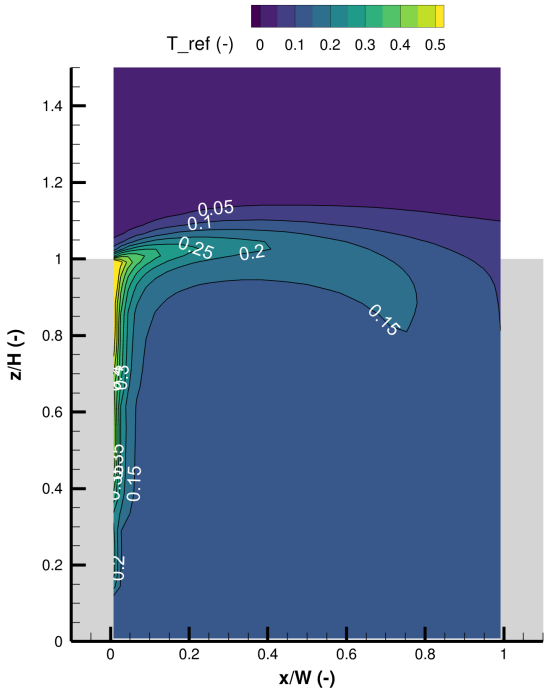

(b) 30k iterations more.

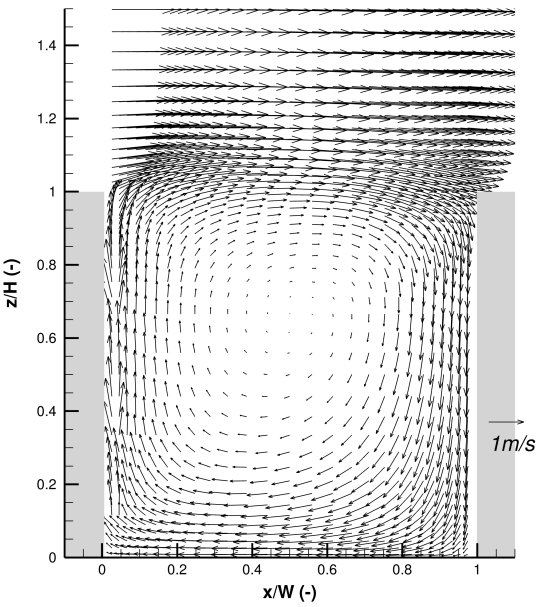

(c) 15k iterations more.

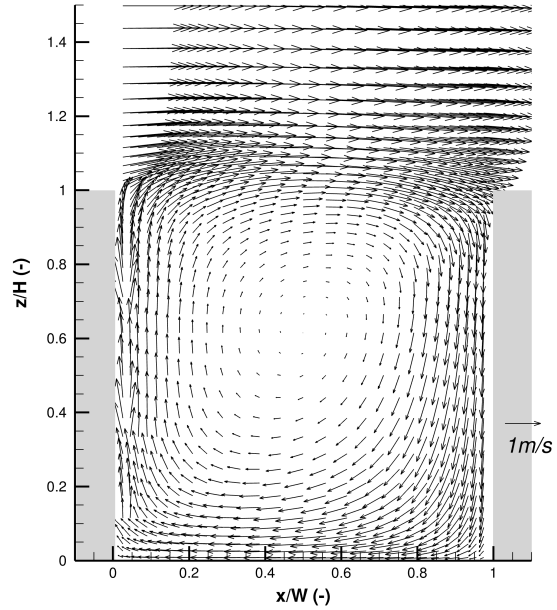

(d) 30k iterations more.

Figure 5.38: The normalized temperature fields (top row) and velocity vector field (bottom row) for the assisting case and longer iterations. Here, the normalized temperature is $T_{ref} = (T - T_0)/\Delta T$, where ΔT is 9 °C and T_0 is 20 °C. The figures represent 15,000 - and 30,000 iterations more compared to figure 5.37.

The longer simulated assisting case results are similar to the results in figure 5.37. The velocity field has a similar pattern with only one central vortex in the center of the canyon. The temperature field, however, is slight different from the original result but its shape stays coherent. This shows that the assisting case is quite stable.
The longer simulated opposing case results (figure 5.39) show quite the dissimilarity with the original results (figure 5.37). The temperature fields are very dissimilar in shape but the values are similar. Besides that, the velocity field shows a different pattern for the original case, the 15,000 iterations more

case and the case of 30,000 iterations more. This lack of cohesion shows that the system is quite unstable and may be inherently time-dependent. There does not seem to be a single solution to this system and the solutions might be more dynamic. It is therefore recommended to simulate the problem in time-dependent mode.

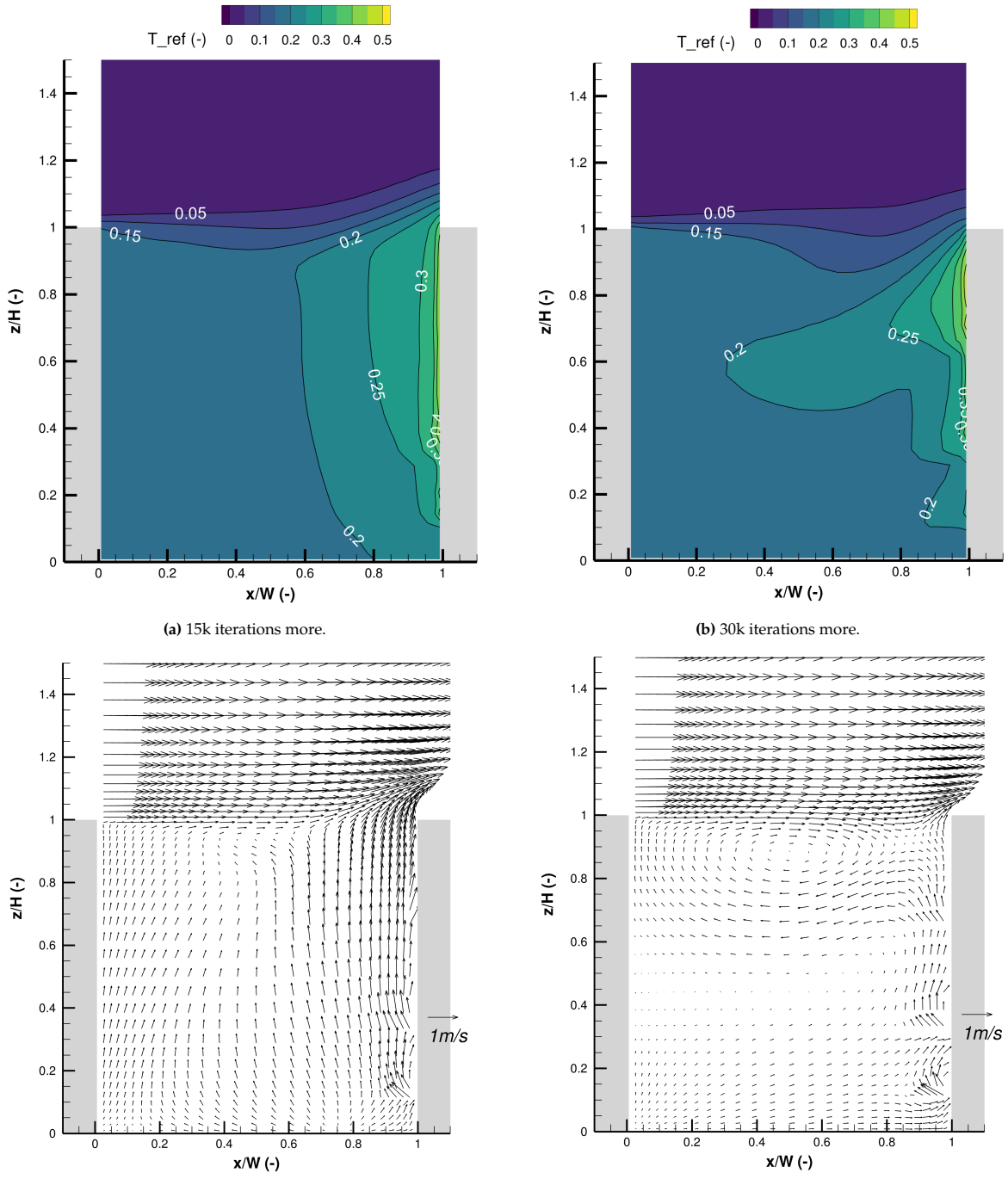

(a) 15k iterations more.

(b) 30k iterations more.

(c) 15k iterations more.

(d) 30k iterations more.

Figure 5.39: The normalized temperature fields (top row) and velocity vector field (bottom row) for the opposing case and longer iterations. Here, the normalized temperature is $T_{ref} = (T - T_0)/\Delta T$, where ΔT is 9 °C and T_0 is 20 °C. The figures represent 15,000 - and 30,000 iterations more compared to figure 5.37.

6

Conclusions and Recommendations

6.1. Summary and conclusions

The goal of this study was to model the surface energy balance at micro-scale in order to acquire fundamental insights into the UHI-effect. A model has been built mechanism-by-mechanism, adding in different physical mechanisms one at a time. After each step, the model is validated, both qualitatively and quantitatively, with the help of various case studies found in literature. After validation, a more complex scenario of a 3D street canyon is studied, where the effect of different heat fluxes on the surface temperature is investigated. On top of that, the effect of wall heating on flow characteristics is also studied. In this chapter, this study's model will be referred to as *the SEB model*. The most significant findings of this study are:

- The SEB model gives good qualitative and quantitative agreements with an experimental study concerning the diurnal variation of the effective albedo of three urban structures. The model correctly captures the multiple reflective behavior of shortwave radiation between buildings.

- The SEB model produces highly realistic shadow patterns around buildings with the use of the sun-lit factor computation.

- The view factor algorithm used in this work is validated and showed very good agreement with analytical values. The employed Gauss-Legendre quadrature achieves less than 0.1 % relative error compared to the analytical values.

- The SEB model showed a good agreement for its longwave radiation and conduction modeling when compared to theoretical values.

- A good agreement was found for the radiative surface fluxes between this work and a numerical study from literature. The conductive heat flux and sensible heat flux showed a lesser agreement with this numerical study.

- Although the SEB model is inherently steady-state, it can produce realistic diurnal patterns by simulating different moments during the day.

- The longwave trapping effect between buildings is captured with high fidelity by the SEB model. It was found that this effect is significantly enhanced by a larger building height-over-width ratio. The SEB model can show on micro-scale in which parts this effect is the most severe within an urban canyon.

- An agreement was found between the 3D street canyon temperature profiles and the 2D street canyon temperature profiles. It can therefore be said that a 2D approximation is a realistic

approximation for a street canyon.

- A good agreement was found for the effect of wall heating on flow characteristics between this study and a numerical study from literature. The non-homogeneously heated walls case showed incoherent behaviour for the opposing case which may be the result of the system being dynamic and inherently time-dependent.

6.2. Recommendations

Based on the findings of this study, several recommendations can be made for future research. These recommendations are listed below.

- *Include other surface energy fluxes*: In this work, only four surface energy fluxes are included and modeled in the SEB model. The fluxes that are left out are, among others, the latent heat flux and the anthropogenic heat flux. Including these two surface energy fluxes in the SEB model would make the model more complete and realistic.

- *Universal Thermal Climate Index*: In future studies, it would be interesting to add an algorithm for calculating the Universal Thermal Climate Index (UTCI). The UTCI is an index that quantifies the thermal comfort of the human body under specific meteorological conditions. Studying the UTCI with the current model would give more insight into the effect of specific heat fluxes on human thermal comfort.

- *Different urban geometries*: Urban environments are usually quite heterogeneous, with buildings of different sizes and shapes. It is therefore recommended to study different and more complex geometries. Possible geometries are buildings with different heights, buildings with windows and circular-shaped buildings.

- *Improved model inputs*: The SEB model's inputs can be further enhanced by coupling the model with an atmospheric weather model. The weather model can provide more detailed model inputs, such as the solar irradiance and the diffusive sky radiation.

- *Improve conduction modeling*: This study has modeled conduction through linearization and by using a constant interior temperature boundary condition. The model can be improved by applying a zero-flux boundary condition and by dividing the interior into multiple layers, each with different thermal properties.

- *Validation with experimental studies*: The sensible heat flux model and conductive heat flux model of the SEB model have not been validated with experimental studies. The validation with experimental studies from literature is therefore recommended to make the model more robust and complete.

- *Two-way coupling:* In this study, the SEB- and CFD model have been coupled through a one-way coupling approach. To make the model more complete and realistic, it is recommended to improve the model by applying two-way coupling between the SEB- and CFD models.

- *Time-dependent mode:* In this study, the non-homogeneously heated walls case was simulated by using a steady-state RANS approach. The results suggested that the system may be inherently time-dependent. It is therefore recommended to do this case study with a time-dependent approach. This can be done by using, for example, LES or T-RANS.

References

Abramowitz, M. and I.A. Stegun (1964). Handbook of Mathematical Functions. *Dover Publications, New York*, p. 887.

Aida, M. (1982). Urban Albedo as a Function of the Urban Structure - A Model Experiment. *Boundary-Layer Meteorology* 23, pp. 405–413.

Ambirajan, A. and S.P. Venkateshan (1993). Accurate determination of diffuse view factors between planar surfaces. *Int. J. Heat Mass Transfer* 36.8, pp. 2203–2208.

Arnfield, A.J. (1988). Validation of an estimation model for urban surface albedo. *Physical Geography* 9.4, pp. 361–372.

Cai, X. (2012). Effects of Wall Heating on Flow Characteristics in a Street Canyon. *Boundary-Layer Meteorology* 142, pp. 443–467.

Chao, C.L. (2010). Numerical Analysis of Turbulent Dispersion of Pollutants in Simplified Urban Areas at Laboratory Scale. *MSc thesis. Delft University of Technology*.

Coronel, J.F. and S. Álvarez (2001). Experimental work and analysis of confined urban spaces. *Solar Energy* 70.3, pp. 263–273.

de Bruin, G. (2022). A numerical study on the influence of vehicle induced turbulence on the dispersion of pollutants in urban areas using the RANS k-ϵ model. *MSc thesis. Delft University of Technology*.

Ehrhard, J. et al. (2000). The microscale model MIMO: development and assessment. *Journal of Wind Engineering and Industrial Aerodynamics* 85.2, pp. 163–176.

Fortuniak, K. (2008). Numerical estimation of the effective albedo of an urban canyon. *Theoretical and Applied Climatology* 91, pp. 245–258.

Garratt, J.R. (1992). The atmospheric boundary layer. *Cambridge University Press*.

Giovannini, Lorenzo, Dino Zardi, and Massimiliano de Franceschi (2013). Characterization of the Thermal Structure inside an Urban Canyon: Field Measurements and Validation of a Simple Model. *Journal of Applied Meteorology and Climatology* 52.1, pp. 64–81.

GNU Fortran (GCC) 8.5.0 20210514 (2021). Originally John Backus and IBM. *Boston, United States*.

GOSmartBricks (2022). *Urban Heat Island – 7 Things You Should Know*. URL: `www.gosmartbricks.com/urban-heat-island/` (visited on 12/15/2022).

Grosan, C. and A. Abraham (May 2008). A new approach for solving nonlinear equations systems. *IEEE Transactions on Systems, Man, and Cybernetics-Part A: Systems and Humans* 38.3, pp. 698–714.

Grylls, T. et al. (2021). uDALES: large-eddy-simulation software for urban flow, dispersion, and microclimate modelling. *Journal of Open Source Software* 6.63, p. 3055.

Guan, K.K. (2011). *Surface and ambient air temperatures associated with different ground material: A case study at the University of California, Berkeley*, pp. 1–14.

Hanjalić, K. et al. (2007). Analysis and modelling of physical transport phenomena. *VSSD*.

Heating Refrigerating, American Society of and Air-Conditioning Engineers Inc. (ASHRAE) (2001). ASHRAE Fundamentals Handbook. *Ch. 30*.

Ibrahim, Siti Halipah et al. (2018). The impact of road pavement on urban heat island (UHI) phenomenon. *International Journal of Technology* 9 (8), pp. 1597–1608.

Kanda, M., T. Kawai, and K. Nakagawa (2005). A Simple Theoretical Radiation Scheme for Regular Building Arrays. *Boundary-Layer Meteorology* 114, pp. 71–90.

Kolokotroni, M., I. Giannitsaris, and R. Watkins (2006). The effect of the London urban heat island on building summer cooling demand and night ventilation strategies. *Solar Energy - SOLAR ENERG* 80, pp. 383–392.

Kovar-Panskus, A. et al. (2002). A Wind Tunnel Investigation of the Influence of Solar-Induced Wall-Heating on the Flow Regime within a Simulated Urban Street Canyon. *Water, Air, & Soil Pollution: Focus* 2, pp. 555–571.

Launder, B.E. and B.I. Sharma (1974). Application of the energy-dissipation model of turbulence to the calculation of flow near a spinning disc. *Letters in heat and mass transfer* 1.2, pp. 131–137.

NOAA (2023). *Solar Calculator*. URL: `www.gml.noaa.gov/grad/solcalc/` (visited on 03/06/2023).

Núñez, M. and T.R. Oke (1977). The Energy Balance of an Urban Canyon. *Journal of Applied Meteorology* 16, pp. 11–19.

Oke, T.R. (1982). The Energetic Basis of the Urban Heat Island. *Quarterly Journal of the Royal Meteorological Society* 3, pp. 1–24.

Oke, T.R. et al. (2017). Urban Climates. *Cambridge University Press*.

Patankar, S.V. (1980). Numerical Heat Transfer and Fluid Flow. *Hemisphere Publishing Corporation*.

Pope, S.B. (2000). Turbulent flows. *Cambridge University Press*.

Pyrgou, A. and M. Santamouris (2018). Increasing Probability of Heat-Related Mortality in a Mediterranean City Due to Urban Warming. *International Journal of Environmental Research and Public Health* 15.8.

Python 3.9.12 (2023). Python Software Foundation. *Delaware, United States.*

Rao, V.R. and V.M.K. Sastri (1996). Efficient evaluation of diffusive view factors for radiation. *Int. Journal of Heat and Mass transfer* 39, pp. 1281–1286.

Royal Netherlands Meteorological Institute (2012). *Wheather Models*. URL: `https://www.knmi.nl/kennis-en-datacentrum/uitleg/weermodellen` (visited on 01/09/2023).

Santamouris, M. et al. (1999). Thermal and air flow characteristics in a deep pedestrian canyon under hot weather conditions. *Atmospheric Environment* 33.27, pp. 4503–4521.

Schlünzen, K.H. et al. (2003). Flow and Transport in the Obstacle Layer: First Results of the Micro-Scale Model MITRAS. *Journal of Atmospheric Chemistry* 44, pp. 113–130.

Schrijvers, P. (2020). Urban Climate at Street Scale: Analysis and Adaptation. *PhD thesis. Delft University of Technology*.

Sparrow, E.M. and R.D. Cess (1963). A new and simpler formulation for radiative angle factors. *ASME journal of heat transfer* 85, pp. 81–88.

Stone, H.L. (1968). Iterative Solution of Implicit Approximations of Multidimensional Partial Differential Equations. *SIAM Journal on Numerical Analysis* 5.3, pp. 530–558.

Suter, I. (2019). Simulating the impact of blue-green infrastructure on the microclimate of urban areas. *PhD thesis. Imperial College London*.

Tan, J. et al. (2010). The urban heat island and its impact on heat waves and human health in Shanghai. *International journal of biometeorology* 54.1, pp. 75–84.

Tecplot 360 (EX 2021 R2) (2022). Tecplot Inc. *Bellevue, Washington, United States*.

Vardoulakis, S., K. Dear, and P. Wilkinson (2016). Challenges and Opportunities for Urban Environmental Health and Sustainability: the HEALTHY-POLIS initiative. *Environmental Health* 15.

Wang, K. et al. (2007). Influences of urbanization on surface characteristics as derived from the Moderate-Resolution Imaging Spectroradiometer: A case study for the Beijing metropolitan area. *Journal of Geophysical Research: Atmospheres* 112 (D22).

World Health Organization (2022). *Urban health*. URL: `https://www.who.int/news-room/fact-sheets/detail/urban-health` (visited on 12/15/2022).

Wu, L. (1995). URBAN4: An Urban Canopy Layer Surface Energy Balance Climate Model. *PhD thesis. University of California, Los Angeles*.

A

View factors: Analytical solutions and calculated values

Analytical solutions

For certain configurations of two planes A_i and A_j, the analytical solution for the view factor ψ_{ij} exists. The three cases that are considered in this study are given in figure A.1. Case 1 represents two identical rectangles with size $z_1 \times y_1$ which are parallel to each other and separated by a distance x_1. Case 2 represents two rectangles of size $z_1 \times y_1$ and $x_1 \times y_1$ with one shared edge. The last case, case 3, consists of two rectangles with sizes $y_1 \times z_1$ and $x_1 \times y_2$ that have one shared vertex.

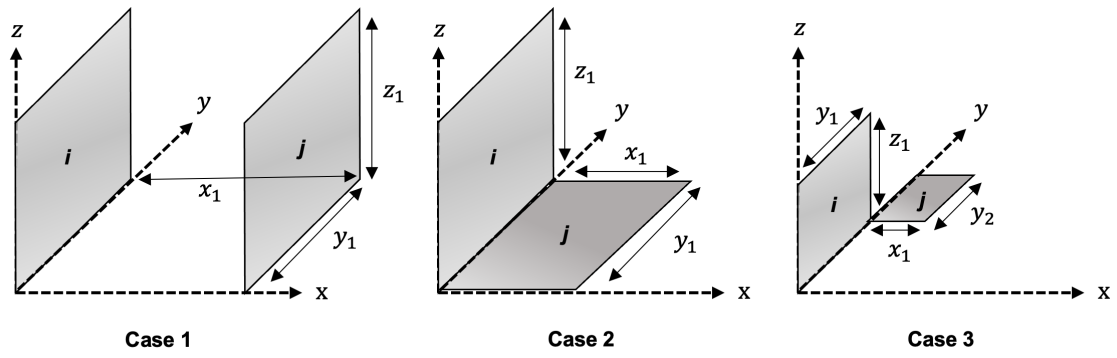

Figure A.1: A schematic overview of the three different test cases used to validate the view factor algorithm.

The analytical formulae for these three cases are stated below (Suter, 2019).

Case 1:

$$a = \frac{z_1}{x_1}, b = \frac{y_1}{x_1}$$

$$\begin{aligned}\psi_{ij} &= F_1(x_1, y_1, z_1) \\ &= \frac{2}{\pi a b}\left[\ln\sqrt{\frac{(1+a^2)(1+b^2)}{1+a^2+b^2}} + a\sqrt{1+b^2}\arctan\frac{a}{\sqrt{1+b^2}}\right. \\ &\left. + b\sqrt{1+a^2}\arctan\frac{b}{\sqrt{1+a^2}} - a\arctan a - b\arctan b\right].\end{aligned} \tag{A.1}$$

Case 2:

$$a = \frac{z_1}{y_1}, b = \frac{x_1}{y_1}$$

$$
\begin{aligned}
\psi_{ij} &= F_2(x_1, y_1, z_1) \\
&= \frac{1}{\pi a}\Bigg[a \arctan\frac{1}{a} + b \arctan\frac{1}{b} - \sqrt{a^2+b^2}\arctan\frac{1}{\sqrt{a^2+b^2}} \\
&+ \frac{1}{4}\log\Bigg[\frac{(1+a^2)(1+b^2}{(1+a^2+b^2)} \times \left(\frac{a^2(1+a^2+b^2)}{(1+a^2)(a^2+b^2)}\right)^{a^2} \\
&\times \left(\frac{b^2(1+a^2+b^2)}{(1+b^2)(a^2+b^2)}\right)^{b^2}\Bigg]\Bigg].
\end{aligned} \tag{A.2}
$$

Case 3:

$$
\begin{aligned}
\psi_{ij} &= F_3(x_1, y_1, y_2, z_1) \\
&= \frac{1}{2x_1y_1}\big[(y_1+y_2)x_1F_2(x_1, y_1+y_2, z_1) \\
&- x_1y_1F_2(x_1, y_1, z_1) - x_1y_1F_2(x_1, y_2, z_1)\big].
\end{aligned} \tag{A.3}
$$

View factor calculations

The calculated values for the three cases described in the previous section for the trapezoidal method and Gauss-Legendre method are given in the table below.

ψ_{ij}	Analyt.: ψ_p	GL: ψ_g	Trap.: ψ_t	$\psi_g/\psi_c - 1$	$\psi_t/\psi_c - 1$
Case 1 ($x_1 = y_1 = z_1$)	0.199825	0.199825	0.198980	0 %	- 0.4 %
Case 1 ($x_1 = y_1 = 0.5z_1$)	0.285875	0.285876	0.284004	0 %	- 0.7 %
Case 2 ($x_1 = y_1$)	0.200044	0.200044	0.200764	0 %	0.4 %
Case 2 ($x_1 = 0.5y_1$)	0.146187	0.146187	0.147445	0 %	0.9 %
Case 3 ($x_1 = y_1 = y_2 = z_1$)	0.0405922	0.0405572	0.0553735	- 0.1 %	27 %

Table A.1: A table comparing the Gauss-Legendre method (GL) and trapezoidal method (Trap.) for the calculation of the viewing factor for different cases, which are shown in the previous section. Both methods are computed with order 6. For each of these cases the analytical view factor is also given.

B

Quantitative results

Infinite street canyon case

The quantitative results for the infinite street canyon case are presented in this section. These results include the correlation coefficient, ρ_c, and the normalized mean absolute error (NMAE). Both the correlation coefficient and the NMAE compare this study's results with the results of Schrijvers (2020).

	$H/W = 0.5$	$H/W = 1$	$H/W = 2$
Surface fluxes			
K	0.984	0.999	0.998
L_{env}	0.997	0.998	0.997
L_{out}	0.978	0.982	0.919
L_{sky}	0.998	0.999	0.998
Surface temperatures			
Case 01	0.973	0.988	0.953
Case 02	0.878	0.872	0.758
Case 03	0.893	0.550	0.0910

Table B.1: Correlation coefficient comparison of the four different energy fluxes in case 01, and the surface temperatures per case. All values are given for the three H/W ratios.

	$H/W = 0.5$	$H/W = 1$	$H/W = 2$
Surface fluxes			
K	12.0 %	5.5 %	12.3 %
L_{env}	3.31 %	2.91 %	2.37 %
L_{out}	3.12 %	3.39 %	6.14 %
L_{sky}	3.89 %	2.60 %	13.7 %
Surface temperatures			
Case 01	4.12 %	2.55 %	6.06 %
Case 02	10.1 %	13.3 %	18.0 %
Case 03	12.4 %	26.7 %	15.2 %

Table B.2: NMAE comparison of the four different energy fluxes in case 01, and the surface temperatures per case. All values are given for the three H/W ratios.

C

Solar angles

The solar azimuthal angle, ϕ_s, and solar zenith angle, θ_s, used in this study as model input are given in this chapter.

Yokohoma National University

The solar angles used for simulating December 3rd, 1977, and June 15th, 1978, at Yokohama National University in Japan are given in the table below. Yokohoma National University is situated at the geographic location: (lat; lon) = (35.47; 139.58). The dates and location correspond to the experimental study of Aida (1982) and are used in validating the shortwave radiation model. All times shown in the tables are local time.

Time (h)	θ_s (°)	ϕ_s (°)
08:00	76	131
08:15	74	133
08:30	70	138
09:00	68	142
10:00	61	156
10:30	59	164
11:00	58	172
12:00	58	188
13:00	61	204
14:00	68	217
15:00	76	229
15:30	81	234
15:45	83	237
16:00	86	239

Table C.1: Solar angles on December 3rd, 1977.

Time (h)	θ_s (°)	ϕ_s (°)
07:00	61	81
07:30	55	84
08:00	49	89
09:00	37	98
10:00	25	112
11:00	15	140
12:00	13	199
13:00	21	240
14:00	32	257
15:00	44	268
16:00	57	276
16:30	63	280
17:00	69	284

Table C.2: Solar angles on June 15th, 1978.

Amsterdam

Time (h)	θ_s (°)	ϕ_s (°)
05:30	89	50
06:00	86	56
07:00	78	68
08:00	69	79
09:00	60	90
10:00	51	103
11:00	42	118
12:00	35	136
13:00	30	161
13:30	29	175
14:00	29	189
15:00	33	215
16:00	39	236
17:00	47	252
18:00	56	265
19:00	65	277
20:00	74	288
21:00	83	299
22:00	89	311

Table C.3: Solar angles on June 21st, 2023, in Amsterdam.

D

3D street canyon

D.1. Temperature profiles
Street temperature profiles

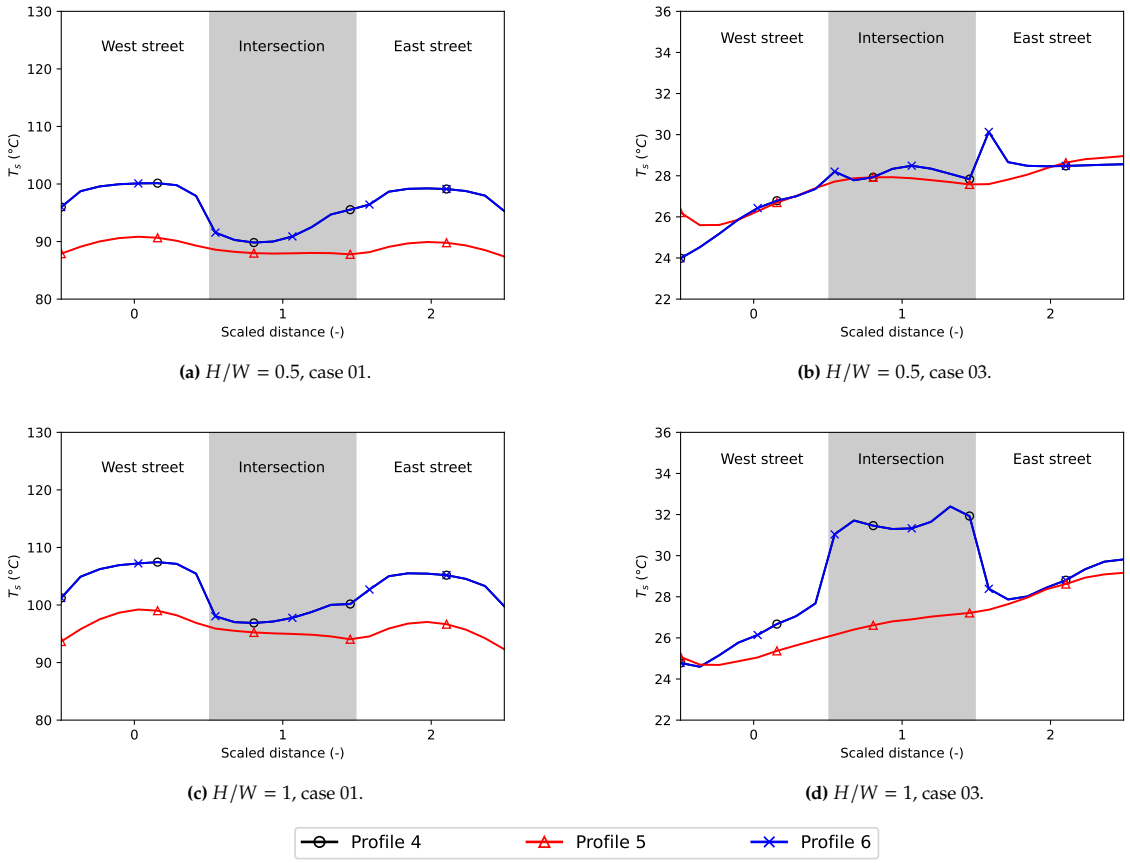

(a) $H/W = 0.5$, case 01.

(b) $H/W = 0.5$, case 03.

(c) $H/W = 1$, case 01.

(d) $H/W = 1$, case 03.

Figure D.1: Street temperature profiles plotting according to figure 5.24.

Street canyon temperature profiles

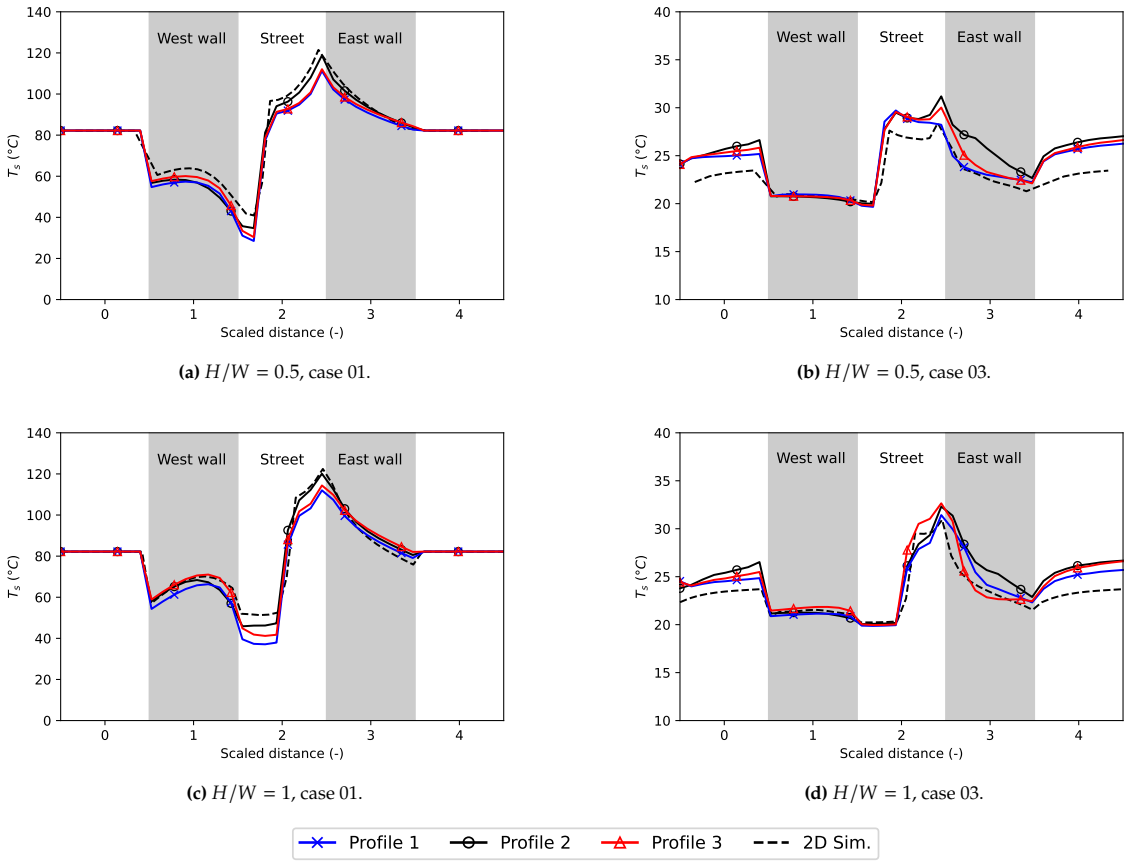

(a) $H/W = 0.5$, case 01.

(b) $H/W = 0.5$, case 03.

(c) $H/W = 1$, case 01.

(d) $H/W = 1$, case 03.

Figure D.2: Street canyon temperature profiles plotting according to figure 5.24.

D.2. Street temperature contours

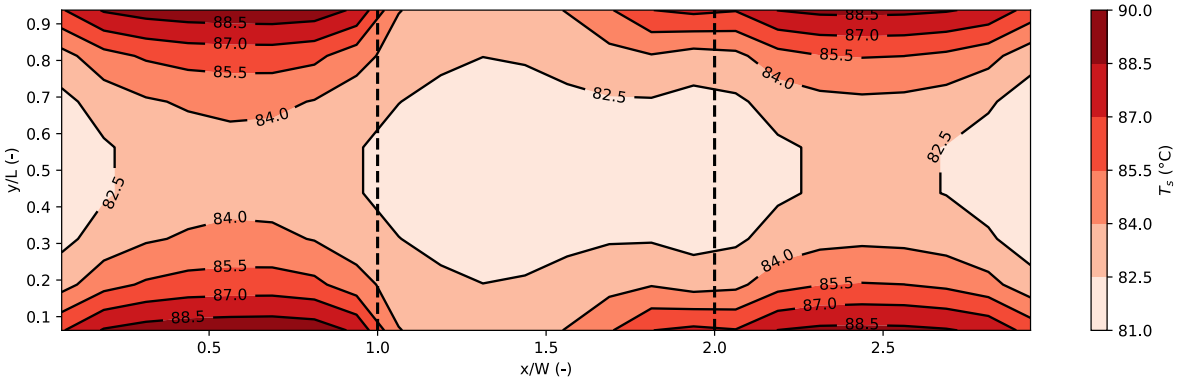

(a) $H/W = 0.5$.

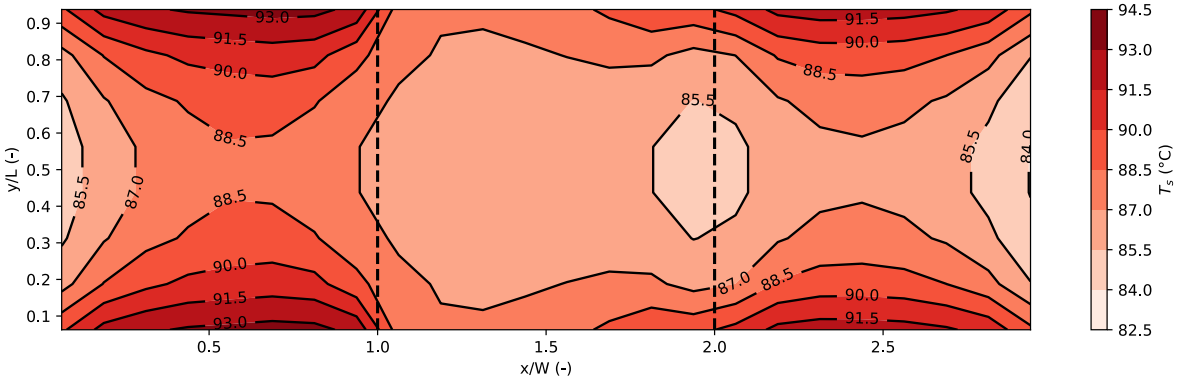

(b) $H/W = 1$.

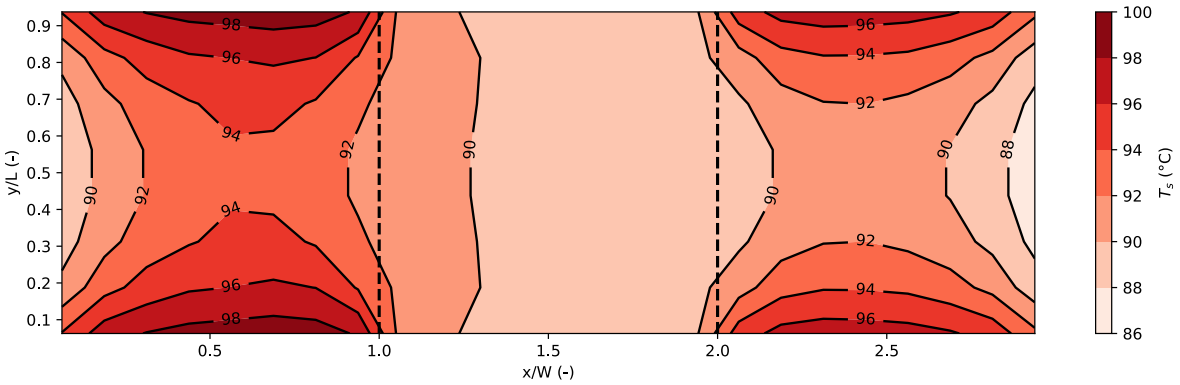

(c) $H/W = 2$.

Figure D.3: Contours of the street temperatures for case 02 at the intersection area highlighted in figure 5.20. The vertical dashed lines separate the intersection area from the rest of the street area. *Note: The colorbar ranges differ per plot.*

D.3. 3D plot surface temperatures

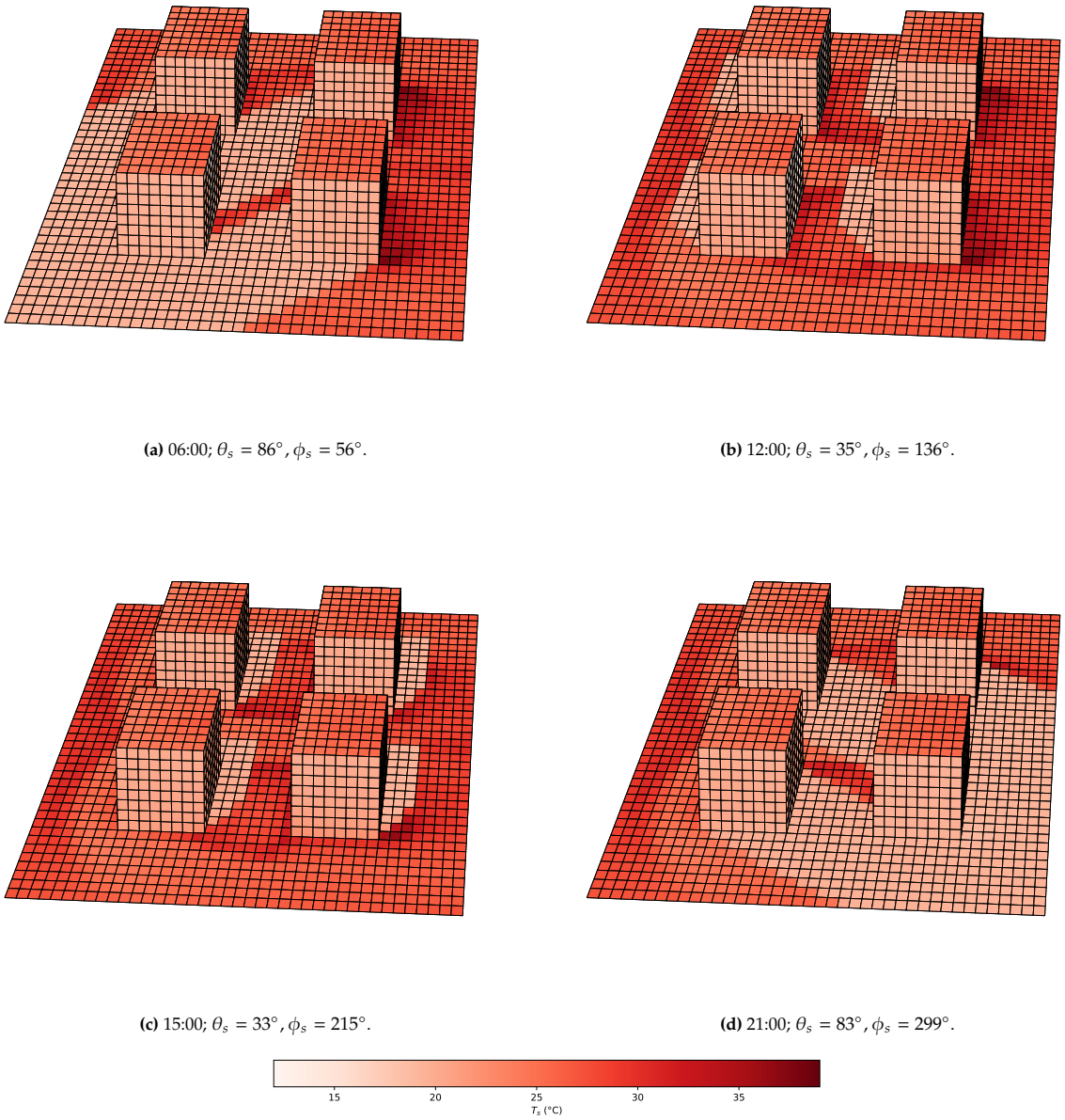

(a) 06:00; $\theta_s = 86°, \phi_s = 56°$.

(b) 12:00; $\theta_s = 35°, \phi_s = 136°$.

(c) 15:00; $\theta_s = 33°, \phi_s = 215°$.

(d) 21:00; $\theta_s = 83°, \phi_s = 299°$.

Figure D.4: A figure showing the surface temperatures in the 3D street canyon for case 03 for different times during the day. The different colors indicate different surface fluxes, shown in the legend. The different times include 06:00 (a), 12:00 (b), 14:00 (c) and 18:00 (d).